TECHNISCHE UNIVERSITÄT WIEN
Vienna University of Technology

DIPLOMARBEIT

Clinical Implementation of Volumetric Modulated Arc Therapy using MV Flat Panels as Quality Assurance System for Dosimetric Verification

ausgeführt am

Atominstitut
Technische Universität Wien
Stadionallee 2
1020 Vienna

in Zusammenarbeit mit

EBG MedAustron GmbH
Marie-Curie-Straße 5
2700 Wiener Neustadt

unter der Anleitung von

Univ.Prof. Dipl.-Ing. Dr.techn. Gerald Badurek

durch

Katja Presich
Novaragasse 32/18
1020 Wien

9471310
066 453

Abstract

Volumetric Modulated Arc Therapy (VMAT) is a relatively new radiation therapy technique. Compared to the so far used techniques like Intensity Modulated Radiation Therapy (IMRT) additional parameters of the medical linear accelerator are used to achieve a better treatment plan for the patient. VMAT allows better dose escalation in the tumor and reduces dose in critical tissue.

The goal of this work is the first step of clinical evaluation of this method to allow the usage of all new possibilities.
Primarily new used parameters have to be identified. These parameters include varying dose rate, movement of the multi leaf collimators during irradiation and gantry movement during irradiation. Dose rate could be varied stepwise, MLC speed as well as gantry speed can vary continuously in between their technical boundaries.
Tests have to be done in order to evaluate if the machine is capable of varying these characteristics and providing a clinically acceptable interplay and therefore producing the expected dose distribution. Every test focuses on one of the new parameters and has been carried out several times with different output to include different dose exposures and gantry rotation speed.

The detector for these measurements has been the flat panel, or electronic portal imaging device (EPID), which is mounted on the medical linear accelerator. They are of semiconductor type, their main element consisting of silicon. Several correction algorithms have to be applied to the original signal to convert the raw image to a dose distribution which can be analyzed. This is done using a recently in-house developed software plug-in which additionally compensates for the physical behavior of the detector and errors arising from the measurement process.

Resulting images show either dose rate or dose. They have been analyzed using MATLAB functions written in the course of this project.

The test images show correct behavior of the linear accelerator. Deviations have been found but are in a clinically acceptable range taking into account the still missing correction factors of the flat panel detector and inaccuracy of the over all equipment. The next step is to create VMAT test plans based on patient geometries and carry out measurements without a patient. If these tests show good results, first patients can be treated with this technique.

Kurzzusammenfassung

Volumetric Modulated Arc Therapy (VMAT) ist eine relativ neue Bestrahlungstechnik im Bereich der Tumortherapie. Verglichen mit bisherigen Methoden, wie Intensity Modulated Radiation Therapy (IMRT), kommen hier einige zusätzliche Möglichkeiten des medizinischen Linearbeschleunigers zur Anwendung, um eine optimale Bestrahlung des Patienten zu ermöglichen. VMAT liefert eine bessere Dosisverteilung , die eine homogenere Tumorabdeckung ermöglicht und gleichzeitig Risikoorgane idealer schont.

Ziel dieser Arbeit ist es, den ersten Schritt der klinischen Implementierung von VMAT durchzuführen.
Zu Beginn müssen Parameter, die neu zur Anwendung kommen, definiert werden. Diese sind variable Dosisrate, Bewegung des Multileafkollimatoren und der Gantry während der Bestrahlung. Die Dosisrate kann stufenweise angepasst werden, während die beiden anderen Parameter innerhalb ihrer Limits kontinuierlich verändert werden können.
Um zu überprüfen, ob der Linearbeschleuniger die Parameter richtig variiert und koordiniert, so dass die klinisch gewünschte Dosisverteilung erreicht wird, müssen einige präklinische Tests durchgeführt werden. Jeder Test behandelt dabei einen der neuen Parameter und wurde mehrere Male mit unterschiedlichem Dosis-Ouptut durchgeführt, um dessen Einfluss, aber auch den der unterschiedlichen Gantry Rotationsgeschwindigkeiten miteinzubeziehen.

Als Detektor für diese Messungen wurde das Flat Panel, oder Electronic Portal Imaging Device (EPID), verwendet, das an jedem medizinischen Linearbeschleuniger angebracht ist. Die Hauptkomponente besteht aus Silizium, daher fällt er in die Kategorie der Halbleiterdetektoren. Das Panel selbst liefert ein Bild aus Grauwerten, das erst mehrere unterschiedliche Korrekturalgorithmen durchlaufen muss, um ein Bild der Dosisverteilung zu liefern. Dies geschieht mit Hilfe der vor kurzem in-house entwickelten Software, die zusätzlich Fehler auf Grund des physikalen Verhaltens des Detektors, aber auch Ausleseartefakte, kompensiert.

Die aufgenommenen Bilder stellen entweder die aktuelle Dosisrate oder die Gesamtdosis dar und wurden nachher mit eigens geschriebenen MATLAB Funktionen ausgewertet.

Die Auswertungen zeigen korrekte Anwendung der Parameter durch den Linearbeschleuniger. Abweichungen wurden gemessen, diese halten sich aber in einem akzeptablen Rahmen, vor allem wenn man die noch fehlenden Korrekturen des Detektorsignals und die absolute Ungenauigkeit des Gesamtsystems in Betracht zieht. Der nächste Schritt ist die Erstellung von patientenspezifischen VMAT Plänen. Diese werden am Linearbeschleuniger vorerst ohne Patient abgestrahlt, kontinuierliche Messungen werden währenddessen durchgeführt. Zeigen diese Messungen ebenfalls gute Resultate, können die ersten Patienten mit der VMAT Technik bestrahlt werden.

Acknowledgment

First I want to thank **Univ.Prof. Dipl.-Ing. Dr.techn. Gerald Badurek** for his support and for his supervision at the Technical University of Vienna. Without his help this project would not have been realizable.

Additionally I want to thank **Mag. Heinrich Deutschmann** (from the federal hospital in Salzburg) received me at his institute with extraordinarily welcoming and supported and supervised me during the time of the whole project. Every discussion with him provided me with interesting and new facets of this research area and offered continuous input to this project.

Especially I want to thank **DI Ann-Katrin Koch** who constantly supervised and helped me, introduced me to the whole topic with immense patience and perfect advice and additionally guided the whole development of this project.

I want to thank **Dr. Bernd Mößlacher** (from EBG MedAustron GmbH) who arranged this collaboration and provided me the possibility for this project.

In particular I want to thank **my parents and my family** who always supported me, believed in me and are always open for any kind of problems.

Finally I want to thank **my friends and colleges** who cheered me up when necessary or provided a basis for interesting and helping conversations.

Contents

List of Abbreviations

a:Si-H	amorphous Silicon (hydrogenated)
BEV	Beams-Eye View
CT	Computed Tomography
CRT	Conformal RadioTherapy
dMLC	dynamic Multi Leaf Collimator
DVH	Dose-Volume Histogram
EPID	Electronic Portal Imaging Device
eV	Electron Volt
FPPI	Flat Panel Plug-In
LET	Linear Energy Transfer
LinAc	Linear Accelerator
MLC	Multi Leaf Collimator
MLG	Multi Level Gain
MRI	Magnetic Resonance Imaging
MU	Monitor Unit
NSCLC	Non-Small Cell Lung Cancer
NTCP	Normal Tissue Complication Probability
IMRT	Intensity Modulated Radiation Therapy
OAR	Organ at Risk
OER	Oxygen Enhancement Ratio
PET	Positron Emission Tomography
PTV	Planning Target Volume
radART	Research and Development of Advanced Radiation Technologies
RBE	Relative Biological Effectiveness
SALK	Salzburger Landeskliniken
SDD	Source Detector Distance
SSD	Source Surface Distance
sMLC	static Multi Leaf Collimator
VMAT	Volumetric Modulated Arc Therapy

1 Preamble

In 2012 the primary cause of death in Austria has been cardiovascular diseases followed by carcinomas. Nevertheless it can be observed that malignant tumors are still on the rise while cardiovascular diseases decrease nearly every year [1]. Radiation therapy can not prevent the occurrence of malignant tumors but can avert them from spreading over the whole body or even cure the diseased patient.
Since the discovery of X-rays by Wilhelm Conrad Röntgen in 1895 various applications of this radiation have been found and are currently used -mainly but not only in medicine. Only four years afterwards the first patient with a malignancy has been reported to be cured by radiation therapy.
Since then continuous improvements have been achieved in the field of radiation therapy with the main goal to deposit dose in the tumor and spare organs at risk. Cobalt-60 or superficial and deep X-ray therapy have been replaced by mega-voltage therapy or proton and ion therapy. Improvements in imaging quality using CT, MRI or PET had an impact on the quality of patient specific radiation therapy plans, new techniques and approaches to different entities are investigated continuously [2]. All these developments result in higher survival or cure rates for patients and decrease the rate of secondary malignancy caused by radiation therapy.
Increase in processing power of computers has provided new possibilities in radiotherapy planning. Optimization can be done by an algorithm specially developed for radiation therapy in a short time with little effort from the planner. Formerly forward planning of 3D conformal radiotherapy (3D-CRT) has been extended to computer inverse planned techniques like intensity modulated radiation therapy (IMRT) and volumetric modulated arc therapy (VMAT).
Using all the possibilities of the medical equipment and digital tools an ideal plan can be set up for each patient and is adapted in the course of the radiotherapy with the help of daily imaging.
Although the extended use of technical possibilities is endorsed by society special care has to be taken when using these facilities. It is crucial to perform regular checks on all parts of the equipment especially before part of it is used clinically but even if they are in continuous use and do not show any undesired behavior.

This project deals with the clinical implementation of VMAT, including all machine tests necessary to release this method to be used in patient specific planning and treatment.
Machine parameters which require testing have been identified and test plans have been set up. These plans were radiated directly on the medial linear accelerator (LinAc). Measurements have been done with the semiconductor detector mounted on the LinAc. The main element of these detectors, often called flat panel or electronic portal imaging device (EPID), consists of silicon. A special software has been written beforehand to measure absolute dose with the EPID. After successful evaluation of the images clinical evaluation of VMAT can be taken to the next step which includes evaluation of real treatment plans and can then be released for clinical use.

2 Physical Basics

2.1 Medical Linear Accelerator

The linear accelerator is a device that uses high-frequency electromagnetic waves to accelerate charged particles such as electrons to high energies through a linear tube [3].
Medical or clinical linear accelerators have become the dominant machine in radiation therapy. They are used to produce ionizing radiation which is essential for the treatment of tumors or other malignancies. Using the accelerated electrons superficial malignancies can be treated, including a conversion step and applying X-rays allows for concentrating the dose to deep-seated tumors.
The accelerated electrons can reach a final kinetic energy in the range of 4 to 25 MeV. Therefore modern clinical linear accelerators will provide two photon energies (typically 6 and 10 or 15 MV) and several electron energies in this range. Earlier generations did not include the direct usage of electrons and could not reach energies as high as the modern machines [4].
Electrons are accelerated through the same potential difference various times, which classifies the linear accelerator as a cyclic accelerator. The term linear accelerator has its origin in the linear path the electrons follow during their acceleration.
Two types of medical LinAcs are currently in use which can be distinguished by the mode of the electromagnetic waves used for acceleration of the electrons. Either standing wave or traveling wave accelerator design can be built, each having their own characteristics, including advantages and disadvantages.
A medical linear accelerator allows treatment of the tumor from various directions with ionizing radiation. It is normally mounted isocentrically and has five basic components [4] (see figure 2.2).

- Gantry
- Gantry Stand or Support
- Modulator Cabinet
- Patient support assembly, i.e. treatment couch
- Control Console

Figure 2.1 shows a bloc diagram including all major components of the accelerator itself.

A power supply provides direct current to the modulator which forms pulses and directs them to both the electron gun and the magnetron or klystron.
The magnetron produces microwaves of several microseconds duration with a repetition rate of up to 400 pulses per second. In the electron gun electrons are produced simultaneously and are injected into the accelerator structure which is also called the waveguide.
In the accelerator copper discs with varying spacing separate the evacuated structure. The electrons interact with the electromagnetic field of the microwaves and gain energy from the sinusoidal electric field. Depending on the point of injection the acceleration path length can be changed leading to different final energies.

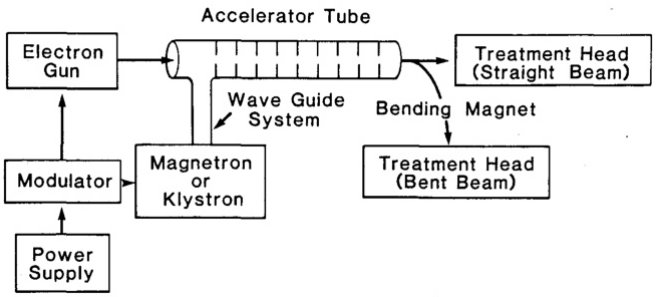

Figure 2.1: A block diagram of typical medical linear accelerator [3]

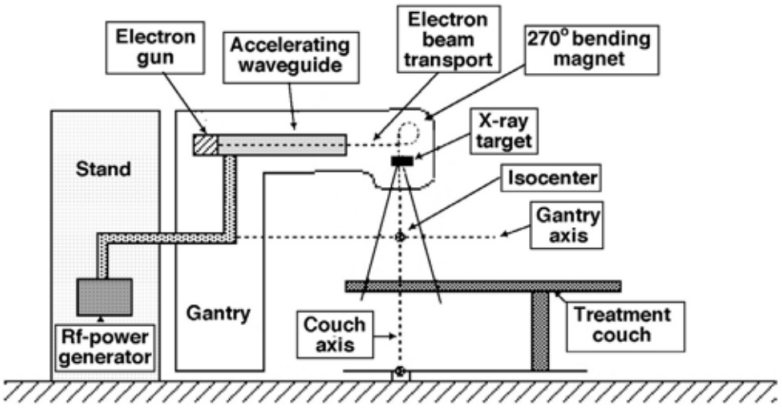

Figure 2.2: Design configurations for isocentric medical LinAcs [4]

Bending magnets focus the emerging electron beam and lead them to the treatment head. [3]

The treatment head is the origin of the clinical electron or X-ray beam. It converts the primary beam which emerges from the accelerator to a clinically usable treatment beam and strongly influences its characteristics.

The incident beam is bent 270° by a bending magnet assembly. Then it impinges a target which converts the electron beam to an X-ray beam. This target can be removed when treating a patient with electrons. On a carousel several filters can be applied to the emerging beam, an example would be a flattening filter or other scattering foils to influence the beam profile. Before the beam is shaped an ionization chamber continuously monitors the dose of the beam. Collimators, including multi leaf collimators (MLCs), are used to shape the beam into the desired dimensions before it exits the treatment head. [5]

Figure 2.3 shows the ELEKTA LinAc used for this project. The gantry is at 180°, the flat panel detector is opposed to the gantry, kV imaging system is at 270°/90°.

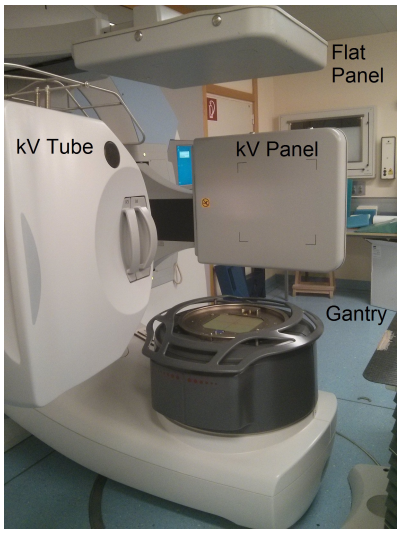

Figure 2.3: Elekta Synergy Linear Accelerator at Federal Hospital in Salzburg; Gantry at 180°

2.2 Interaction of Photons with Matter

Photons or X-rays are indirect ionizing radiation. During their interaction process they produce secondary particles which can excite or ionize surrounding tissue. Interaction processes include fully or partly absorption and scattering. When the photons' energy surpasses a certain level the forces on the nucleus or bound electrons can cause ionization further leading t biological damage. These interaction processes shall be described briefly.

- Attenuation
  Attenuation describes the overall loss of intensity of the primary photon beam when it passes through matter. It follows the attenuation law

$$I = I_0 \cdot e^{-\mu d} \tag{2.1}$$

  where I_0 is the intensity of the primary beam, I the current intensity, d the thickness of crossed matter and μ is the attenuation coefficient. This coefficient is material dependent and consists of all interaction processes of the photon beam with matter. On the other hand it can be associated with the atomic number A, the cross section σ_a, the density of the material ρ and the Avogadro constant N_A. μ is specified in [1/cm].

$$\mu = \frac{N_A}{A} \cdot \rho \cdot \sigma_a \tag{2.2}$$

$$\frac{\mu}{\rho} = \frac{\sigma_{coh}}{\rho} + \frac{\tau}{\rho} + \frac{\sigma_c}{\rho} + \frac{\pi}{\rho} \tag{2.3}$$

  The first coefficient represents Rayleigh Scattering, the other three are referred to as principal interactions of a photon with an atom and shall be described below.

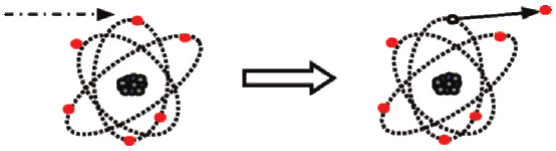

Figure 2.4: Schematic representation of the photoelectric effect; red dots are electrons, dashed lines represent photons, continuous lines the path of the ejected electron [8]

- Rayleigh Scattering σ_{coh}
  Rayleigh scattering, also referred to as coherent or classical scattering, occurs with low photon energies and high atomic number Z of the scatter material. The incoming photon interacts with a bound electron from the shell of the atom leading to oscillations of the latter. These oscillations emit a new photon with the same energy and frequency as the incident photon. Therefore the atomic shell remains unchanged.
  This effect is of no interest in radiation therapy as it leads to no biological changes and therefore has no effect on the biological tissue.

- Photoelectric Effect τ
  A photon can "collide" with an electron and thereby transfer all its energy to the electron which is ejected from the atom. This effect is called the photoelectric effect. In 1921 Einstein won the Nobel Prize for his explanation of the photoelectric effect.
  The photon is completely absorbed by a bound orbital electron, its energy transferred. Every electron has a binding energy, depending on its occupied shell position. This energy has to be overcome for the electron to escape the atomic structure. See figure 2.4 for a sketch of the photoelectric effect.
  The difference of the original energy of the photon and the binding energy of the electron is converted to kinetic energy of the electron (see equation 2.4). An ionized atom remains which can undergo further processes. As a 'hole' is produced other electrons from outer shells can fill that vacant place, emitting characteristic radiation themselves.
  The angular distribution of the photo electron is energy dependent. The higher the energy the smaller the emission angle becomes.
  The photoelectric effect mainly occurs with electrons of the inner shells.

$$E'_{electron} = E_{photon} - E_b \tag{2.4}$$

  The coefficient for the photoelectric effect, the photo absorption coefficient, is τ, which can also be found in equation 2.3. The dependency of the photo absorption coefficient is given by equation 2.5.

$$\tau \propto \rho \frac{Z^n}{A} E^{-3} \tag{2.5}$$

  where $n \approx 4.6$ for light elements and $n \approx 4$ for elements with high atomic number.

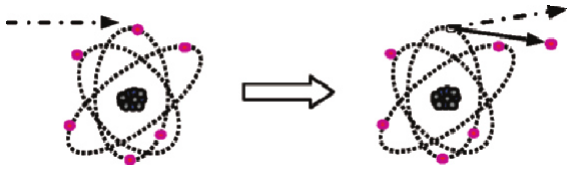

Figure 2.5: Schematic representation of a Compton interaction of a photon with an atomic electron [8]

- Compton Effect σ_c
  The Compton effect can also be referred to as incoherent scattering. In contradistinction to the photoelectric effect, where the photon is completely absorbed, in the occurrence of Compton effect the impinging photon transfers only part of its energy and momentum to the electron. It continues along an altered path with reduced energy and momentum and is therefore scattered. The energy and momentum difference of the photon is transferred to the electron which is ejected from the atom (see figure 2.5 for a sketch). The Compton effect leads to an ionized atom as well.
  From the law of energy conservation we get

$$E'_{electron} + E'_{photon} = E_{photon} - E_b \tag{2.6}$$

  where E' refers to the energy after the occurrence of the Compton effect. Normally Compton effect occurs with electrons from the outer shells which are loosely bond. Photons can be scattered over the full range of angles but tend to be scattered forwardly for higher energies. Angles of electron ejection are always within 90° of the near-forward direction.
  The transferred energy from the photon to the ejected electron depends on the energy of the incident photon.
  The Compton attenuation coefficient σ_c is proportional to Z/A of the absorber and is therefore often approximated by 1/2 for most stable and light elements. Hence it is nearly independent on the atomic number. The overall dependency is described by

$$\sigma_c \propto \frac{Z}{A} \cdot \rho \cdot E^{-1/2} \tag{2.7}$$

  Using the laws of conservation of energy and momentum an equation can be derived describing the dependency of the primary and scattered energy of the photon.

$$E' = \frac{E_0}{1 + \frac{E_0}{m_e c^2}(1 - cos(\phi))} \tag{2.8}$$

  E' is the energy of the scattered photon, E_0 its primary energy, m_e the mass of an electron and ϕ the scattering angle.

Figure 2.6: Schematic representation of pair production [8]

- Pair Production π
  The third principal interaction is pair production. If the photon gets close enough to the atomic nucleus it interacts with the electromagnetic field of the protons. This interaction can lead to the extinction of the photon and the creation of a pair of particles: namely an electron and a positron, which is the antiparticle to the electron.
  See figure 2.6 for a sketch.
  The energy of the incident photon is used to create two particles, which is a dramatic example of the equivalence of mass and energy as stated by Einstein. As both particles have a rest mass, there is a threshold for the minimum energy of the photon for the occurrence of pair production. It is given by the sum of the two rest masses, namely $2 \cdot 0.511MeV = 1.022MeV$. The remaining energy is transferred to both the electron and the positron as kinetic energy.

$$E'_{electron} + E'_{positron} = E_{photon} - 1.022MeV \tag{2.9}$$

  The pair production coefficient, π, depends on the photon energy, the density of the material and the factor Z^2/A, but is only valid for photon energies higher than $1.022MeV$ as mentioned above.

$$\pi \propto \rho \frac{Z^2}{A} log(E_\gamma) \tag{2.10}$$

  Slow moving positrons later combine with electrons producing two photons with $0.511MeV$ each. These photons are ejected in opposite directions. The process of electron positron reaction is called annihilation.

The probabilities of each effect on its own was already mentioned above. To reach a better understanding of importance of each effect in combination with the others, a short discussion about the appearance of each effect depending on external variables shall be given.
Figure 2.7 shows the importance of each principal interaction process depending on the energy of the incident photon. The likelihood of photoelectric effect is highest in low energy regions. Above $0.05MeV$ Compton effect is the dominant interaction process. Pair production has a threshold and is most important for high energy photon interactions.
In the range of clinically used radiation, from about 0.3 to 20 MeV, Compton effect shows the highest importance. Therefore the behavior of most therapeutic photon beams is explained by physics of Compton interactions alone [8].

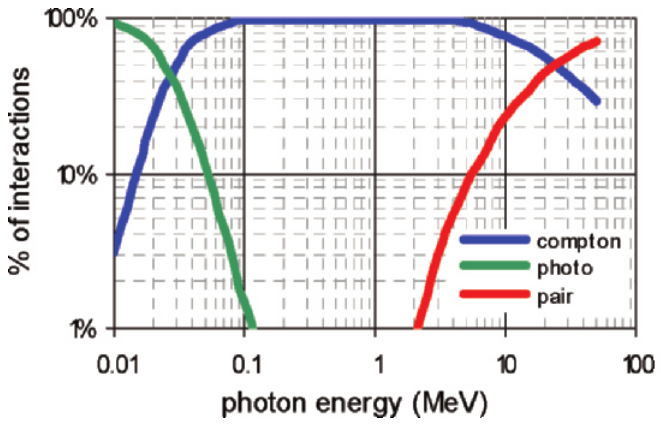

Figure 2.7: Relative importance of photoelectric effect, Compton interactions and pair production in water (both axes are logarithmic) [8]

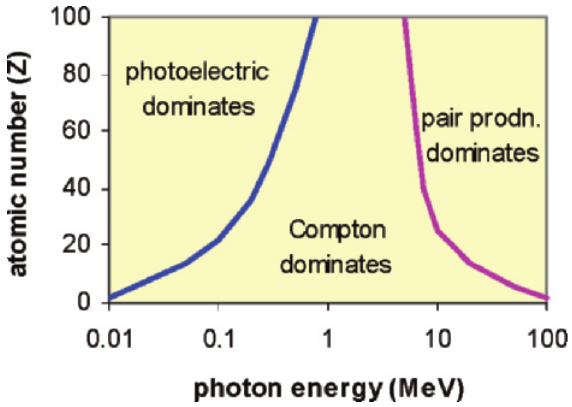

Figure 2.8: Domains of dominance as a function of photon energy and atomic number [8]

The likelihood of occurrence of the principal interactions is dependent on the atomic number Z as well. This was already mentioned in relations above. For photoelectric effect, the probability is approximately proportional to Z^3, for Compton interactions virtually independent and for pair production approximately proportional to Z.
Although pair production has its threshold at 1.022 MeV, it can be seen that the likelihood for this effect is basically zero around this energy.
The areas of dominance of the basic interactions as a function of photon energy and atomic number is shown in figure 2.8. The photoelectric effect dominates in areas of low energy and higher Z, it therefore dominates diagnostic imaging of bones. For therapeutic photon beams Compton effect is the dominant interaction process for all tissues and body parts.

2.3 Radiotherapy

Radiotherapy is an approach used to cure cancer, often combined with other treatment techniques like chemotherapy or surgery.
Radiation which penetrates the human tissue, i.e. the cells, can cause lethal damages, on one hand by forming radicals and on the other by direct breaking of chemical bonds in the DNA. The higher the applied dose, the higher is the probability for cell death -both for the healthy and the malignant cells. Therefore one major goal is to spare normal and healthy tissue from dose exposure.
Dose is a measure of radiation exposure. It depends on multiple factors, including radiation type, chemical composition and tissue type. Various units have been established and will be discussed in the next section.
As mentioned above, one major goal is to spare healthy tissue. A fortunate fact is that tumor cells seam to be more sensitive to exposure of radiation than healthy cells. Additionally the ability to regenerate itself and repair damages is higher in normal tissue. These effects have been confirmed but can not be fully described or understood. They are reinforced by applying the dose in several small fractions.
An adverse circumstance is the low oxygen concentration in tumor tissue. Oxygen easily forms radicals and thereby increases the effect of radiation to the surrounding atoms and molecules. Due to the lack of it in tumor tissue radiation effects are decreased. For counteraction radio-sensitizers can be used.

2.3.1 Dose Terms

Radiation measurements and investigation of effects require the definition of various units which describe the radiation field at a certain point of interest. Radiation dosimetry deals with methods for quantitative determination of deposited energy in a given medium by directly or indirectly ionizing radiation [9]. Some important quantities and units shall be described in this section.

KERMA
KERMA is an acronym for kinetic energy released per unit mass. It is defined by equation 2.11, as the quotient of dE_{tr} by dm, where dE_{tr} is the sum of the initial kinetic energies of all the charged ionizing particles (electrons and positrons) liberated by uncharged particles (photons) in a material of mass dm [3].
It does not include effects of secondary processes, therefore only taking into account the transferred energy from the indirectly ionizing radiation to directly ionizing radiation. Differences to the absorbed dose can arise due to secondary particle interactions with the surrounding material which have not been included in the calculation. Assuming equality of secondary particles KERMA is the perfect measure for absorbed dose.

$$K = \frac{dE_{tr}}{dm} = \frac{dE_{tr}}{\rho dV} \tag{2.11}$$

The unit of KERMA is joule per kilogram [J/kg], and is therefore equivalent to gray (1Gy = 1 J/kg).
KERMA is dependent on the irradiated material, it therefore takes on different

values even when the radiation quality and radiation type are the same. It is essential to define a material when specifying a certain level of KERMA. The differences arise from varying binding energies of secondary particles like orbital electrons or protons from the nucleus [10].

Energy Dose
Energy Dose, also referred to as absorbed dose, is defined as the quotient of absorbed energy dE_{abs} per mass dm. In contrast to KERMA it can be applied to any type of radiation, independent on whether it is directly or indirectly ionizing.
Energy dose is the mean absorbed dose of a certain material with density ρ during an irradiation divided by the mass of the irradiated volume (see equation 2.12). dE_{abs} is defined as the sum of the energy entering the volume of interest minus all the energy leaving the volume. It takes the first interaction process (where KERMA is released) as well as secondary processes into account.

$$D = \frac{dE_{abs}}{dm} = \frac{dE_{abs}}{\rho dV} \tag{2.12}$$

The old unit for energy dose was rad (=radiation absorbed dose), the currently used unit is gray (Gy), where 100rad = 1Gy.
Energy transfer mainly occurs due to secondary particles which have a material dependent binding energy which has to be overcome. Therefore this unit is dependent on the absorbing material. [10]

Ion Dose
Ion Dose is defined in air, as the due to radiation directly or indirectly produced electric charge in a certain volume of air divided by the mass of this volume [10]. This relationship is shown in equation 2.13.

$$J = \frac{dQ}{dm} = \frac{dQ}{\rho dV} \tag{2.13}$$

The unit of the ion dose is C/kg.

Equivalent Dose
Equivalent dose is defined as the product of absorbed dose D in an organ and a dimensionless quality factor Q. Therefore, equivalent dose has the same unit as energy dose.

$$H = Q \cdot D_w \tag{2.14}$$

The value Q is influenced by the radiation quality of the beam and the observed tissue type and takes into account the different biological effectiveness of a certain radiation quality on a certain organ. The value of Q is defined by international committees.

Dose Rate
Dose rates are the differential quotients of dose per time. Dose rate can be defined for both energy dose and ion dose.

$$\dot{J} = \frac{dQ}{dmdt} = \frac{dQ}{\rho dV dt} \tag{2.15}$$

$$\dot{D} = \frac{dE_{abs}}{dmdt} = \frac{dE_{abs}}{\rho dV dt} \tag{2.16}$$

Regarding radiation therapy, dose rate is a very important quantity. It is measured as the maximum value of energy dose in a water phantom in 100cm distance in a field of size 10x10cm [11]. It is given in Gy/s.

2.3.2 Radiation Biology

Interactions of radiation with cells is based on energy transfer which can result in various damages in the cell - from biological and biochemical alterations to instant cell death. After primary absorption - the physical interactions - other physical-chemical, biochemical and biological interactions take place which heavily depend on the characteristics of the incident radiation.
A precondition for biological changes is that the radiation has to be ionizing, therefore its energy has to be high enough to ionize molecules or atoms in the tissue in question.
The first interaction process is the physical phase, where primary interactions take place. Radiation is absorbed locally based on the primary interaction processes. The results are ionized or activated atoms and molecules. In the physical-chemical phase energy gets transferred to the local surrounding by thermodynamical interactions. This further energy transfer can result in structural and functional changes in the biomolecules of the cell. Biological changes include long-term changes in the cell. Radicals diffuse through the cells, interact with biomolecules in the cell and result in damages. These damages can affect whole chromosomes or only parts of the DNA which further leads to mutations, denaturation of proteins and cell death.

The final goal of radiation therapy is to sterilize the tumor cells in the human body. To achieve this, the DNA of the cells has to be irreversibly damaged.
This can be accomplished in two ways: either direct or indirect radiation damage depending on the interaction with the DNA.
Direct damaging of the DNA can be the result of single or double strand breaks, but also alterations of the present bases or sugars or the breaking of hydrogen bonds in the double helix. Due to the low concentration of DNA in the whole irradiated volume, this interaction process is rare.
Indirect damaging includes an intermediate step. The incident radiation builds radicals in the body, mostly out of oxygen which is highly present in the cells. These radicals further interact with the DNA or other important components of the cell resulting in damages. [10]
The effect of a certain kind of radiation is therefore not only dependent on the radiation type but also on other factors like oxygen concentration in the irradiated volume. Some factors which include these parameters shall be discussed briefly.

Linear Energy Transfer LET
The Linear Energy Transfer coefficient is a measure for ionization characteristics in a volume. It is described as the local absorbed energy along a certain path length. To further define the term "local" a cut-off energy has been defined which is given as an index when used. [9]

$$L_{\infty} = \frac{dE}{dx} \tag{2.17}$$

$$L_{\triangle E} = \left(\frac{dE}{dx}\right)_{\triangle E} \tag{2.18}$$

A distinction can be made due to the LET factor. Loosely ionizing radiation has low LET and includes gamma radiation as well as ultraviolet or X-ray radiation. Densely ionizing radiation has a high LET, which is a property of neutron or α radiation as well as ions and protons.
Densely ionizing radiation has a higher biological effectiveness than loosely ionizing radiation, even when the same energy dose is applied to the tissue. [10]

Relative Biological Effectiveness RBE
The relative biological effectiveness is used to compare two different radiation types. It is defined as the ratio of absorbed dose of a reference radiation D_{ref} to the absorbed dose of a comparative radiation D_u which induce the same biological effect under the same conditions.

$$RBE = \frac{D_{ref}}{D_u} \tag{2.19}$$

As reference radiation low LET radiation like 250keV X-rays or radiation from ^{60}Co is normally used. The RBE varies not only with radiation type but also with applied dose or examined biological effect.

Oxygen Enhancement Ratio OER
As mentioned above the occurrence of high oxygen levels has the ability to increase the effects of radiation through building of radicals which further interact with cell molecules. The ratio of the necessary doses to achieve a certain effect with and without oxygen is called the oxygen enhancement ratio OER.

$$OER = \frac{D_{noO_2}}{D_{O_2}} \tag{2.20}$$

The OER can take values up to two to three when low LET radiation is applied and decreases to one for higher LET radiation.

Cells have the ability to regenerate themselves. Not only can they repair single strand but also double strand breaks although with a much lower probability. A positive fact is that normal cells have a much higher ability for regeneration than tumor cells.
This fact is one of the reasons why radiation therapy is fractioned. The dose which should be applied to a tumor is split in many small fractions, delivery is performed regularly over a period of some weeks.

This has four basic reasons:
1. Recovery: Giving the tissue time in between two irradiations helps the normal cells to regenerate themselves. As they have a higher ability to repair damages on their own, they have a higher survival rate than tumor cells when fractioning is applied. The latter normally regenerate themselves slower if they do so.
2. Re-oxygenation: The concentration of oxygen, which plays a major role in the effectiveness of radiation therapy, is lower in tumor regions. Cells on the border of the tumor area are affected first, others which are located in deeper regions are re-oxygenated in between the given fractions.
3. Redistribution: Cells have different sensitivity to radiation depending on the state of the cell cycle they are in. During or just before mitosis they are most sensible. Fractioning allows to hit more cells during this point of the cell cycle.
4. Re-population: In between two given fractions new and healthy cells can take the place of the tumor cells which have been sterilized in the previous fraction. Dead cells are washed out, new ones come in and take their place. [10]

Fractions are normally given daily, five days a week. One fraction holds about 200cGy for the tumor region, resulting in durations of the whole radiation therapy of three to five weeks depending on the prescribed dose which can be found in the range of 4500cGy to 9000cGy. Shorter periods are achieved through hyperfractioning, by applying two fractions a day, or by increase of dose for a single fraction (hypofractioning).
More information can be found in [10], [11].

2.3.3 Tumor Biology and Volume Concepts

Tumor staging is used to describe the progress of a malignancy and is done by the radio oncologist.
One system used for staging is the TNM staging. T describes the size of the primary tumor, N describes nearby lymph nodes that are involved and M describes distant metastasis. Adding a 'c' before the staging defines the tumor as clinical, a 'p' classifies it as pathological. An example would be cT2N1M0, which describes a clinical tumor of rather small size with only regional lymph node metastasis present and no distant metastasis. [13]

To treat a tumor with radiation a certain dose is prescribed to the tumor volume which should be as uniform as possible to achieve the best results. On the other hand normal and healthy tissue should be spared as good as possible. Different tissue and organs vary in their sensibility concerning radiation dose. Depending on the organ at risk (OAR) certain constraints have to be fulfilled to not harm or destroy the healthy and vital organ. These doses can be defined by using the normal tissue complication probability (NTCP). These values arise from experience of many investigations and give an estimate of how much dose an organ can bear without losing its functionality. Based on these values, constraints and objectives are set up for radiation therapy. [14]

A plan is set up where the beam arrangement is shown with all necessary characteristics (how this is done is described in the next section) with the main goal to deliver the prescribed dose to the tumor volume and to spare the OARs as good as possible. Therefore CT imaging is done before the plan is set up, the physician delineates target volumes and organs at risk. This process creates

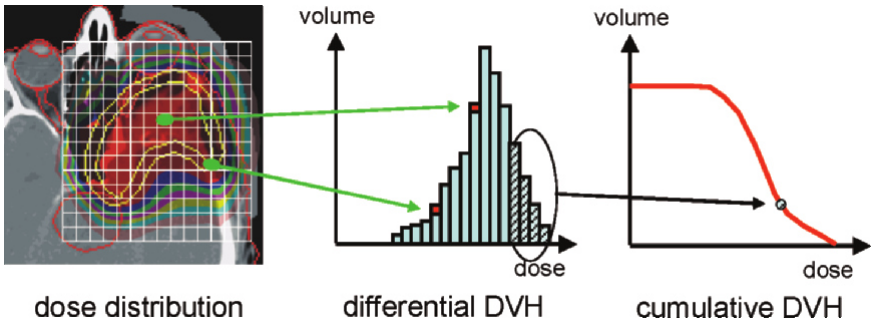

Figure 2.9: Illustration of how differential and cumulative DVHs are constructed [8]

volumes for every delineated structure. The dose which is applied to every structure is calculated and can be depicted in the dose volume histogram (DVH). This graph shows the distribution of dose within a particular volume of interest (see figure 2.9 for an example). There is a cumulative and a differential DVH. From the cumulative DVH can be concluded what percentage of a volume gets at least which dose level, whereas the differential DVH shows how many percent of a volume get which dose level. [8]

2.3.4 Planning Methods used for Radiotherapy

In the last decades radiotherapy planning has evolved from surface anatomy-based planning to 3D image-based planning. Several technical improvements had an impact in planning, including CT, PET and their fusion as well as the development of simulators and the drastic increase in computer processing power.
Every treatment planning process starts with imaging. Anatomic information is obtained by transverse slice images. Imaging is done with CT as it provides the attenuation factor necessary for dose calculation, sometimes other modalities like PET or MRI are included. For easier evaluation of all gathered information these images are fused by an overlay of anatomical landmarks. The radiation oncologist then defines the volumes of interest in each slice of the image data set. These volumes include the target volume with sufficient margins (which is called the PTV -planning target volume) to compensate for uncertainties and other anatomical structures. The prescriptions for minimal dose to the target volume and maximum dose to the organs at risk (OAR) are done by the physician as well.
There are two basic approaches to develop a treatment plan. The first is manual or forward planning where the treatment planner decides on all modifiable components to best fit a desired dose profile for the whole volume. Here the planner is the one who creates a treatment plan. The second approach is computer-driven or inverse planning. Using this approach the planner lines out which dose profiles he or she would like to have in a certain volume of interest and only gives small limits to the adjustable parameters of the machine. The computer then calculates these parameters and produces the treatment plan.

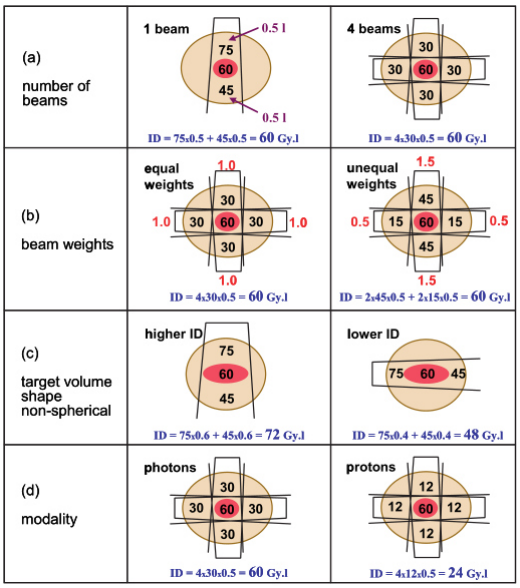

Figure 2.10: Schematic presentation of a number of different treatment approaches and their impact on integral dose. A very crude estimate of the integral dose (ID) is shown under each sketch. [8]

3D-CRT

3D-CRT stands for three dimensional conformal radiation therapy. The treatment is planned on a sliced image set which can be converted to a 3D representation of the patient. 3D-CRT is a forward planning method.

After the structures have been delineated on the image set of the patient, the treatment planner is responsible for the selection of beam directions and designing beam apertures. For his support to choose the right parameters, beams-eye-view (BEV) images can be created. These images show all important structures in a plane perpendicular to the beam and therefore changes depending on the angle of the beam with respect to the patient.

As the intensity of a radiation beam decays exponentially in tissue (see equation 2.1) choosing only one beam would always lead to the dose maximum being located some centimeters underneath the skin. Therefore beams from various directions are selected which superimpose in the region of the target and spare the volume before and after the tumor (see figure 2.10). This figure also shows a measure of the integral dose, which gives an estimate of the total energy deposited in the patient outside the target volume. If target coverage is the same for two plans the better plan can be identified by its smaller integral dose.

When the beam directions have been defined, treatment planning moves on to aperture design. Not only can the gantry rotate around the patient covering an angle of 360°, the beam can additionally be shaped. To achieve a certain field form, collimators are used. Collimators allow the rectangular shaping of the beam. Frequently, machines are additionally equipped with multi leaf collimators (MLCs) -see figure 2.11. MLCs measure 0.5 to 1 cm in width at the isocenter and are installed in the gantry head after the primary collimator.

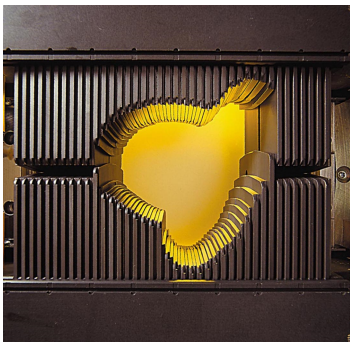

Figure 2.11: Millenium MLC, Varian [6]

Therefore they offer almost any kind of beam shaping in one dimension of the beam. To further enhance beam shaping the collimator can be rotated as well. Primary collimator and MLCs are manually or automatically shaped so the beam form fits the target volume plus a variable margin. The delivered radiation has a uniform intensity profile. The only possibility to influence that fact is to add a wedge or compensator.
After setting of gantry angle and collimator positions, dose in the patient is calculated. In an iterative process these parameters are further varied to achieve a plan which attains all clinical goals. [3]

IMRT
Intensity Modulated Radiation Therapy (IMRT) belongs to the class of inverse treatment planning methods.
The principal to use beams from different directions to get a superimposition of dose intensity in the target volume is kept. The treatment planner defines certain specific directions which are normally equally distributed over the whole arc. To achieve intensity modulation -as the name suggests- each direction does not only have one configuration of collimator and MLCs. Beams with non-uniform profile are created and optimized to deliver a high dose to the target and spare the surrounding normal tissue.
The treatment planner mainly defines the beam angles and does not influence the shaping of the beam profiles. Goals for both PTVs and OARs are defined, each of these goals is weighted by a certain factor depending on the importance the planner wants to set for this goal.
On this basis the computer optimizes the treatment plan by dividing each beam into a number of beamlets and on the same time minimizing the cost function which is based on the predefined goals and their weights. [3]
The treatment plan is therefore created inversely to best fit the desired criteria. For the creation of non-uniform intensity profiles for each beam two methods can be used which shall be described briefly.

- static MLC
  Using the sMLC (static MLC) approach each beam is split up into segments with different MLC configurations. Therefore each field is subdivided into subfields which each have a uniform intensity profile. Each

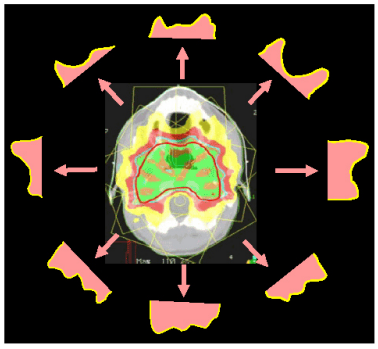

Figure 2.12: Example for an IMRT treatment plan representation [7]

subfield is delivered one at a time. The beam is turned off while the leaves move from one subfield arrangement to the next one. As the segments can have different durations of irradiation and therefore different delivered dose for their shape the overall intensity profile for one angle is not uniform any more but shows non-uniform distribution. [3]
After all subfields of one field have been delivered the gantry moves on to the next angle- again while the beam is turned off.
This method is also called "step-and-shoot" IMRT due to the behavior of irradiation of all fields and segments.
Maximum number of segments as well as minimum MU per segment and minimum field size can be limited by the treatment planner.

- dynamic MLC
  The dMLC (dynamic MLC) approach does not use static fields and segments for one beam angle. Instead the leaves sweep simultaneously and unidirectionally over the whole desired distance while the beam is on. Non-uniform intensity distribution is achieved through variation of MLC speed over time. Dynamic MLCs can move with a speed greater than 2cm per second, changes in the speed can be achieved very accurately.
  The beam is constantly on during the movement of the MLCs. After they have swept over the whole irradiated area the beam is turned off and the gantry moves to the next angle where the procedure of sweeping leaves starts again.
  This method is also called "sliding window" approach to describe its characteristics. [9]

An example for an IMRT treatment plan is shown in figure 2.12.
The process of finding an acceptable plan which satisfies all required goals is again a try and error process. Weights of the goals as well as other limiting factors can be changed to get an optimal treatment plan.
Therefore the time needed to get to the final version of the treatment plan always depends on the experience of the treatment planner, independent on the modality of planning.
Volumetric Modulated Arc Therapy (VMAT) is an extension of IMRT and will be discussed in the following section.

3 Volumetric Modulated Arc Therapy VMAT

Volumetric Modulated Arc Therapy, shortly referred to as VMAT, is a newly developed radiation therapy technique which is assigned to the category of rotational methods. The algorithm was introduced by Karl Otto in 2007, first publications were done in 2008 [16].
The goal was to create an optimization platform to deliver highly conformal dose distributions in one single gantry arc. Earlier rotational techniques were IMAT (Intensity Modulated Arc Therapy), where one sliding window is used for one arc (MLCs only move unidirectional during one rotation) and multiple arcs are applied to achieve the desired dose distribution, and Tomotherapy (helical therapy HT), where multiple arcs are used in a fan-like manner. Both techniques implied their disadvantages, mainly because of their long duration due to the multiple necessary arcs. VMAT should produce a satisfactory dose distribution in only one single arc, therefore sparing dose output and time needed for the radiation therapy.
In this section this new technique shall be discussed in detail.

3.1 Basics

Since its introduction IMRT techniques have been widely used in clinics all over the world. Further improvements resulted in the usage of more beam directions and exploitation of all available possibilities. Nevertheless IMRT also entails some disadvantages. The more beam angles are used the longer the treatment of the patient takes and the more monitor units (MU) are used. This can result in intrafractional motion, less patient comfort, less patient throughput and a higher integral dose which can cause secondary malignancies [17]. Early rotational techniques implied their own shortcomings despite their enhanced target coverage.
To encounter these disadvantages and additionally produce a more efficient technique VMAT was created. In particular, VMAT is designed in a way that the optimized plans are delivered efficiently in a single arc over 360°, with a high dose conformity and with high resolution sampling of the beam directions during planning [16].
Being an extension of IMRT VMAT is also planned inversely. The user specifies certain parameters and defines goals regarding the dose distribution, the computer produces the optimal plan based on these assumptions. One arc turned out not to be sufficient for all cases, sometimes a second arc may help to achieve an acceptable plan.Using more than two arcs would annihilate the advantage of short treatment duration.
Different vendors provide VMAT with various names: Varian with RapidArc, Philips with SmartArc and Elekta with Elekta VMAT. A LinAc has to be made ready for the application of this technique which is done via the software. Then testing and first patient treatment can start.

The principles of VMAT are presented roughly in figure 3.1.
Control points are spread equally over the whole arc. The number of control points can be defined by the treatment planner. At every control point the position of the MLCs is defined. In between these borders the MLCs move continuously with constant speed from one position to the next. Constraints have

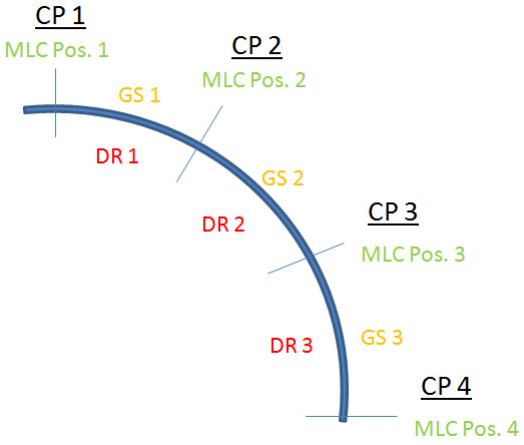

Figure 3.1: A coarse presentation of the VMAT principle. CP = Control Point, MLC Pos. = MLC Position, GS = Gantry Speed, DR = Dose Rate

to be set concerning leaf motion due to technical limitations of leaf speed. The finer the control points are set, the less are the MLC positions allowed to differ between two control points.
Gantry speed is constant between two control points but can vary along the arc. This can be necessary to quickly pass an area where an organ at risk is located directly in the beam direction before the target. Significant changes in gantry speed should be handled with care due to problems with accurate delivery.
The dose rate varies as well, but is constant between two control points and therefore provides an additional possibility to distinguish different arrangements of PTVs and OARs depending on the beam angle.
The dose delivered between two control points can be calculated on basis of elapsed angle, gantry speed and dose rate.

3.2 Inverse Treatment Planning

VMAT planning involves an inverse optimization process done by a computer program. The original idea and algorithm were developed by Karl Otto in 2007 [16]. Details about the optimization process can be found in this paper. A short overview shall be given here, based on this publication. Further information concerning planning with an available computer program, f.e. Raystation, property of RaySearch AB, is provided in [18].
VMAT optimization follows the classical approach of other planning methods. In the first step optimal fluence maps are created followed by a MLC leaf sequencing step which includes MLC positioning and MU weighting as optimization parameters. This approach is called aperture-based.
The cost-function is dependent on dose-volume-constraints which can be defined by the planner. Desired minimum or maximum values are chosen (f.e. 66Gy to 95% volume) for both PTVs and OARs. Each of this constraint is given a certain weight depending on the importance of the goal. The cost is then

Parameter	Computer Optimized	Manually Chosen	Constrain	Typical Value
Dose Rate	x		x	7 - 600 MU/min
MLC Position	x		Velocity	3cm/s
Gantry Speed	x		x	6°/s
Control Points		x	x	60-180 per arc
Arc		x	x	Single, Double, Multiple
Delivery Time	x	x	x	Maximum User-Defined
Dose-Volumes		x		f.e. 67Gy to 95%V
Iterations		x		max. 100
Leaf Motion		x	x	max. 0.5cm/deg

Table 3.1: Parameter Characteristics VMAT Optimization

calculated using a standard quadratic dose difference function multiplied by the priority value. The total cost is the sum of all individual cost values.
Optimization constraints depending on technical machine restrictions limit the optimization to some extent. MLC shapes and motion as well as MU values have to be physically achievable. For example, overlapping leaves or negative MU weights are rejected.
The so called efficiency constraints are defined in terms of gantry rotation angle,

$$\frac{\triangle x}{\triangle \theta} \leq \left(\frac{dx}{d\theta}\right)_{max} \tag{3.1}$$

$$\frac{\triangle MU}{\triangle \theta} \leq \left(\frac{dMU}{d\theta}\right)_{max} \tag{3.2}$$

where x is the MLC position, MU the MU weight and θ the gantry angle. Limiting these values also enhances accuracy of the delivery.
The constraints can be calculated from machine parameters:

$$\left(\frac{dx}{d\theta}\right)_{max} = \left(\frac{dx}{dt}\right)_{max} \Big/ \left(\frac{d\theta}{dt}\right)_{max} \tag{3.3}$$

$$\left(\frac{dMU}{d\theta}\right)_{max} = \left(\frac{dMU}{dt}\right)_{max} \Big/ \left(\frac{d\theta}{dt}\right)_{max} \tag{3.4}$$

Meeting these constraints each optimization iteration involves randomly selecting a control point, changing MLC position or MU weight and recalculation of the cost function. If the cost function value is decreased by this alteration it is kept, otherwise it is rejected.
Table 3.1 shows important optimization parameters, the optimization mode and their constraints.
During the optimization process the whole arc is modeled using a series of static source position samples. At the beginning a relatively coarse sampling with only a few control points is used. For each control point the optimal MLC position and MU weight is calculated in some iterations. Afterwards new samples are added to the pool of control points right in between two already existing control points. The MLC positions are iterated at first, MU weights recalculated. This

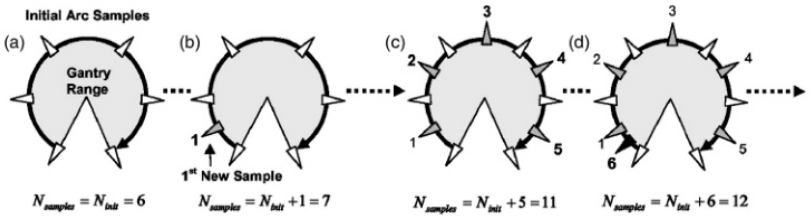

Figure 3.2: Optimization Process of VMAT using progressive sampling. New samples are added, optimization restarts various times [16]

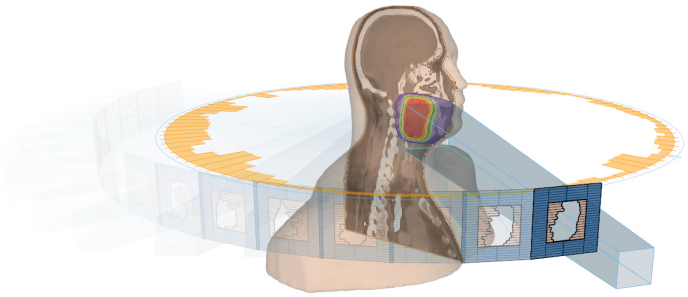

Figure 3.3: Representation of an Optimized VMAT plan using Raystation, RaySearch AB [19]

step is followed again by a number of iterations.
Adding new samples and reoptimizing the whole rotation is repeated until the final number of control points is reached. Figure 3.2 shows the sampling and optimization scheme.
As the optimization process proceeds the number of optimization iterations between the adding of new samples is decreased. This is necessary because of increasing constraints due to restricted leaf motion. The more control points the higher the restriction level for this parameter. On the other hand with more control points the delivery of the arc becomes more accurate.

A representation of a finished optimized VMAT plan is shown in figure 3.3. Using more than one arc may help to achieve a better dose distribution. When selecting the dual arc mode, a second arc is used in opposed direction which otherwise has the same parameters as the first arc. The aperture shapes are split up in order to minimize the necessary movements between two control points. Therefore, they would rather be arranged on one side for the first arc, the other side would be shaped in the second arc.
Multiple arcs are independent arcs which can f.e. have different gantry spacing in between two control points.

As VMAT treatment planning and delivery spreads across radiation therapy facilities, vendors of optimization and dose calculation engines have adapted to the new technique and included it in their algorithms. Medical LinAc vendors have done the same. Nevertheless different machines come with different possibilities.
In the beginning ELEKTA LinAcs were not able to change the gantry speed during an arc. This is not the case for the current machines. Variation of dose rate can be achieved in different ways as well. Some machines allow nearly continuously variable dose rate, offering tiny steps, where other LinAcs only work with stepwise dose rate variation. In combination with varying gantry speed these limitation can be encountered. Another possible mode is to always use maximal dose rate or gantry speed. The gantry only slows down when more dose has to be delivered than achievable with this combination, dose rate drops when less dose exposure is needed. These modes are described in detail in [18].

3.3 Benefits and Drawbacks

VMAT is a relatively new technique therefore no long-term studies are available until now. Nevertheless various publications of VMAT planning studies and clinical outcomes in short-terms for different tumor sites are available. [17] and [2] provide a good overview of currently finished studies of VMAT. Additionally many publications deal with the comparison of VMAT to other treatment modalities.

VMAT is a preferable method in radiation therapy concerning treatment time. IMRT radiation time increases with rising segments and beam directions and can get as high as half an hour for extremely complex cases. VMAT is typically carried out by rotating one or two arcs in one to three minutes each. This saved time can be used for image guidance or other corrections. Additionally more patients can be treated in the same time. A comparison done by K. Otto [16] showed treatment time of a nasopharynx case of 1.8 minutes for a VMAT plan in comparison to the IMRT plan which had a delivery time of 7.1 minutes.
Most planning studies have compared VMAT to CRT or IMRT. It is clear that using VMAT dose conformity, OAR sparing and dose escalation to the PTV increases compared to CRT. The difference between VMAT and IMRT is not that clear. Different studies have shown different outcome, most of them achieved similar or better results. [17]
The total number of MU decreases using VMAT in comparison to CRT. Nevertheless, the volume which is irradiated with low dose increases using VMAT. These small doses may be the source of secondary malignancies.
Finally, VMAT planning is more complex than plan set-up for an IMRT plan. The optimization process for a VMAT plan therefore takes more time than for a regular IMRT plan.

Comparisons of dose distributions are shown in figure 3.4 and 3.5.

VMAT definitely has its place in the treatment of many tumors but can not be used as the universal solution to all entities. It has its advantages but comes with disadvantages. Therefore every case has to be evaluated individually and the appropriate treatment technique has to be chosen to get the best results.

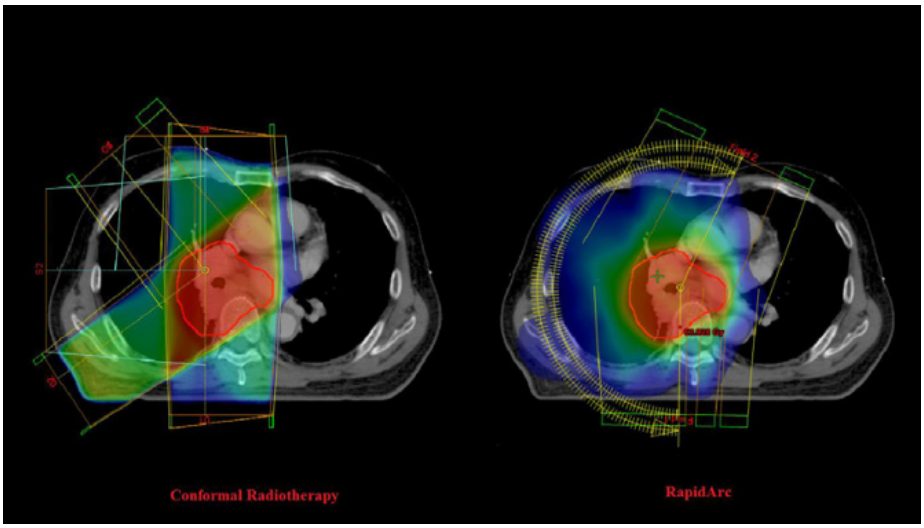

Figure 3.4: Comparison of a CRT plan to a VMAT plan [20]

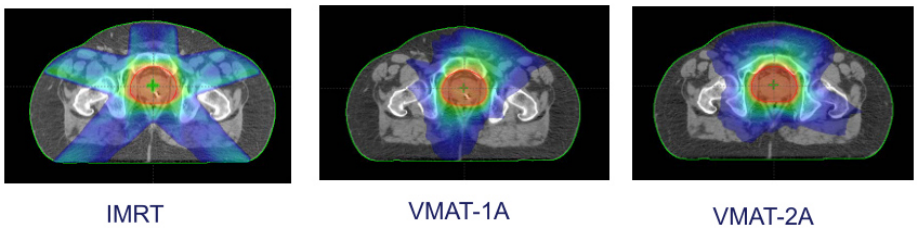

Figure 3.5: Comparison of an IMRT plan to single and double arc VMAT plan [21]

Karl Otto [16] started with a planning study of a nasopharynx case, up until now basically every tumor entity has been the subject of many planning studies. A good overview was given by Teoh et al [17]. Time will give rise to more experience using these techniques and creating guidelines for ideal VMAT optimization. Clinical long-term studies still have to be carried out and evaluated to examine the influence of the large low dose volumes.
In contradiction to what was proposed in the beginning, using VMAT as a single arc technique, experience showed that some cases need more than one arc to achieve the desired dose distribution. Additionally VMAT should be preferable in cases where the arrangement of PTV and OARs is complex, because of its greater possibility to achieve more conformal dose distribution in complex cases. Especially these situations may have the need for more than one arc.

3.4 Dosimetry for VMAT

Starting with a new radiation therapy method but also for regular quality assurance procedures tests or real treatment plans have to be measured and verified on the LinAc without a patient.
A phantom can be used to simulate absorption of a patient or measurements are done directly without any absorbing material. Simple phantoms can be shaped in regular geometric figures like discs or balls and are made of water equivalent material. The most sophisticated phantoms are shaped in a human like form and have density differences. They provide spots for the insertion of detectors. Detector arrangements in phantoms can be found in various sizes and forms. Next to point measurements the most simple version is an arrangement of detectors in a two dimensional static array. These arrays have a significant disadvantage concerning VMAT measurements due to their directional dependence. An advance was done by synchronizing the orientation of the array to the gantry motion. Another approach to avoid angular dependence was to use three dimensional arrangements of detectors. Currently available forms are an arrangement in X-form or a cylindrical arrangement.
Currently used detector types shall be discussed briefly.

Film Dosimetry
Using films for dosimetric measurements is a two dimensional measurement method. Films are the superior method to get a high spatial resolution in dose measurements but can only measure cumulative exposure. Film dosimeters are characterized by a wide dynamic range.
They consist of a photo-emulsion with silver atoms. Incident radiation can interact with the emulsion and increase the optical density of the film by dissolving of silver atoms, the film is 'blackened'. After the exposure the film has to be developed to get quantitative results from the measurement [11]. Different scanners and software solutions are available to get an absolute dosimetric result. No time resolved measurements can be done with this type of detector.

Diodes
Diodes are an example of solid state detectors. The major part of these detectors are made of semiconductors, other materials like diamond, are rarely used. In semiconductors a certain amount of energy is needed to allow conductibility. This energy can be achieved with thermal activation, with doping of the material but also with incident radiation. Mostly used materials are silicon or germanium. Radiation passing through a semiconductor material can cause either lattice excitation, ionization or atomic displacement [12]. For radiation detectors the first two processes are of main interest. Lattice vibration can lead to thermal effects and therefore conductibility. Direct ionization produces an electron-hole pair. For both cases a certain current can be measured when using a bias voltage. This current can be related to the incident radiation.
A picture of a diode detector from PTW is shown in figure 3.6.

Ionization Chambers
Ionization chambers are widely used due to their easy handling, good efficiency, simple construction and applicability for all radiation types. Despite these advantages they show temperature and pressure dependencies and therefore re-

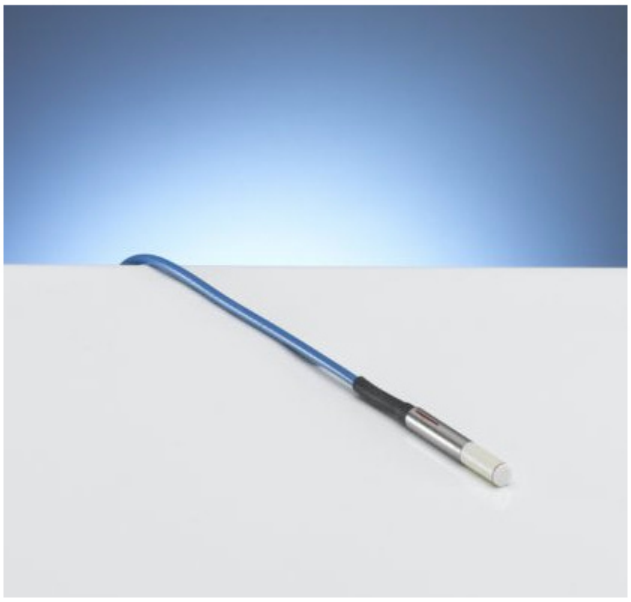

Figure 3.6: Diode Detector, PTW [15]

Figure 3.7: Ionization Chamber, PTW [15]

quire corrections.
They consist of two electrodes which enclose a gas-filled volume (filling the volume with liquid is another possibility but shall not be discussed here). Radiation which passes through the gas can ionize the molecules or atoms. The produced charge pairs then result in a current proportional to the radiation energy which can be measured at the electrodes [11].
Ions or electrons which were produced from the incident radiation are called primary charges. Depending on the biased voltage at the electrodes regions of interaction principles of these charges can be distinguished. Low voltage results in a high recombination rate of the charges. Ionization chambers work in the ion chamber region, were all primary charges are measured at the electrodes but no further charges are produced. Increasing the bias voltage results in the production of secondary charges due to traveling primary charges. This region is called the proportional region [12].
A picture of an ionization chamber from PTW is shown in figure 3.7.

Electronic Portal Imaging Device EPID
Electronic portal imaging devices are attributed to solid state detectors. They consist of different layers to get exact measurements of dose. They are arranged in a matrix array with a certain number of pixels depending on the detector. These arrays can be mounted on the LinAc, some machines provide an EPID by default to enable imaging with the therapy beam.
Build-up and signal processing shall be discussed in the next chapter.

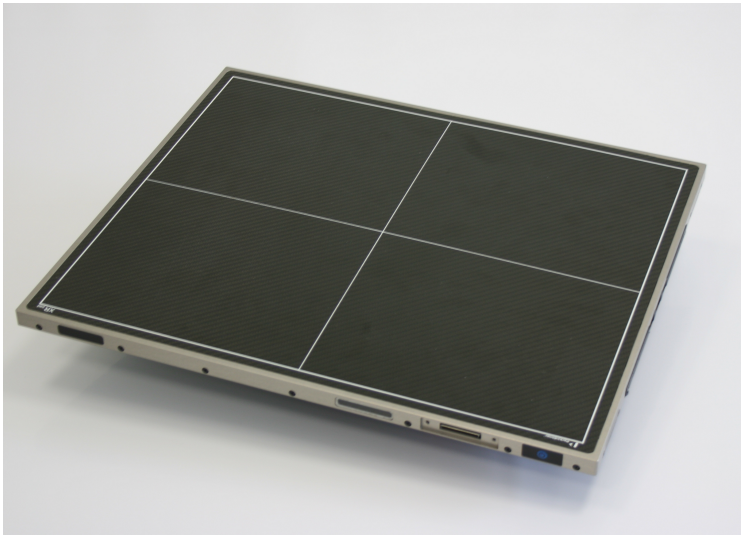

Figure 4.1: Flat-Panel detector, Perkin Elmer, http://www.perkinelmer.com/

4 Flat Panel

Flat Panel refers to a certain kind of detector used in radiotherapy for captioning of so called portal images. Portal images originate from the therapy X-ray beam itself. They have various practical applications including daily checking of correct patient positioning as well as tumor size and location. Images can be taken before the treatment itself, where they are referred to as localization images, and during treatment, where they are called verification images [23].
Previously these images have been gathered using X-ray films. The main disadvantage of film dosimetry is the necessary procession step which is obligatory to get the information. This development needs some time during which the patient can move and the image does not represent the actual patient position. In contradistinction to films, flat panels use an active matrix-scanning technology which assigns them into the group of electronic portal imaging devices. Apart from semiconductors which are used in flat panels, liquid filled ionization chambers can be used as well.
The EPID is mounted on the gantry in a cassette enclosure and rotates in accordance with the treatment head. Therefore the relative position of the EPID to the treatment head does not vary. Despite their advantages EPIDs only provide images of poor quality due to the predominant Compton Effect. Distinctive structures like bones are necessary for position verification.
Figure 4.1 represents a panel produced by Perkin Elmer without enclosure.

4.1 Buildup of an a:Si-H flat panel

Flat panels, more precisely active matrix flat-panel imagers (AMFPI), consist of several layers which convert the therapy X-ray beam to an electric signal. For deeper understanding of the conversion process as well as the consequential errors and necessary corrections, the build-up of a flat panel shall be described

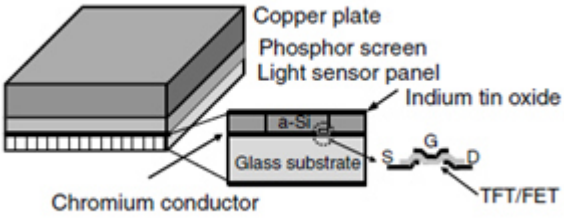

Figure 4.2: Schematic draw of an a-Si:H solid state detector with all basic components: copper plate, scintillator, light sensor panel with silicon diodes [22]

shortly. Figure 4.2 shows a schematic illustration of the essential components.

4.1.1 Copper Plate

The most superficial part following the enclosure of the panel itself is a copper plate. This layer normally is about 1.5mm in thickness and serves as an X-ray converter.
Incident radiation is converted into electrons. The interaction process is dominated by Compton interactions at therapy energies, which is highly dependent on electron density, in contrast to the photoelectric effect which strongly depends on the atomic number and is used in diagnostic imaging [23]. As anatomical structures do not vary much in electron density the achieved contrast is not optimal.

4.1.2 Scintillator

The second layer is a scintillator. It is made out of phosphor material including gadolinium oxysulphide.
A scintillator converts incident ionizing radiation into light photons. They are normally used for detection of photons or fundamental particles. Scintillators can both be anorganic or organic. The first group mainly consists of crystals where incident electrons produce electron-hole pairs and coincidental relaxation processes produce photons with a material dependent energy [10].
The scintillator has to be transparent for the produced light in order to allow transmission to the following structure.

4.1.3 Photo-diode

Underneath the scintillator a large area, pixelated array follows. Each pixel in the array consists of a thin film transistor (TFT) build on a glass substrate. The TFTs are fabricated from hydrogenated amorphous silicon (a-Si:H). Silicon itself is a semiconductor which can be made conductive when energy is transferred to the material.
In flat panels these energy originates from the photons produced in the scintillator. Each incident photon results in the creation of an electron-hole pair and

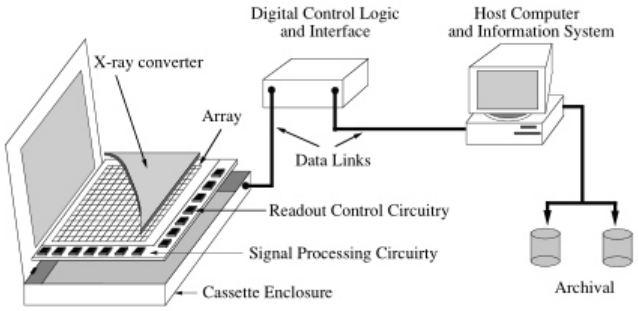

Figure 4.3: Schematic illustration of the elements of an active matrix, flat-panel imager (AMFPI) [23]

an electric impulse. One photo-diode is located in each pixel. The signals are stored for a short time in the TFT and read out pixel-wise. [23]

The signal is measured by electronics connected to a computer. A software is necessary to correct the original signal. If the image is only intended to be used for position verification, simple correction algorithms are sufficient. More sophisticated software and corrections are necessary when absolute dose measurements shall be done.

Figure 4.3 shows a complete draw of the panel with all other necessary components.

4.2 Software - Flat Panel Plug-In (FPPI)

The flat panel plug-in was developed to convert the original signal from the flat panel to an image for absolute dose measurements. It was developed at the institute on reasearch and developement on advanced radiation technology (radART) at the Paracelsus Medical University (PMU) in Salzburg.
Although designed as a detector for mega voltage radiation the panels receive damage which especially affects the electronics. These damages can partly be corrected for in the course of signal processing and therefore the panel can be in use for a longer period. The plug-in includes not only correction algorithms to cope with aging effects but deals with other necessary corrections as well.
Apart from the application of various correction algorithms the plug-in provides live view of the images which are currently measured and storage of the latter.
During the time where this project was carried out, some corrections were finished and included into the plug-in as well as new calibrations had been done. These changes and the resulting improvements will be discussed in the analysis of this project and show how important the correction algorithms are.

Some of the available correction algorithms will be described here although not all of them are finished yet.

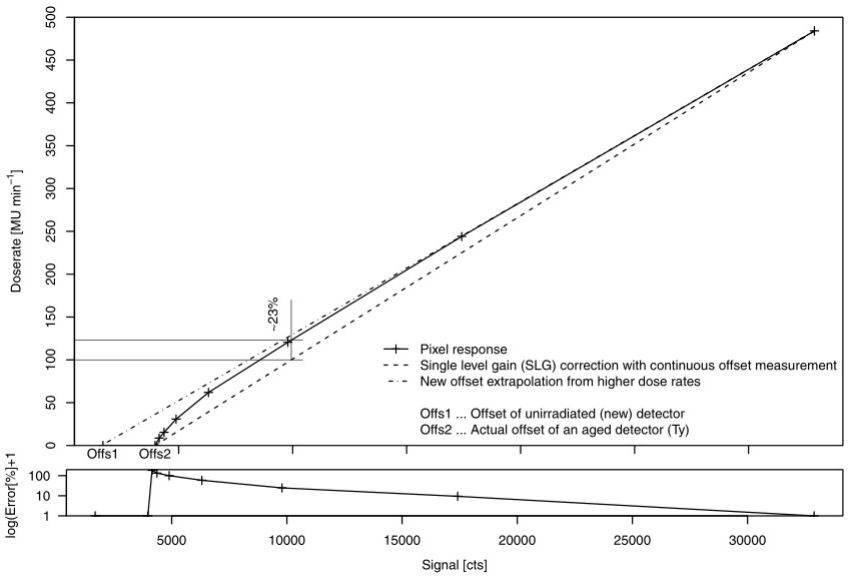

Figure 4.4: Dose rate response of one pixel for the old panel, showing large residual errors when only SLG is applied [25]

4.2.1 Non-Linear Response - Multi Level Gain Correction

Each pixel of the detector shows a different response depending on the dose it is exposed to. This response also varies with the cumulative dose the pixel has received over its live time. Pixels tend to show a higher dose with increasing dose exposure. Therefore, especially for aging detectors, a pixel specific correction is necessary.
The simple approach is to use an offset and gain calibration which would result in a linear curve. This approach is called single level gain (SLG) correction. But measurements have shown that especially for low doses and dose rates the behavior of the response function of the panel is not linear and shows large deviations from the high dose regions.
Therefore a multi level gain (MLG) correction has been implemented which not only uses two points to calculate offset and gain but takes various sampling points into account. In between these measured points the curve is interpolated. Details regarding this behavior can be found in [25].
An example for such a multi level gain correction curve is shown in figure 4.4.

4.2.2 Temperature Correction

Temperature effects can be separated into two groups.
During the course of a day many images are taken with the panel, the panel gets warmer with each irradiation. Changes in temperature result in different signals for the same dose and pixel. With increasing temperature the pixel shows a much higher value.
Investigations showed that there is not only a difference in the offset value of

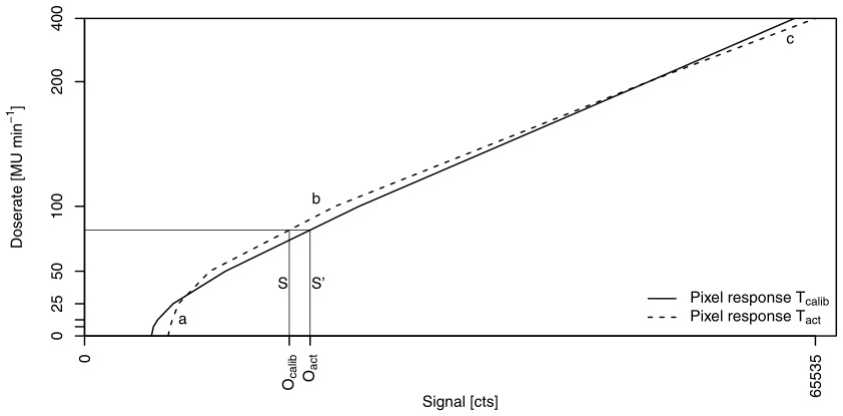

Figure 4.5: Schematic illustration of first level temperature correction [25]

the correction curves, but also gain changes with alternating temperatures.
The first level temperature correction mainly deals with offset changes and is shown in figure 4.5. Parameters a, b and c are used to relate the offset at the calibrated temperature T_{calib} to the offset at the actual temperature T_{act} which gives an actual signal S' depending on the temperature [25].
As this correction is not sufficient, a second level temperature correction has been introduced which deals with the residual error to achieve a satisfactory fit to the actual pixel response behavior. These residual errors show as stripe artifacts in the first level temperature corrected picture. An interpolation of the MLG calibration curves for the different temperatures is done to annihilate these artifacts [25].

4.2.3 Ghosting

Ghosting is the effect of exponential decay of the signal measured by the detector. After the beam has been turned off the signal does not fade off instantly but shows a so called "ghost".
This effect can be explained by two physical properties of the detector. On one hand charges are trapped in the thin film transistor and on the other the scintillator shows a postglowing effect [24]. These two effects result in the necessity of image correction regarding the exponential decay of the signal.
Irradiating the detector and frame wise capturing of the images afterwards provides one means of measuring the ghost and calculating the necessary corrections. Figure 4.6 shows the exponential decrease of the signal after irradiation of the panel has stopped.

4.2.4 Sync-Artifacts

The flat panel can be used to capture single frames or a series of images. Recording of various images is referred to as continuous free-running mode. Especially for VMAT verification many frames have to be recorded in order to investigate all necessary parameters.

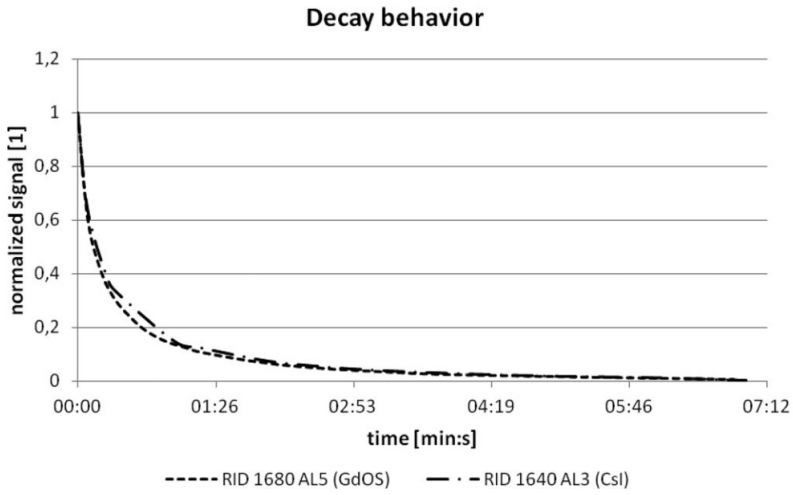

Figure 4.6: Exponential decay curves of detector ghosting in comparison of two different scintillator materials [24]

Simultaneous read out and irradiation of the panel leads to synchronization (sync) artifacts which show as moving stripes from frame to frame due to interaction of these processes. These alternating moving black and white stripes are of constant width and intensity [24].
Sync-artifacts can be characterized and can be annihilated by application of a correction algorithm. This correction algorithm was included in the flat panel plug-in and can be found in detail in [24]. Figure 4.7 shows sync artifacts for a flood field and an image of a scull and the same images after the correction has been applied.

4.2.5 Bad Pixels

Radiation damages also include complete failure of certain pixels. This may result in corrupt pixels which show false values. Irradiating the panel with a flood field these pixels can easily be discovered.
Two approaches are included. The first locates bad pixels using local regions around each pixel, the other one compares pixel values in the whole subpanel region. If the value deviation exceeds a certain level, the pixel is marked as bad pixel, the actual value is overwritten by a mean value from surrounding pixels.

4.3 Application of EPIDs

EPIDs have been the preferred tool for verification of patient positioning in the last decades. Tumor movements between or during the delivery of a fraction can be examined as well. Since the images produced by them also contain dose information, special interest and investigations have been done in this area as well.
EPIDs can be used in transmission or non-transmission mode dependent on

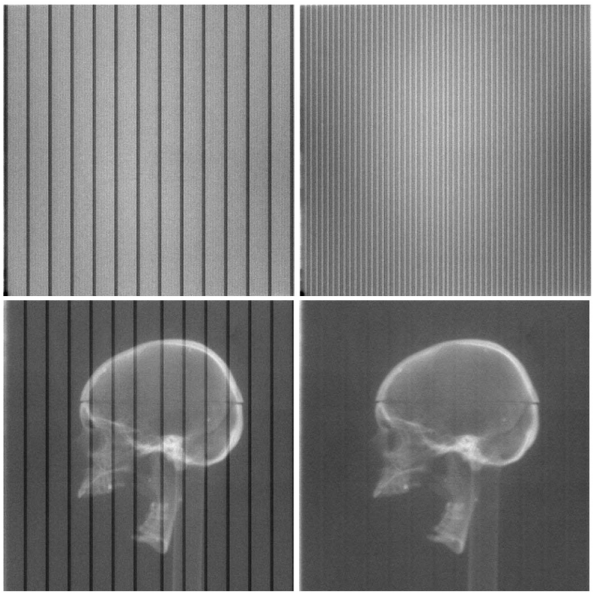

Figure 4.7: Single frames of a flood field with different dose rates; Image of a Scull phantom before and after sync-artifact correction [24]

whether a phantom or patient is positioned in between the treatment head and the EPID.
Non-transmission mode is mainly used for checks of geometric characteristics. Test fields are created to check field flatness or beam symmetry as well as MLC leaf positioning. Most of these applications do not include dosimetric conversion of the gray-scale image [26]. Nevertheless these images can be converted to dose and provide the user with enough information for dosimetric checks. Additionally, MLC leaf positioning can be checked for dynamic delivery with non-transmission measurements. Using the continuously free-running mode every frame of the EPID is recorded and allows for complete checks for VMAT application. Including a CT data set, dose distributions can even be reconstructed inside the patient.
Using transmission mode allows for verification of the correct delivery of dose to the patient, starting from point-dose verification up to 3D reconstruction [38].

It is obvious that EPIDs allow for a wide range of applications and that investigations and research are far from complete.

5 Quality Assurance on LinAcs

Linear accelerators which are used in medical environment and therefore specified as medical LinAcs, are subjected to obligatory quality checks. These checks are specific for the medical use and have to be documented by the institution which uses the machine.
Depending on the potentialities the medical LinAc has, different checks have to be performed. Potentialities refer to mechanical or software characteristics of the machine like the availability of MLCs or the application of certain radiation therapy techniques.
Vendors tend to provide lists of recommendations for checks and their frequency as well.
The conditions for checks to be undertaken are set up by national standards bodies and can be found in various ÖNORM papers. Nevertheless these are often built up on recommendations of international commissions. One of these commissions is the IEC, the international electrotechnical commission. Other examples include the AAPM, the American Association of Physicists in Medicine which regularly publishes task group reports with the help of their world wide members. One task group report which deals in detail with medical LinAc QA is Task Group Report # 142 [39].
In [40] the IEC gives recommendations regarding routine test in medical imaging departments. National regulations take this and other norms into account and create a national norm, for example [41], which deals with medical electron accelerators and their functional performance characteristics.

Regarding these guidelines and recommendations it is obvious that the clinical implementation of new radiation therapy technique like VMAT involves preclinical testings.
The medical LinAc used in this project was an ELEKTA Synergy machine with an Agility head providing the user with 80 MLC pairs. The vendor, ELEKTA, provides a preclinical test and calibration method for VMAT before it should be used clinically. This test was performed with the help of a technician from ELEKTA. It consists of a radiation plan irradiated on the machine. If the process runs smoothly, the machine should be ready for VMAT, otherwise additional calibration is necessary.
Additional testing was done before as well as after the ELEKTA calibration procedure to observe the resulting impact.

6 Preclinical Tests

While VMAT spreads over the clinics various publications for VMAT commissioning and acceptance tests arise and guidelines are formed by national and international institutions. Two publications which appear frequently were written by Ling et al. [28] who was working with Rapid Arc, Varian Medical Systems, and Bedford and Warrington [27] who suggested guidelines specifically for Elekta accelerators. The presented methods are widely used and adapted to the current clinical situation in different institutions.
To make the right decision on which tests have to be performed for commissioning of VMAT it is essential to define the initial position. Parameters which have to be tested are identified and already implemented characteristics can be left out. Additionally the tests have to be chosen to fit for the applied measurement tools and detectors. Detectors which are in current use may be reliable, new detectors have to be tested themselves.

This project was done on one medical linear accelerator at the institute of radiotherapy and radio-oncology at the federal hospital in Salzburg (SALK). The machine is an Elekta Synergy accelerator with an agility head including 80 MLC leaf pairs, each of 0.5cm width, forming a maximum total field size of 40x40cm^2. As detector the EPID mounted on the LinAc was used which has an active area of 40x40cm^2 containing 1024x1024 pixels. Due to the greater distance the panel has to the treatment head compared to the isocenter it only allows for maximum field size of 26x26cm^2 despite its size being equal to the maximum field size in the isocenter. Therefore the primary collimator allow for 26x26cm^2 field size while 52 MLC pairs shape the field individually. Signals were measured with the flat panel in combination with signal processing using the FPPI which provided corrected pictures with gray values in 16 bit unsigned form. Conversion factors allow for direct calculation of absolute dose out of these gray value matrices. The in-house developed software open-radART serves as forward planning and record and verify tool.
IMRT with static leaves was already implemented as well as basic field parameters like uniformity or stability of the beam for all gantry angles checked. The detector has been investigated thoroughly in course of the implementation of the FPPI. Therefore these tests were skipped.
Performed tests had to cover all parameters which are new for VMAT application in comparison to sMLC IMRT. These include varying dose rate, moving leaves with different velocities and directions during beam delivery and varying gantry speed. Tests have been chosen to base on one another. Where the first tests start with simple checks of single parameters they get more sophisticated to the end.
These tests shall be described in detail, analysis is done in the next chapter.
Most tests cover the whole field the panel can be irradiated with. All tests have been done in clockwise and counter-clockwise gantry rotation direction to observe possible differences. Tests with constant gantry speed were done repeatedly with varying over-all dose output which resulted in different gantry speeds to catch variations depending on this parameter. All test plans have been created in forward planning mode which means manually definition of every MLC at every control point, control point set-up including gantry angles, dose rates and MU delivery.

The LinAc which was tested for VMAT provided only step-wise dose rate variation, for 6MV photon energy the limit for lowest dose rate during rotation was 28 MU/min, therefore providing the user with the following dose rates: 28MU/min, 57MU/min, 115MU/min, 230MU/min, 460MU/min.

6.1 Test Plan Setup

The test plans were set up using the in-house developed software open-radART. As these plans are not optimized in accordance with a certain structure but should follow a special pattern designed by the planner, they were created in forward planning mode. The concept of plan set-up using this software shall be described briefly.

Figure 6.1 shows the graphical user interface of open-radART. The right side can show either patient overview (Pat), the CT image series (Ser), the plan where dose calculation is fused with the CT image series (Pln) or the radiation field (Fld). In this case the field is shown and the MLC positions of one control point are visible.
The left side shows various details (see figure 6.2). Starting with the patient name at the top of the plan, treatment, field and segments follow.
A plan has to be created and named, followed by the treatment and the field arrangement.
Parameters of the whole field, which would symbolize one arc in VMAT mode, can be altered underneath. Machine, radiation quality and beam energy have to be chosen, the DL (MU/min) is not important for VMAT because this parameter is overwritten by another entry, but as a minimum 7 has to be entered. The following parameters characterize the gantry start angle, couch rotation and focus surface distance, on the right the isocenter position is defined. Collimator rotation and absolute field size can also be entered. The maximum allowed field size for measurements with the panel is 26x26cm^2. Here the field was automatically decreased in its width concerning the variable y, because these are the maximum MLC positions.
Absolute dose output has to be defined.
Essential information which characterize the VMAT treatment can be found in the segment section and have to be manually altered in forward planning mode. Each segment symbolizes one control point, starting position is defined by the first segment. For every MLC segment the positions of the MLCs can be altered (x, y [cm]). Below, the gantry angle of the control point is defined using the difference to the gantry start angle. The absolute angle can be calculated by adding the first entry of gantry to the start angle. The second entry in the gantry field is the covered angle of the segment. These entries are followed by the definition of the dose rate for this segment. At the top of the segment section, the entry "Gewicht" is the cumulative weight of the segment. To get the MUs which are irradiated in the segment, the weight of the previous segment has to be subtracted from this weight and multiplied by the absolute dose output. Therefore it gets clear that this value has to start at 0 for the first segment and reach 1 at the end of the control point sequence. Other final values can be chosen, but this way is the most intuitive one.

Parameter	Limit
Gantry Speed	max. 6 deg/s
Leaf Speed	max. 3.5 cm/s
Jaw Speed	max. 9 cm/s
Gantry MU delivery	max. 20 MU/deg
Gantry MU delivery	min. 0.1 MU/deg
MLC leaf MU delivery	min. 0.3 MU/cm

Table 6.1: Machine Parameter Restrictions

Nevertheless some additional parameters have to kept in mind which are not checked by open-radART but violation of these results in the incapability of the LinAc to irradiate this plan. These parameters are summarized in table 6.1. They have their origin in technical limitations of the machine but also in limits of the irradiation capabilities of the LinAc. Violation of these restrictions results in radiation with bad quality, instability or inaccuracy. The medical LinAc would decline to execute plans which do not stick to these limits.
Gantry speed, leaf speed and jaw speed are technical limitations. The maximum and minimum gantry MU delivery as well as the MLC leaf MU delivery result out of accuracy limitations. Too fast rotation of the gantry with practically no output is not clinically useful, MU output above a certain level from one specific direction would annul the basic idea of a VMAT plan. On the other hand if the MLC leaves move too fast while only little output occurs the distribution of the dose in this area would have a high level of imprecision.
Therefore these restrictions are specified for each machine in the optimizing treatment planning system. If a VMAT plan is created they are automatically kept by the planning system, no errors on the machine itself can arise if they are correctly entered beforehand. Here, they had to be kept in mind due to the forward planning mode.

All test plans have been set up according to the restrictions. Each control point was defined as a MLC segment, the parameters of MLC position, cumulative weight, gantry start position and covered angle as well as the dose rate for each segment have been entered. Gantry speed and MLC leaf speed was automatically calculated by the system but are no visible values. The dose rate definition is valid from the start of the segment till the start of the next one where a new dose rate is defined. MLC positions are interpolated linearly.

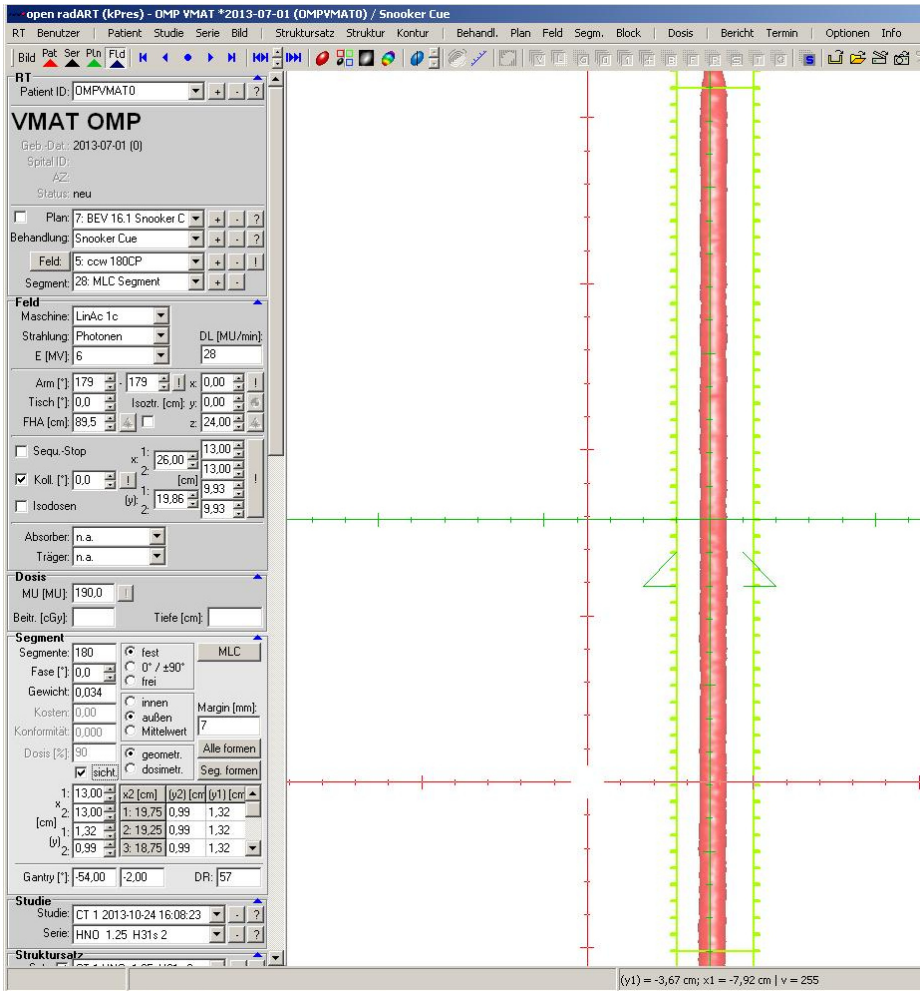

Figure 6.1: Screenshot of the Software open-radART

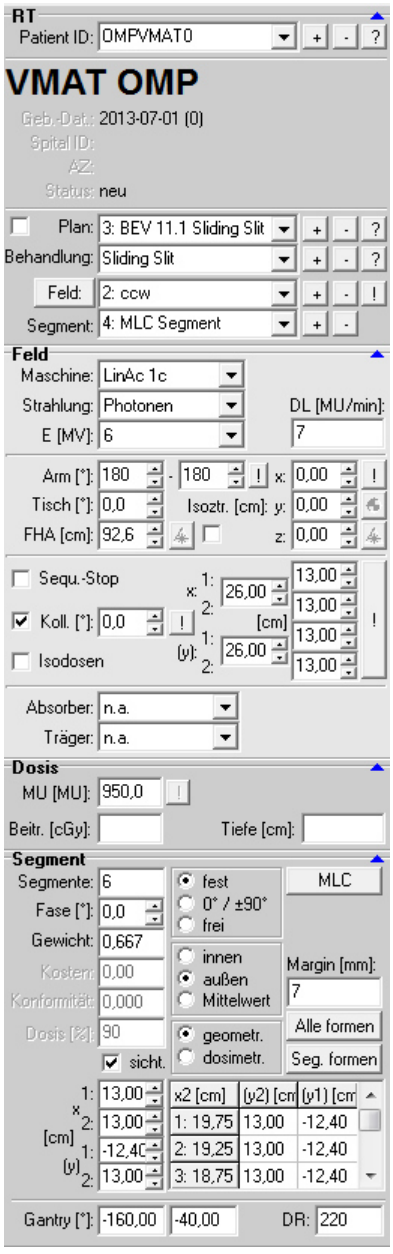

Figure 6.2: Patient information of VMAT Test Patient in open-radART

Segment No.	Start (deg)	$\triangle\alpha$ (deg)	Dose Rate (MU/min)	Gantry Speed (deg/s)	MU Output
1	180	100	50	0.94	101.25
2	80	20	28	0.94	14.85
3	60	50	115	0.94	101.25
4	10	20	28	0.94	14.85
5	350	25	230	0.94	101.25
6	325	20	28	0.94	14.85
7	305	12.5	460	0.94	101.25

Table 6.2: Technical details of the segments used for dose rate testing, counter-clockwise rotation, 450MU total output

6.2 Description of Test Plans

6.2.1 Dose Rate

The first tested parameter was varying dose rate. The test itself was adapted from the Dose Rate Gantry Speed test from Jorgensen et al. [30].
The whole field was separated into four segments, respectively for the four higher usable dose rates. The MLCs formed a static open field 26x6.5cm^2 at the isocenter, therefore irradiating the whole panel width for each segment and moved to the next segment with the lowest possible dose rate before stopping the MLCs again and irradiating the next segment. MLCs moved simultaneously and with the same speed between the segments. Calculations were done to equally irradiate each segment, disregarding dose distributions during the movement of the MLCs with the lowest dose rate. The MU output can be calculated combining dose rate, gantry speed and covered angle of one segment.

$$MU = DR \cdot \frac{\alpha}{GS} \tag{6.1}$$

where MU is the MU output of the LinAc for one segment, alpha the rotation angle during the segment and GS the gantry speed. Table 6.2 shows the characteristics of all segments including these where the MLCs move from one segment to the next, figure 6.3 represents an image of all segment shapes from open-radART.
The gantry covered 247.5 degrees, over-all output was varied from 90 to 450 MU to achieve gantry speed in a range from approximately 1 to 6 deg per second.

This test shows the control of the dose rate and corresponding time calculation during which each segment is irradiated. Ideally every segment should show the same dose on the detector but due to the movements from one segment to the next one with non-zero MU output some variations especially at the borders of the taken image are to be expected.

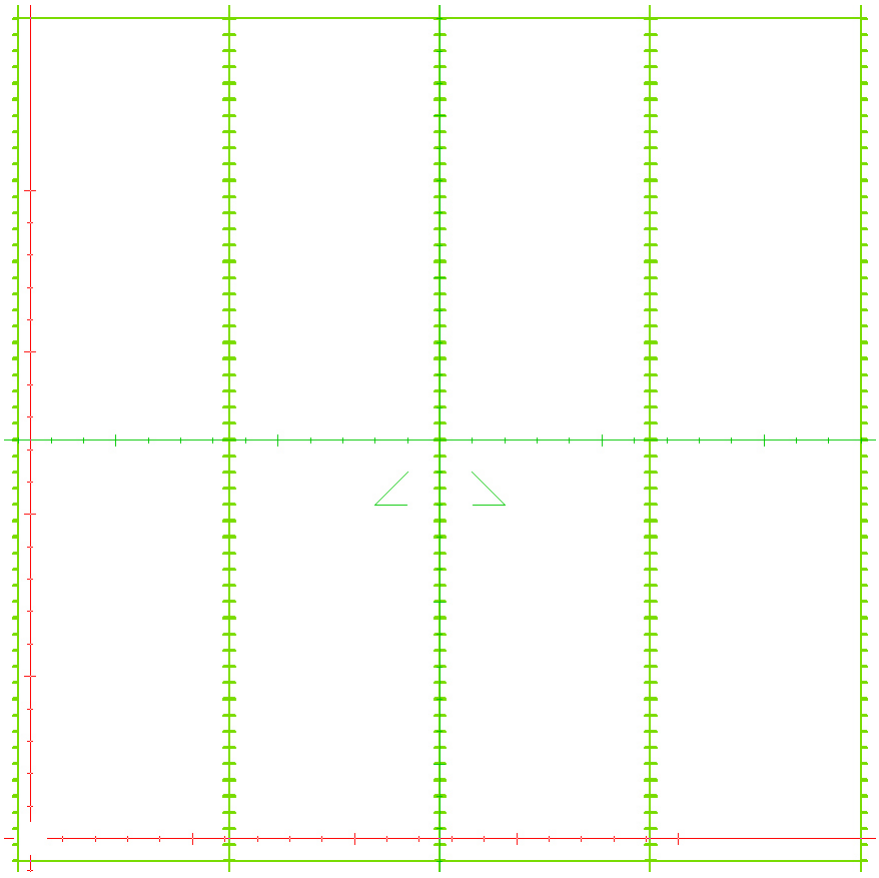

Figure 6.3: Dose Rate Test, Field View in open-radART; green lines represent MLC positions at control point, all control points shown

Segment	Start (deg)	$\triangle\alpha$ (deg)	Doserate (MU/min)	MLC leaf Speed(cm/s)	Gantry Speed (deg/s)	MU Output
1	181	24	460	0.8	2.94	62.5
2	205	48	230	0.4	2.94	62.5
3	253	92	115	0.2	2.94	62.5
4	345	195	57	0.1	2.94	62.5

Table 6.3: Technical details of the segments used for DRMLC test, clockwise rotation, 250MU total output

6.2.2 Dose Rate versus MLC Leaf Speed

For the dose rate versus MLC leaf speed test the whole panel was again separated into four segments. The MLC leaf speed and the dose rate were varied to achieve a homogeneous dose distribution over the whole detector. As dose rate variation was already checked before the central element of this test was varying leaf speed. The MLCs started all at one side, one leaf bank opened the first segment, the second bank closed the first segment again. Then the same procedure started for the second segment. Each segment had a size of 26x6.5cm^2. There was constant movement of at least one MLC bank.
Gantry speed was kept constant using the same calculation method as for the dose rate test. Depending on the dose rate the MLCs moved with different velocities. Higher dose rate implies higher MLC leaf speed.
This test was taken from Jorgensen et al. [30].

Figure 6.4 shows the schematic control point - MLC position drawing, table 6.3 gives an example of the segments with the chosen characteristics. As over-all MU delivery varied so did the gantry speed and the MLC speeds.

This test covered the whole arc. Variations were done including both gantry rotation directions and variation of total MU output from 150 to 750MU which resulted in gantry speeds from below 1 deg/s to 6 deg/s.
Homogeneous intensities for all segments confirm good interplay of varying dose rate and MLC leaf speed. Comparison of tests with different total MU can show influence of different MLC speed as well as gantry speed.

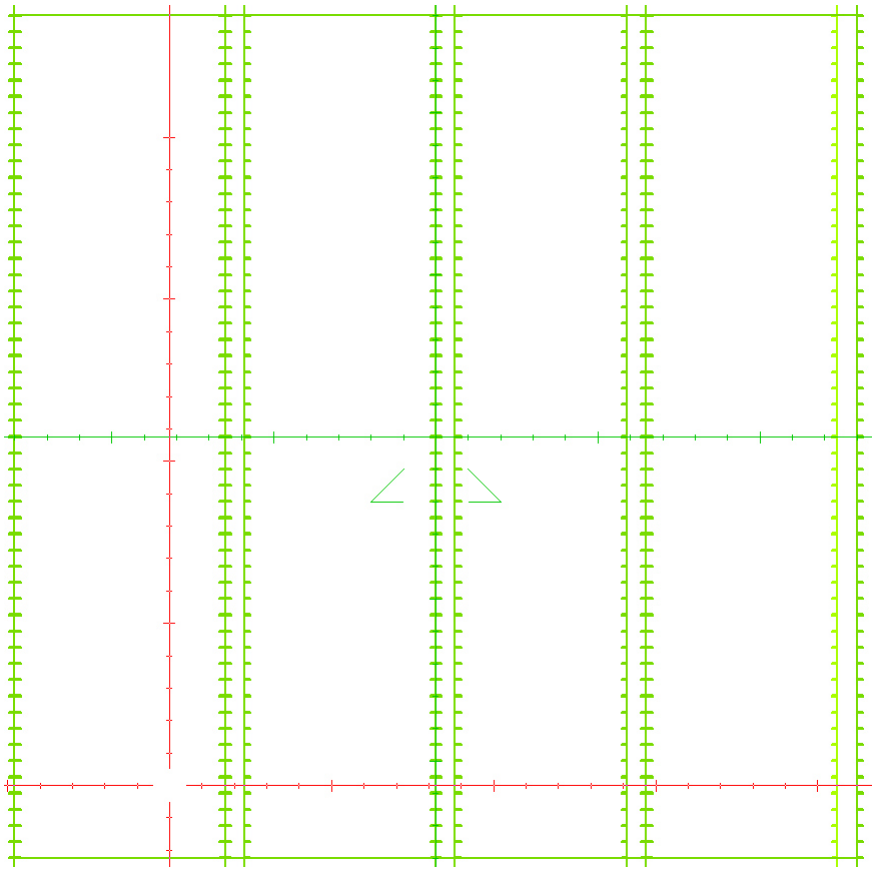

Figure 6.4: Dose Rate versus MLC Leaf Speed Test, Field View in open-radART; green lines represent MLC positions at control point, all control points shown

Segment	Start (deg)	$\triangle\alpha$ (deg)	Doserate (MU/min)	Gantry Speed (deg/s)	MU Output
1	180	10	28	0.8	5.95
2	170	10	460	0.9	79.05
3	160	10	28	0.8	5.95
4	150	10	460	0.9	79.05

Table 6.4: Technical details of the first four segments of the Picket Fence Test, counter-clockwise rotation, 850MU total output

6.2.3 Picket Fence Test

The picket fence test, sometimes also referred to as garden fence test, exists in various forms and is a standard test which is included in nearly every commissioning process. Jorgensen et al. [30], but also many other authors relied on this test; [35], [31], [28] are only examples, this list is far from complete. Chui et al. [36] was the first one to introduce this pattern.
This test consists of two different segments which alternate. The MLCs always have a constant shape. They form a small slit, with the minimum possible tip to tip distance which is allowed by the machine. In this case this distance is 0.6cm. In the first segment the MLCs move from their starting position with a very low dose rate to their next position. The second segment does not include any MLC movements. The dose rate is increased to the highest possible level irradiating a small slit on the detector. Afterwards the MLCs move again to the position of the next stripe.
Collectively ten stripes were irradiated. Figure 6.5 shows the schematic drawing of all MLC positions. The two seemingly stripes at the end and at the beginning do not define a stripe but start and end position. Table 6.4 gives an overview of other important characteristics of this test. Only the first four segments are listed, the other 18 necessary to achieve ten stripes follow likewise. Each stripe is 0.6cm in width, the distance between them is approximately 2.3cm.
Again clockwise and counter-clockwise rotation as well as different total MU output and therefore gantry speed combinations were tested to check for influences of all parameters. The gantry rotated over an angle of 210deg. To cover different gantry speeds from below 1 deg/s up to 6 deg/s total MU output of 170MU to 850MU was chosen.

This test specially focuses on correct MLC positioning. As the MLCs move quite quickly from one position to another and the constant stripes receive a very high intensity, misplacement of only one MLC can be observed even below millimeter ranges. Correct interplay of dose rate change and MLC movements can be observed as well. The MLCs have to stop and start rather abruptly which additionally allows for observation of this circumstance.

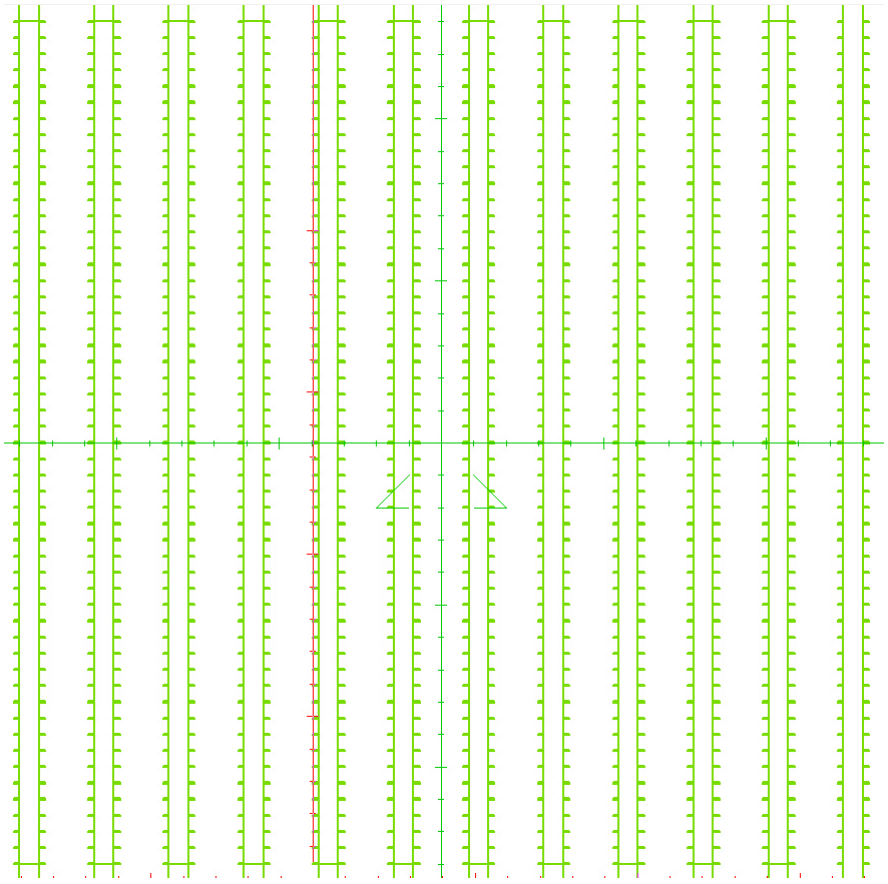

Figure 6.5: Picket Fence Test, Field View in open-radART; green lines represent MLC positions at control point, all control points shown

Segment	Start (deg)	$\triangle\alpha$ (deg)	Doserate (MU/min)	Gantry Speed (deg/s)	MU Output
1	181	50	230	1.9	101.4
2	231	12.5	230	1.8	25.35
3	243.5	62.5	230	1.9	126.75
4	306	41.7	230	1.9	84.5

Table 6.5: Technical details of the dynamic MLC test, clockwise, 338MU total output

6.2.4 Dynamic MLCs

A lot of investigations have been done concerning properties of dynamic multileaf collimator movements. This test focuses on one of the properties which belong to dynamic behavior of MLCs. Thorough investigations concerning these properties have been done by Chui et al. [36] who was using films as dosimetric measurement system, Richart et al. [34] and Rowshanfarzad et al. [31] adapted these tests using EPIDs for verification.
The chosen test separates all MLCs into four groups, 13 MLCs per group. In every group a small slit with 0.6cm in width is built and swept across the field. All MLCs move with a constant speed over the whole field but every group has a different speed. Therefore four vertical stripes, each with homogeneous but different intensity, should arise, representing the different MLC speeds.
Special attention has to be paid to the borders of the groups where interactions between MLCs moving with different speeds can be observed. These effects should be minimal but can show friction or motor failures of a certain MLC.

Figure 6.6 shows the schematic drawing of the test, table 6.5 lists all important characteristics.

This test was done in both clockwise and counter-clockwise gantry rotation direction as well as total MU output variation from 135MU to 675MU resulting in different gantry speeds from below 1 deg/s up to 6 deg/s. The test covered a gantry angle of 166.7 deg. Four control points apart from the definition of the starting position were enough to define all movements.

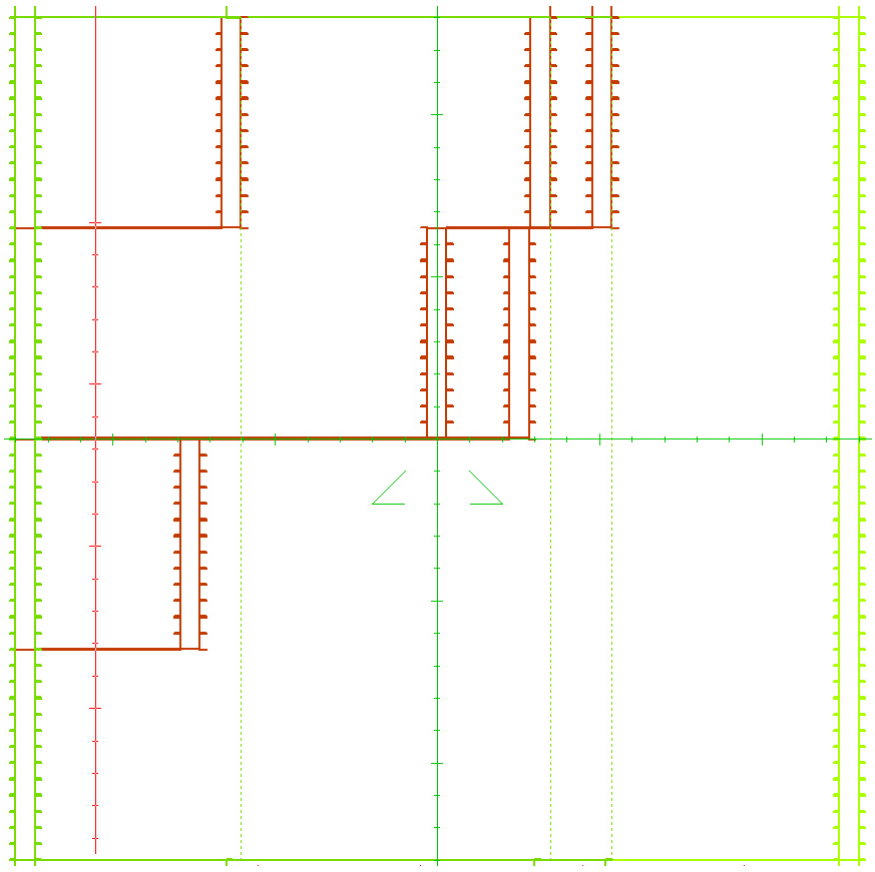

Figure 6.6: Dynamic MLC Test, Field View in open-radART; green and red lines represent MLC positions at control point, all control points shown

Segment	Start (deg)	$\triangle\alpha$ (deg)	Dose Rate (MU/min)	Gantry Speed (deg/s)	Leaf Speed (cm/s)	MU Output
1	180	40	230	4.8	1.5	31.67
2	140	40	230	4.8	1.5	31.67
3	100	80	230	4.8	1.5	63.34
4	20	40	230	4.8	1.5	31.67
5	340	40	230	4.8	1.5	31.67

Table 6.6: Technical details of the sliding slit test, counter-clockwise, 190MU total output

6.2.5 Sliding Slit

The sliding slit test is again a test which deals with dynamic behavior of the MLCs. A sweeping slit test pattern was proposed by LoSasso et al. [37] who performed measurements using an ionization chamber, and adapted by Richart et al. [34] for EPID dosimetry.
Keeping the principles of these test based on the above publications the pattern was adapted and used in this project.
Using the MLCs a slit with minimum width of 0.6cm was formed. The dose rate and gantry speed stayed constant while the slit was moved across the panel. The speed of the MLCs stayed constant as well. The slit moved from the right side to the middle of the detector, turned around again and returned to its initial position, then swept across the whole field, reversing again to the middle of the panel and finally moved to the left end of the EPID.
As the dose rate and MLC speed do not vary the total dose over the whole detector should be homogeneous. Errors of over or under-travel of leaves or leaf banks can be observed with this test as well as non-uniform travel of the MLCs.

Figure 6.7 shows the schematic draw of the test, table 6.6 lists the important values. In the third segment the slit moves from one side of the panel to the other, therefore the covered angle as well as the MU output are twice as high as in the other segments to keep the remaining values constant.

This test was done clockwise and counter-clockwise with MU output ranging from 190MU to 950MU to cover gantry speeds from below 1 deg/s up to approximately 5 deg/s. The total covered gantry angle was 240 deg.
Homogeneous distribution of the dose shows the right behavior of MLC start, stop and reverse movement directions which display the extreme conditions of MLC speed changes.

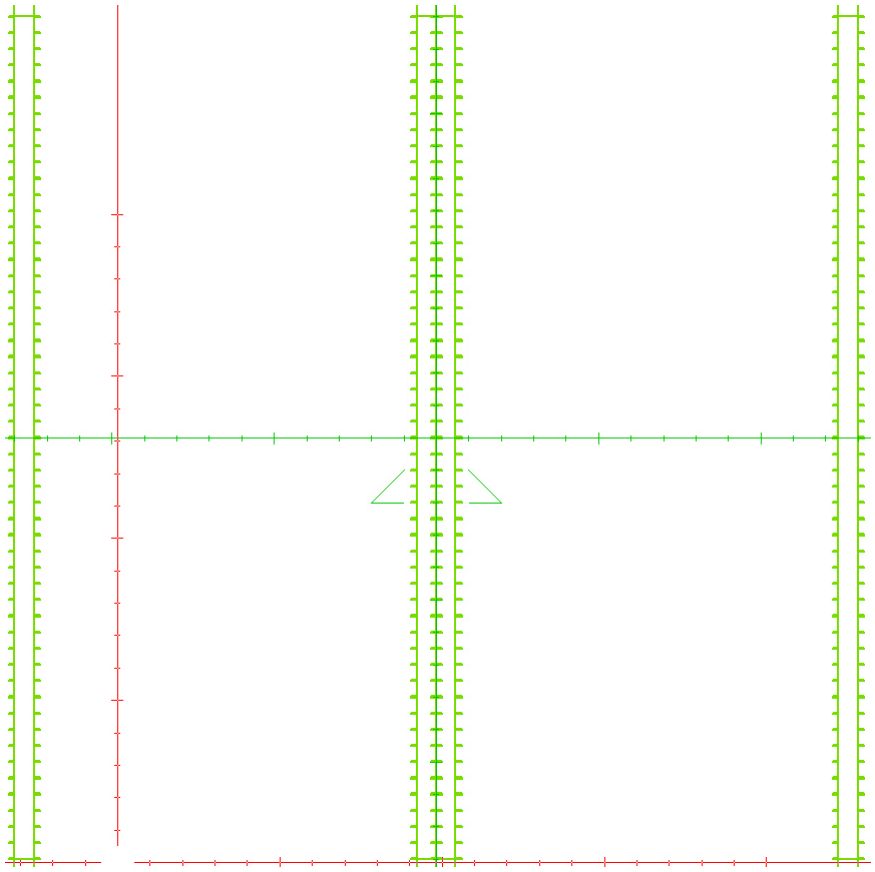

Figure 6.7: Sliding Slit Test, Field View in open-radART; green lines represent MLC positions at control point, all control points shown

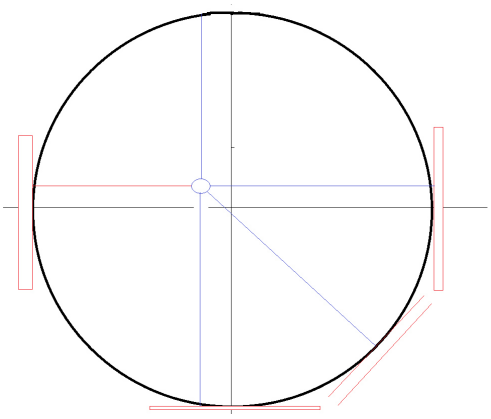

Figure 6.8: Schematic draw of the Snooker Cue test, Panel in red, Gantry Rotation in black, Isocenter in the middle of the cross

6.2.6 Snooker Cue Test

The Snooker Cue test combines MU delivery versus gantry angle and MLC movement in one single check. It was introduced by van Esch et al. [32]. Here a slightly varied version of this test was used.
EPIDs are extremely fast and easy measurement tools for LinAc QA. But as they are mounted on the gantry and rotate in accordance with it, the images provided by the panel do not contain any information about the gantry angle, additional devices are necessary to get this information.
A metal rod of 26cm length was placed on the treatment couch and a displacement of 7cm in x direction and 5cm in y direction from the isocenter was introduced. As the gantry moves along the angles, the metal rod takes a different position in the image of the EPID depending on the gantry angle. The MLCs were programmed to follow the metal rod on its way across the detector, forming a gap which was automatically adjusted by the planning program. A margin of 7mm was kept to the edges of the rod, producing frames of images which always show a slit with the metal rod in the middle of it. The rod does not "move" across the field with constant but with varying speed, therefore MLC speed had to change during the irradiation. Dose rate was varied along the movement of the gantry as well to include all parameters of interest.

Figure 6.8 shows a very rough picture of the idea behind the Snooker Cue test. In figure 6.9 again all MLC positions at each control point are visible. This test was set up with 180 control points along the rotation of 360°. Therefore the MLC positions are not distinguishable any more in this simple picture.

This test was done including clockwise and counter-clockwise gantry rotation and MU output ranging from 200MU to 950MU to include different gantry speeds. The total covered gantry angle was 360deg.
This test is simple but covers all necessary parameters for VMAT QA. If some misplacements of the rod can be observed, further investigations with other tests have to be done to find out the cause of the misalignment.

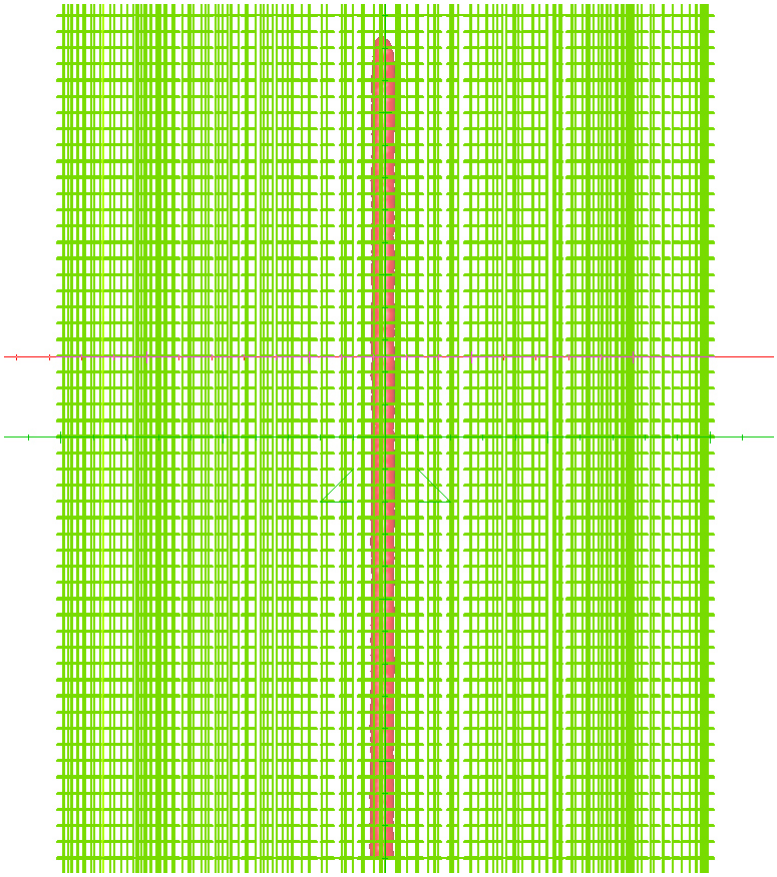

Figure 6.9: Snooker Cue Test, Field View in open-radART; green lines represent MLC positions at control point, all control points shown; metal rod in red

6.3 Testing and Analysis

The FPPI allows for various modes of image capturing. Single frame acquisition or average frame calculation as well as the combination of both options are possible. In clinical practice the average frame as well as some single frames will be captured and saved. In the evaluation phase more thoroughly investigation is necessary, therefore every frame had to be saved. This is only possible with the direct use of the FPPI through special modulation made possible in the GUI. Every image as well as the average frame were gathered for later analysis. The images are saved in a *.raw format containing a matrix of 1024 x 1024 values in unsigned 16 bit format. Therefore the values range between 0 and $2^{16} = 65536$. The available correction algorithms were already applied, but the values do not yet match the dose or dose rate. The final conversion follows a linear curve

$$DR = RS \cdot V + RI \tag{6.2}$$

where DR is the dose rate, RS stands for rescale slope, RI for rescale intercept and V is the value of the original matrix. When only single frames are examined, the conversion provides the user with dose rate information. Applying other correction factors on an average frame results in an image of the overall dose exposure.

The file name provides various values including these conversion factors, an example is shown here.

file_T_1387109447491_irKvS_-1_irP_-1_RS_0.0146258_RI_-58.5033_ X_1024_Y_1024.raw

The first number is the time in milliseconds when the image has been taken. RS and RI can also be found in the file name, they are constant for single frames.

$$RS = 0.0146258 \tag{6.3}$$

$$RI = -58.5033 \tag{6.4}$$

The last numbers define the image size.
To convert average files to dose images different conversion parameters are necessary. RS and RI are not provided in the file name and have to be calculated. This is done with additional use of the time stamps of the files. Subtracting the time stamp of the first image from the last image in the series the irradiation time can be calculated. Multiplying the time (in minutes) with the original RS and RI from the single frames provides the conversion values of the average image to dose values. As the test plans all had different durations these factors have been calculated for every test plan individually.

$$D = RS \cdot \triangle t \cdot V + RI \cdot \triangle t \tag{6.5}$$

Most files were analyzed using either MATLAB, The MathWorks, Inc., some additionally were examined with ImageJ, a public domain image processing software.
The MATLAB files are included in the appendix, but their basics are described in this section. All of them are written in function type to allow setting of different parameters like file name, thresholds or conversion factors.

The basic conversion had to be applied to every image, independent on whether it is a single frame or an average frame. Therefore a basic program for image preparation has been designed. The function is called with the file name and the corresponding conversion factors for either dose or dose rate. If these values are not defined, the image is handled as a single frame and RS and RI are set automatically according to the values from equation 6.4. Additionally a maximum value is defined as a cut off to better visualize the dose or dose rate. This cutting-off is necessary to remove remaining bad pixels which show a value which is too high compared to the rest of the image.
After the conversion to dose or dose rate is done the image is further processed depending on the test that was performed.

All tests were done various times over a period of seven months. During the course of testing additional parts of the FPPI were implemented as well as calibration of the detector has been updated. Differences in image quality output of the flat panel shall be analyzed and included in the analysis. In the beginning not every test was performed due to the unfinished FPPI. Three thorough runs which have been analyzed in depth have been executed where the tests have been done in both rotation directions and with varying dose rates.
Measurement dates were 2013-11-01, 2013-12-15 and 2014-03-23. Calibration of the flat panel was done directly before the first testing - on 2013-10-30. Included correction algorithms are MLG correction, Bad Pixel correction, Sync artifact correction and first level temperature correction. Other correction algorithms were not yet implemented. From the first to the second measurement date the dose output was not altered. On the third date the lowest and highest dose output were kept, measurements with dose output values in between were altered.

6.3.1 Dose Rates

After precedent conversion the images are further processed.
Analyzing the single frames stability of the dose rate can be observed. Blocks of frames should have the same dose rate, changes in accordance with leaf position can be examined as well as over or under travel of the leaves.
The average images which contain dose information have been analyzed more profoundly.
In the direction where the MLCs are located, the image matrix dimension has been reduced to the number of MLCs, i.e. 52, assigning each of these values the mean of three pixel values located in the middle of the position of each MLC. The other dimension represents the travel direction of the MLCs. In this direction the image was split into four segments, respectively for the four different applied dose rates.The segments were analyzed for their mean dose and deviation within the segment and compared to the other segments. Deviation of one segment to the other segments was observed as well. This was done in an overall observation as well as for every MLC separately.
Using the MATLAB code which can be found in the appendix, several images were produced which could be analyzed as well as overall values were produced which have been plotted in separate graphs.
Figure 6.10 shows some initial images of this test taken wit the panel. The FPPI was still under development, therefore initial results show huge differences to the final images which were used for profound analysis.
From the beginning on the test consisted of four segments, but initially not the whole field was covered which can be seen in part (a) and (b). The difference between them is a calibration which was renewed after the first measurements. The calibration process is done for each pixel individually and the result is obvious in figure 6.10 (b). The image is more smooth and does not show a different intensity in the center.
In part (c) and (d) the whole field was covered. Picture (c) was taken using recent calibration data, image (d) was a first try of the implementation of the multi - level gain correction but had an older calibration file as its background. Nevertheless obvious improvements can be seen in these images.

Considering the three measurements which were done with final calibration and corrections included lead to the following results.
Tables 6.7 to 6.9 give an overview of the basic results of these tests for all measurement dates. Mean intensity in each segment, as well as an estimate of the expected value, and the corresponding standard deviation is shown. Table 6.10 sums up all results for each dose output, figure 6.11 visualize the results of the measurements from 2013-11-01.
Deviations of the segment intensity from the expected value are within -5.7% and 8.7%. No dependence on the overall dose output can be observed, deviations do not vary in accordance with higher dose exposure.
The segments in the middle always show higher doses than the border segments. This behavior is expected due to the additional segments with low dose where the leaves move from one segment to the next one. On the last measurement date the third segment shows tendencies for a lower intensity as well. Highest values can mostly be found in the measurements of the first date and tend to decrease.

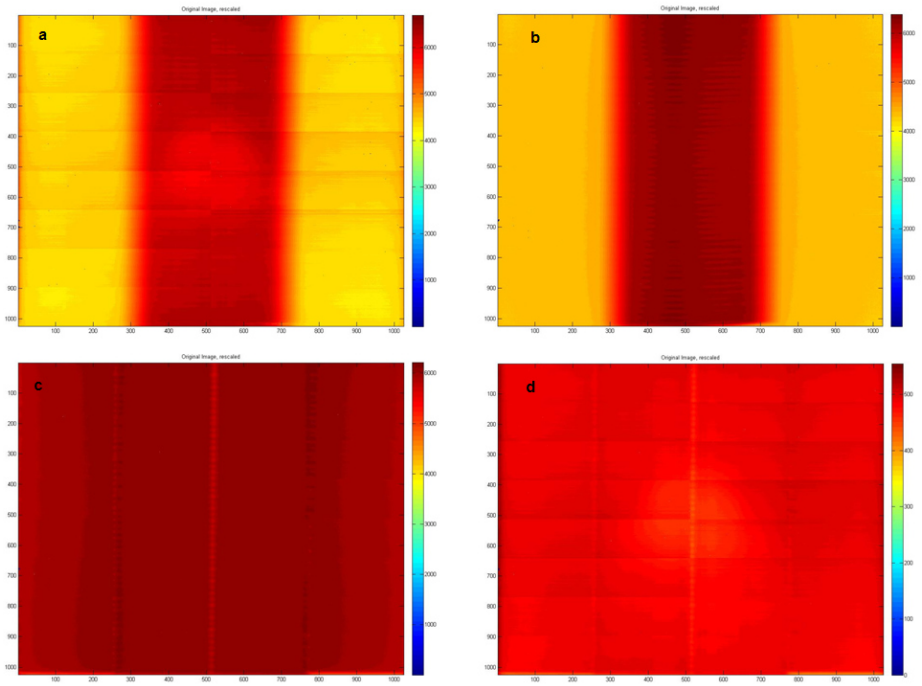

Figure 6.10: First Dose Rate Test Images; (a) First Test Setup, (b) First Test Setup with new Calibration, (c) Final Test Setup, (d) Final Test Setup with first MLG Correction

On the first measurement date the first segment always showed the lowest intensity whereas the third segment showed the highest dose. On the other measurement dates the highest dose could always be found in the second segment, the lowest in the forth. Although the over-all relative deviation was 14.4%, deviation in one test did not exceed 10%, the highest value could be found for 115MU cw on 2013-12-15 where -4.5% and +5.1% were measured.
Five different images were created with the MATLAB function. The with RS and RI corrected image, the image where one dimension represents the MLCs, a segmented image, the mean intensity in a segment for each MLC pair and the intensity deviation of one MLC pair along the four segments. One example for these images can be found in figure 6.12.

Output		Seg. 1	Seg. 2	Seg. 3	Seg. 4	Expected
90MU ccw	Mean Intensity	20.94	22.93	22.98	21.54	21.74
	Stand. Dev.	0.17	0.07	0.07	0.49	
90MU cw	Mean Intensity	21.55	23.30	23.56	22.16	21.74
	Stand. Dev.	0.17	0.30	0.26	0.67	
115MU ccw	Mean Intensity	26.88	29.14	29.59	27.46	27.77
	Stand. Dev.	0.23	0.20	0.27	0.99	
115MU cw	Mean Intensity	26.80	29.08	29.14	27.65	27.77
	Stand. Dev.	0.29	0.21	0.24	0.52	
150MU ccw	Mean Int.	35.96	38.94	39.44	36.79	36.23
	Stand. Dev.	0.59	0.16	0.9	0.84	
150MU cw	Mean Intensity	35.56	38.52	38.71	36.57	36.23
	Stand. Dev.	0.36	0.32	0.16	0.73	
225MU ccw	Mean Intensity	53.83	58.47	59.00	54.92	54.34
	Stand. Dev.	0.43	0.34	0.31	1.43	
225MU cw	Mean Intensity	53.16	57.63	57.83	54.72	54.34
	Stand. Dev.	0.55	0.29	0.25	1.08	
450MU ccw	Mean Intensity	107.53	116.87	118.15	109.74	108.68
	Stand. Dev.	0.78	0.61	0.66	3.37	
450MU cw	Mean Intensity	107.57	116.51	116.88	110.49	108.68
	Stand. Dev.	0.91	0.60	0.51	2.47	

Table 6.7: Results of the Dose Rate Test for Measurements on 2013-11-01

Output		Seg. 1	Seg. 2	Seg. 3	Seg. 4	Expected
90MU ccw	Mean Intensity	21.26	22.95	22.04	20.83	21.74
	Stand. Dev.	0.19	0.11	0.10	0.65	
90MU cw	Mean Intensity	20.75	22.12	21.42	20.51	21.74
	Stand. Dev.	0.26	0.15	0.31	0.36	
115MU ccw	Mean Intensity	26.98	29.04	28.04	26.45	27.77
	Stand. Dev.	0.23	0.13	0.17	0.73	
115MU cw	Mean Intensity	27.30	29.18	28.02	26.45	27.77
	Stand. Dev.	0.25	0.18	0.22	0.50	
150MU ccw	Mean Int.	35.73	38.30	37.22	35.11	36.23
	Stand. Dev.	0.64	0.30	0.35	0.59	
150MU cw	Mean Intensity	35.69	38.04	36.67	35.18	36.23
	Stand. Dev.	0.34	0.18	0.23	0.63	
225MU ccw	Mean Intensity	53.36	57.24	55.45	52.08	54.34
	Stand. Dev.	0.43	0.34	0.31	1.43	
450MU ccw	Mean Intensity	107.47	115.25	111.70	105.17	108.68
	Stand. Dev.	0.94	0.64	1.02	2.75	
450MU cw	Mean Intensity	107.32	114.65	110.26	105.85	108.68
	Stand. Dev.	1.05	0.64	0.76	2.04	

Table 6.8: Results of the Dose Rate Test for Measurements on 2013-12-15

Output		Seg. 1	Seg. 2	Seg. 3	Seg. 4	Expected
90MU ccw	Mean Intensity	21.40	22.52	21.38	20.58	21.74
	Stand. Dev.	0.35	0.36	0.45	0.45	
90MU cw	Mean Intensity	21.26	22.27	21.06	20.57	21.74
	Stand. Dev.	0.27	0.29	0.42	0.61	
100MU ccw	Mean Intensity	23.78	25.05	23.73	22.78	24.17
	Stand. Dev.	0.38	0.32	0.45	0.73	
100MU cw	Mean Intensity	24.21	25.33	23.89	23.29	24.17
	Stand. Dev.	0.29	0.21	0.24	0.52	
150MU ccw	Mean Int.	36.34	38.08	36.31	34.90	36.23
	Stand. Dev.	0.40	0.51	0.67	0.95	
150MU cw	Mean Intensity	35.66	37.17	35.22	34.46	36.23
	Stand. Dev.	0.40	0.49	0.65	0.72	
300MU ccw	Mean Intensity	71.31	74.94	71.28	68.34	72.45
	Stand. Dev.	1.23	1.01	1.37	1.50	
300MU cw	Mean Intensity	72.08	75.28	71.24	69.58	72.45
	Stand. Dev.	1.06	1.53	2.05	4.15	
450MU ccw	Mean Intensity	108.11	113.40	107.83	103.34	108.68
	Stand. Dev.	1.06	1.53	2.05	4.15	
450MU cw	Mean Intensity	107.40	112.27	106.11	103.71	108.68
	Stand. Dev.	1.66	1.47	1.95	2.09	

Table 6.9: Results of the Dose Rate Test for Measurements on 2014-03-23

Output	Minimum	Expected	Maximum	Percentage	
90MU	20.51	21.74	23.56	-5.6%	+8.4%
100MU	22.78	24.14	25.33	-5.6%	+4.9%
115MU	26.45	27.77	29.18	-4.8%	+5.1%
150MU	34.46	36.29	39.44	-5%	+8.7%
225MU	52.08	54.34	59.00	-4.2%	+8.6%
300MU	68.34	72.45	75.28	-5.7%	+3.9%
450MU	103.34	108.68	118.15	-4.9%	+8.7%

Table 6.10: Summary of the results of the dose rate test with relative deviations

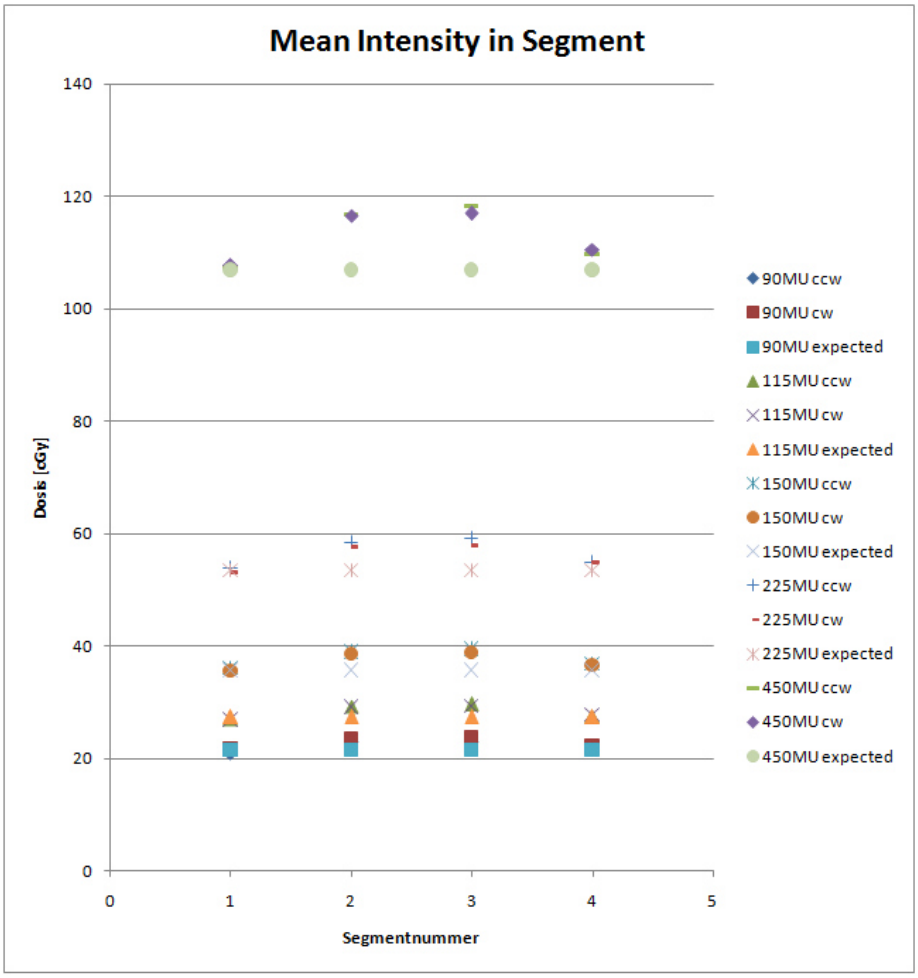

Figure 6.11: Results from the Dose Rate Test on 2013-11-01

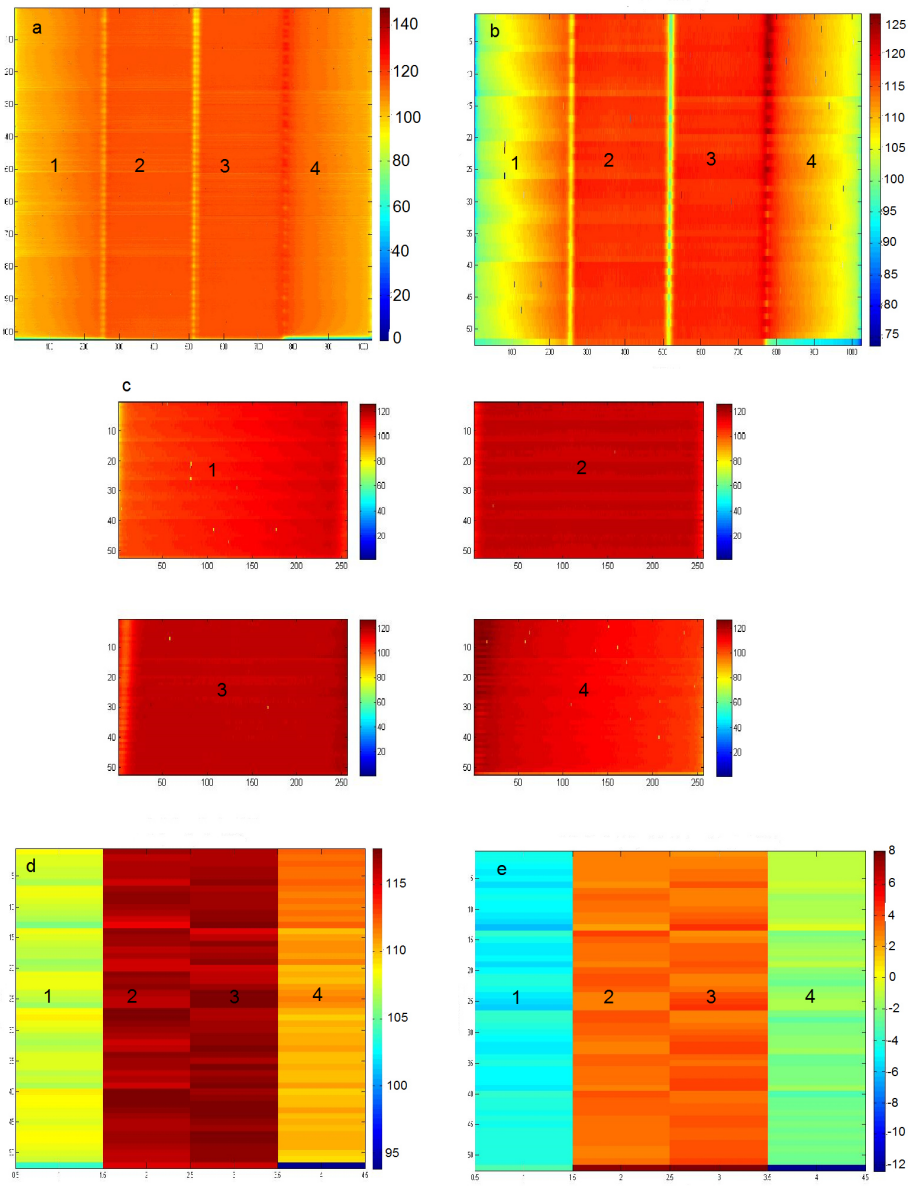

Figure 6.12: MATLAB Figures from the Dose Rate Test, from 2013-11-01 450MU cw; (a)Original Image, (b)Dimension reduced to MLC number, (c)Segmented Image, (d)Mean Intensity in each Segment for each MLC pair, (e)Deviation of intensity for each MLC pair along the four segments; Segments numbered

6.3.2 Dose Rate versus MLC leaf speed

This test was analyzed in a very similar way as the dose rate test.
Preprocessing has been done with the rescale slope and intercept values. Using the single frames leaf travel as well as dose rate change can be observed, stability of these two values is examined.

The focus was laid to the average image.
Again, the dimension was reduced to assign each vertical value to one MLC pair, therefore the matrix dimension decreases from 1024x1024 to 52x1024 pixels. The four segments for the four different dose rates and MLC speeds have been separated and analyzed on their own as well as compared to the other three segments. As small stripes with a much higher intensity due to overlap of the segment borders arose the segment length has been reduced by some pixels to exclude this effect. Mean and deviation of each segment and for the whole image has been calculated. MATLAB figures have been generated as well as graphs with plots of the summarizing values to analyze the results.

Development and improvement of image quality in this test can be observed in figure 6.13. Where the first image (a) shows an early arrangement of the four segments without recent detector calibration, the second image (b) had a new calibration file in its background. The last image (c) includes initial MLG corrections but again has an old calibration file as its basis. This shows as a the cold spot in the middle of the image where the panel is irradiated most frequently.

More emphasis was laid on the last three measurements where all available corrections have already been implemented. The results of the three dates are summarized below.

Tables 6.11 to 6.13 provide all values for each measurement date and test. Mean intensity as well as an estimate of the expected value and the corresponding standard deviation are shown. Table 6.14 sums up all results for each dose output, figure 6.14 visualize the results of the measurements from 2013-12-15.

Deviations of the segment intensity from the expected value are within -3% and 17.1%. No dependence on the overall dose output can be observed, deviations do not vary with higher dose exposure.
Segments in the middle tend to show a higher dose than the border segments. This behavior is expected at the very borders where the MLCs are starting their movement. On the last measurement day the third and forth segment tend to show a lower intensity than in earlier measurements. Highest values can always be found in measurements from the first date.

On 2013-11-01 the first segment showed lowest intensity, the third one highest in all measurements. On the second date lowest intensity could be found in either the first or the fourth segment, highest in the second or third. On the last date highest intensity was always measured in the second segment, lowest intensity in the forth segment.

The first measurement date showed significantly higher values than expected. The minimum value was never below the expected intensity value (with one exemption), the maximum value always showed a deviation of more than +10%.

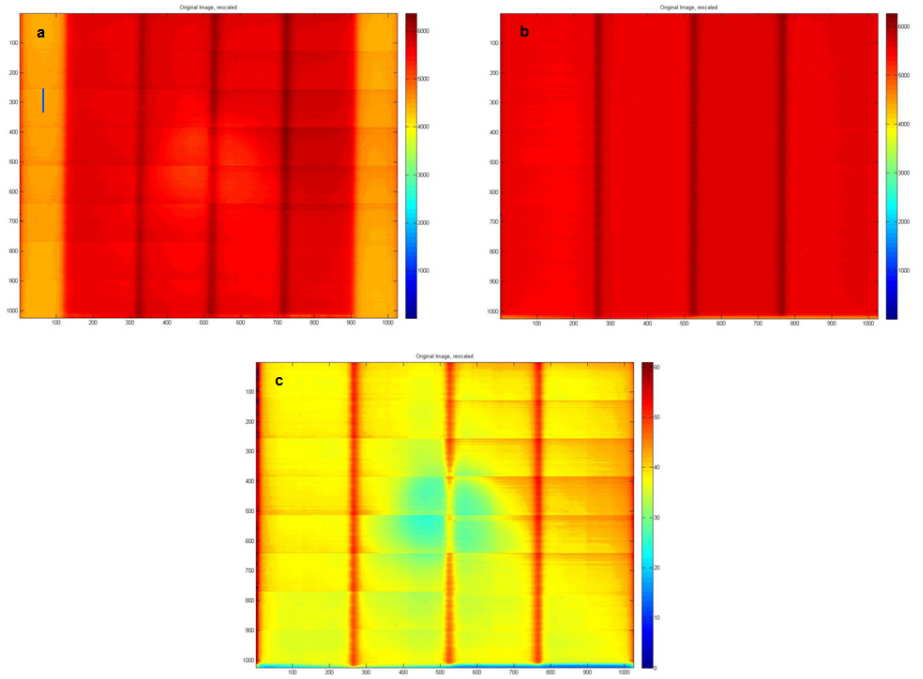

Figure 6.13: First DRMLC Test Images; (a) First Test Setup, (b) Final Test Setup with new Calibration, (c) Final Test Setup without Calibration but first MLG Correction

Disregarding the first measurement date the maximum positive deviation was 8.7%. In this measurement the minimum value exceeded the expected value as well.

Again, five MATLAB images were created. The first image is the corrected image using the RS and RI values. The second image shows the same image with reduced value for the dimension where the MLCs are located. The third image shows the segmentation, the last two show the mean intensity in a segment for each MLC pair and the intensity deviation of one MLC pair along the four segments. For an example, see figure 6.15.

Output		Seg. 1	Seg. 2	Seg. 3	Seg. 4	Expected
150MU ccw	Mean Intensity	18.27	19.76	20.97	19.51	18.75
	Stand. Dev.	0.43	0.30	0.82	0.76	
150MU cw	Mean Intensity	19.22	20.97	21.96	20.53	18.75
	Stand. Dev.	0.52	0.27	0.79	0.73	
190MU ccw	Mean Intensity	24.15	26.10	27.67	25.78	23.75
	Stand. Dev.	0.90	0.33	0.86	0.68	
190MU cw	Mean Intensity	24.18	26.25	27.54	25.77	23.75
	Stand. Dev.	0.29	0.21	0.24	0.52	
250MU ccw	Mean Int.	31.56	33.87	35.85	33.33	31.25
	Stand. Dev.	0.91	0.42	1.56	1.65	
250MU cw	Mean Intensity	31.93	34.65	36.25	34.00	31.25
	Stand. Dev.	0.91	0.37	1.27	0.92	
375MU ccw	Mean Intensity	47.79	51.22	54.18	50.54	46.88
	Stand. Dev.	1.25	0.54	2.28	2.07	
375MU cw	Mean Intensity	47.52	51.50	54.02	50.59	46.88
	Stand. Dev.	1.44	0.52	2.00	1.12	
750MU ccw	Mean Intensity	95.83	102.64	108.59	100.98	93.75
	Stand. Dev.	2.20	1.07	3.83	5.20	
750MU cw	Mean Intensity	94.90	102.85	108.04	100.72	93.75
	Stand. Dev.	2.89	1.20	3.06	3.43	

Table 6.11: Results of the DRMLC Test for Measurements on 2013-11-01

Output		Seg. 1	Seg. 2	Seg. 3	Seg. 4	Expected
150MU ccw	Mean Intensity	19.07	20.29	20.30	19.29	18.75
	Stand. Dev.	0.64	0.21	0.61	0.59	
150MU cw	Mean Intensity	18.16	19.54	19.49	18.41	18.75
	Stand. Dev.	0.48	0.21	0.62	0.58	
190MU ccw	Mean Intensity	24.40	25.66	25.82	24.28	23.75
	Stand. Dev.	0.48	0.21	0.62	0.58	
190MU cw	Mean Intensity	23.44	24.94	25.02	23.65	23.75
	Stand. Dev.	0.71	0.28	0.85	0.79	
250MU ccw	Mean Int.	31.65	33.22	33.40	31.68	31.25
	Stand. Dev.	1.06	0.34	1.06	0.96	
250MU cw	Mean Intensity	31.03	33.13	33.20	31.37	31.25
	Stand. Dev.	0.77	0.40	0.92	1.33	
375MU ccw	Mean Intensity	47.04	49.40	49.68	47.05	46.88
	Stand. Dev.	1.22	0.56	2.09	2.44	
375MU cw	Mean Intensity	46.82	49.62	49.67	47.07	46.88
	Stand. Dev.	0.99	0.57	1.05	2.02	
750MU ccw	Mean Intensity	95.22	100.00	100.42	95.17	93.75
	Stand. Dev.	2.34	1.16	4.29	5.01	
750MU cw	Mean Intensity	94.47	99.99	99.99	94.64	93.75
	Stand. Dev.	1.76	1.11	3.97	4.68	

Table 6.12: Results of the DRMLC Test for Measurements on 2013-12-15

Output		Seg. 1	Seg. 2	Seg. 3	Seg. 4	Expected
150MU ccw	Mean Intensity	18.96	19.36	19.05	18.60	18.75
	Stand. Dev.	0.64	0.38	0.83	0.72	
150MU cw	Mean Intensity	18.45	19.10	18.70	18.19	18.75
	Stand. Dev.	0.61	0.36	0.78	0.69	
250MU ccw	Mean Intensity	31.25	31.95	31.40	30.65	31.25
	Stand. Dev.	1.24	0.64	1.64	1.15	
250MU cw	Mean Intensity	30.87	31.90	31.25	30.44	31.25
	Stand. Dev.	0.96	0.58	1.28	1.14	
300MU ccw	Mean Int.	37.85	38.67	38.07	37.06	37.5
	Stand. Dev.	1.49	0.74	1.48	1.71	
300MU cw	Mean Intensity	37.25	38.50	37.65	36.72	37.5
	Stand. Dev.	1.21	0.70	1.83	1.28	
500MU ccw	Mean Intensity	63.04	64.40	63.23	61.67	62.5
	Stand. Dev.	2.55	1.32	3.23	2.87	
500MU cw	Mean Intensity	61.86	63.79	62.45	60.83	62.5
	Stand. Dev.	1.87	1.24	2.97	2.38	
750MU ccw	Mean Intensity	93.81	95.80	94.02	91.73	93.75
	Stand. Dev.	3.57	1.93	4.58	4.50	
750MU cw	Mean Intensity	93.44	96.26	94.31	91.91	93.75
	Stand. Dev.	2.92	1.90	4.11	3.30	

Table 6.13: Results of the DRMLC Test for Measurements on 2014-03-23

Output	Minimum	Expected	Maximum	Percentage	
150MU	18.16	18.75	21.96	-3.2%	+17.1%
190MU	23.33	23.75	27.67	-1.3%	+16.5%
250MU	30.44	31.25	36.25	-2.6%	+16.0%
300MU	36.72	37.5	38.67	-2.1%	+3.1%
375MU	46.82	46.88	54.18	-0.1%	+15.6%
500MU	60.83	62.5	64.40	-2.7%	+3.0%
750MU	91.73	93.75	108.59	-2.2%	+15.8%

Table 6.14: Summary of the results of the DRMLC test with relative deviations

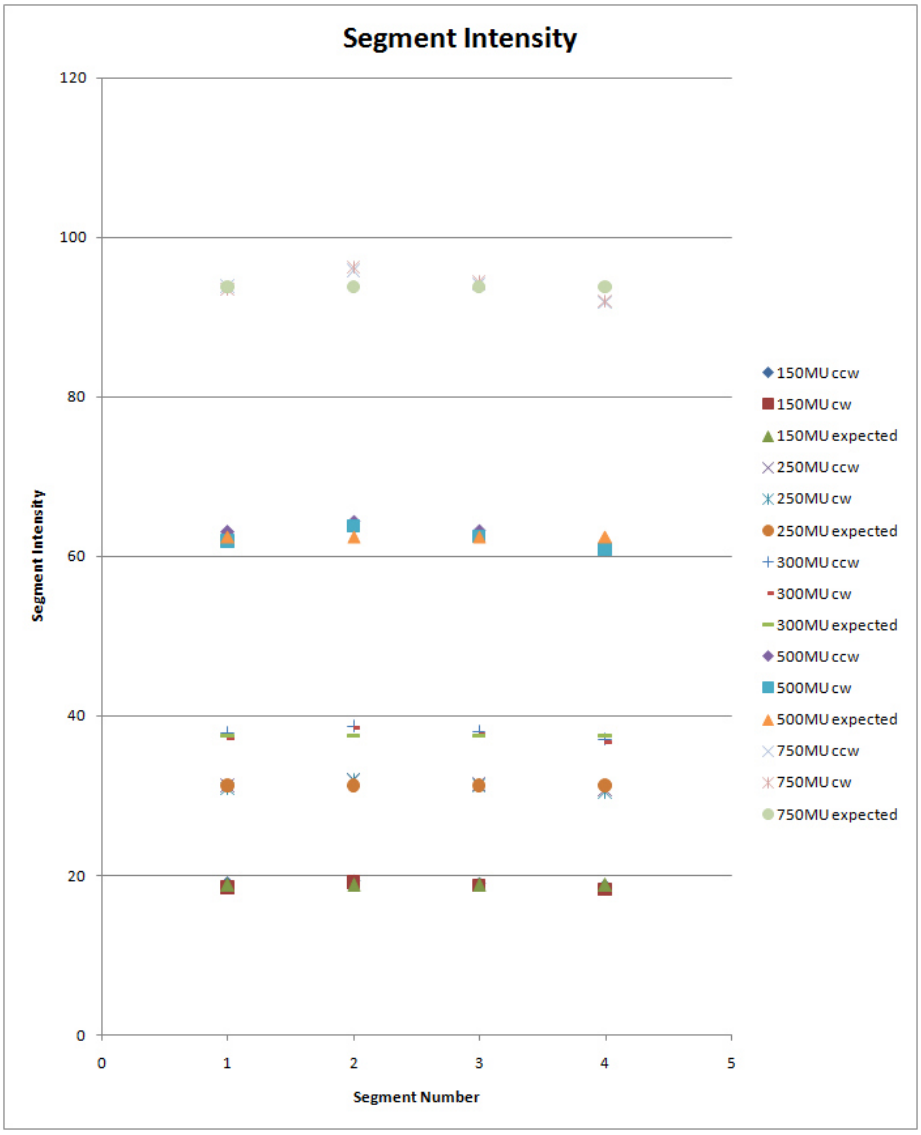

Figure 6.14: Results from the DRMLC Test on 2014-03-23

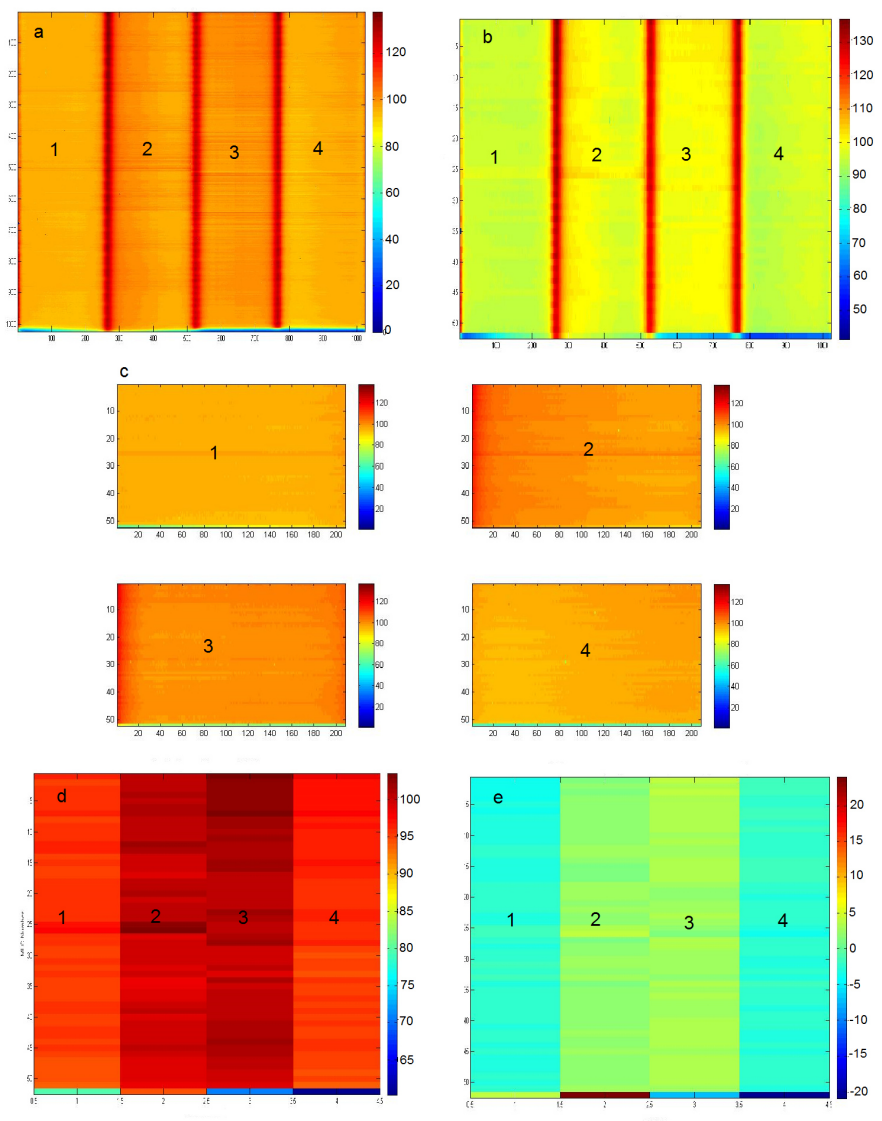

Figure 6.15: MATLAB Figures from the DRMLC Test, from 2013-12-15 750MU ccw; (a)Original Image, (b)Dimension reduced to MLC number, (c)Segmented Image, (d)Mean Intensity in each Segment for each MLC pair, (e)Deviation of intensity for each MLC pair along the four segments; Segments numbered

6.3.3 Picket Fence Test

Primary analysis was done similar to the two preceding tests. Conversion to dose rate or dose was followed by deeper analysis of the average image. One dimension was reduced to the number of MLCs before further examination was done. Afterwards the test specific analysis started.
Important values which have been examined are the positions of the gaps, their width and their intensity. MLCs which do not move correctly, f.e. stop at a wrong position during gap formation, can be identified.
Values below a certain threshold have been omitted to better localize the gaps. The remaining non zero elements have been further analyzed. Groups of less then ten pixels have been omitted as well. This way only the 'real' gaps remained. For these the mean position -weighted with the pixel intensity- (see equation 6.6) has been calculated and compared to the intended position. The gap should have a width of 0.6cm which corresponds to 24 pixels. Not only the mean position (i.e. the center) has been marked in the original image but also the intended borders have been sketched.
The mean intensity of the gaps has also been calculated as well as the overall value for each gap individually. These values can be compared to the intended values.
The mean intensities of the gaps have been plotted using their absolute values as well as the relative ones.
Ideally every gap should be at its intended position and each of them should have the calculated intensity. The MLC positions where the gaps are formed should be a straight line.

$$p(x_{MLC}, gap) = \frac{\sum_{I(x_{MLC},y)>threshold} I(x_{MLC}, y) \cdot y}{\sum_{I(x_{MLC},y)>threshold} I(x_{MLC}, y)} \tag{6.6}$$

Figure 6.16 shows images of the picket fence test in different situations. An initial test setup is shown in image (a), image (b) was already done with the final arrangement. Again the missing recent calibration is visible as the cold spot in the middle of the image. Image (c) was done after recent calibration of the panel, image (d) was done with initial MLG calibration but with an old calibration file in the background.

On the three dates where measurements have been done with all available correction algorithms, the resulting images have been analyzed profoundly as described above.
Tabel 6.15 shows the gap positions which were calculated according to equation 6.6. The positions do not vary depending on the date but show increasing deviations with increasing gap number (irradiation starts with gap 10). Additionally no dependence of the gap positions due to the used dose output could be found. Figure 6.17 shows the calculated deviation from the expected pixel position. Maximum deviation was found to be 8 pixels which corresponds to an absolute displacement of $0.2cm = 2mm$.

The calculated gap intensities were analyzed for each gap and for each measurement separately. Gaps during one measurement showed approximately the same dose with acceptable variations. The calculated mean intensity were compared to the expected value, their deviation analyzed as well. The values can

GapNr.	1	2	3	4	5	6	7	8	9	10
exp.	102	193	284	375	466	557	648	739	830	921
11-01	102	194	287	379	471	563	654	745	836	928
12-15	104	195	288	380	472	564	655	746	838	929
03-23	102	194	287	379	471	563	654	746	837	928

Table 6.15: Mean Gap Positions of the Picket Fence Test

be found in table 6.16, figure 6.18 gives an example for all gaps and dose output of 2013-12-15.
Two things attracted the attention. Measurements of 2014-03-23 all showed a deviation of about -40%, but remained in an intervall of 3.6%. Additionally the threshold for gap detection had to be decreased in the analyzing MATLAB function to get useful results. This behavior strongly suggests a systematical error. Further observation of the average image confirms this presumption. Figure 6.21 shows such an average image. It is quite obvious that the detector calibration needs to be renewed. This is not only evident due to the understated values but also shows as rubbed out pickets. Calculated gap positions on this date do not show any suspicious behavior.
Deviation of the gap intensity of 117MU on 2013-12-15 showed exceptionally high values from 16.3% to 16.8%. This is probably caused by the very low overall dose output.

Disregarding these two groups of measurements the deviations can be found in between -7.4% and $+5.4\%$. This deviation seems to be reasonable.

The calculated values originate from the MATLAB function for picket fence test evaluation. Additionally, other graphs and images have been created and can be found in figure 6.19 and 6.20. The first image shows the calculated mean gap intensity using the absolute and relative value of one measurement. The second image shows the original image which was only corrected with RS and RI and the same image overlaid with the calculated gap positions and borders.
Taking a closer look at the image with the overlaid gap positions reveals a certain deviation angle of the gaps from the intended angle which should be zero. Gaps tend to show a shift to the right. This tendency could be seen in all images, independent on the measurement date, dose output or rotation direction and is probably due to wrong panel positioning in the cassette.
Analysis of the image with reduced dimensionality (where one axis represents the MLC pairs) only shows MLC positioning deviations of less than 10 pixels. Including the uncertainty due to panel positioning no error of MLC positioning during gap formation which would have any impact could be found.
An interesting property can be observed during these test. As the difference in dose rate is quite high from one segment to the other and the LinAc is not capable to change the dose rate in an infinite small time difference, the gantry speed is reduced for a short time interval to make up for this behavior. This can be observed in the cameras which constantly monitor the irradiation room.

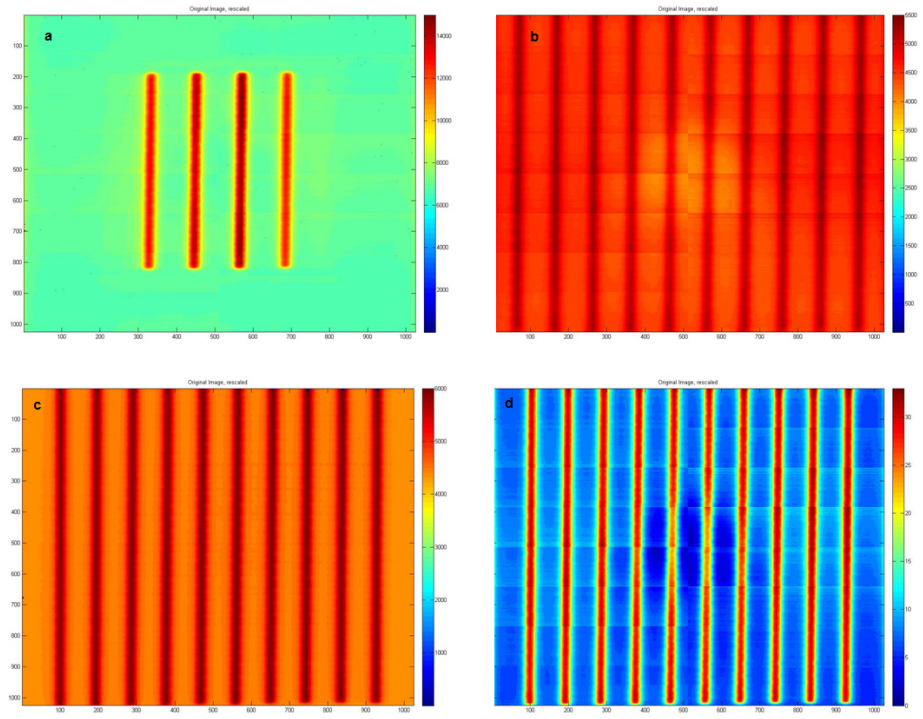

Figure 6.16: First Picket Fence Test Images; (a) First Test Setup with only four stripes, (b) Final Test Setup; (c) Final Test Setup with new Panel Calibration, (d) Final Test Setup without recent Calibration but first MLG Correction

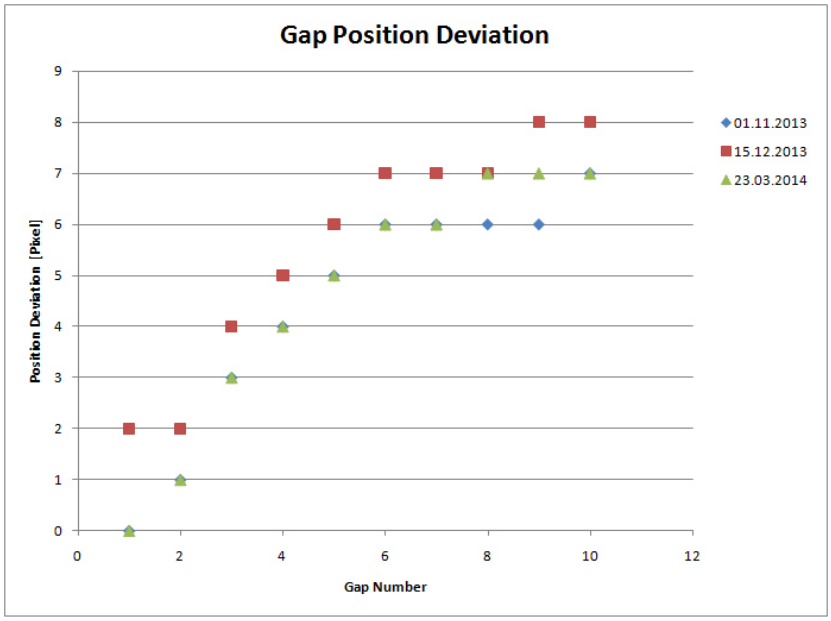

Figure 6.17: Gap Position Deviation from Expected Value

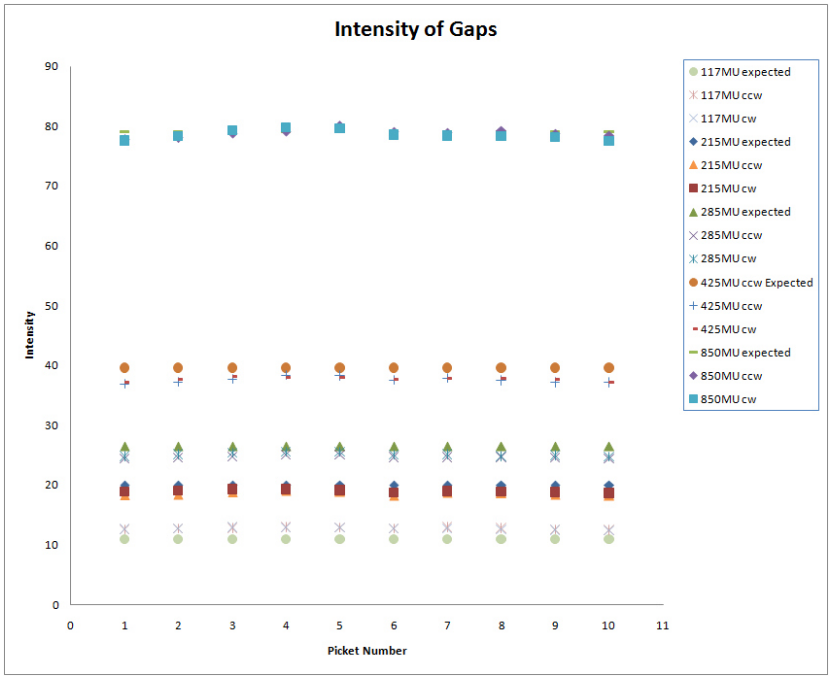

Figure 6.18: Gap Intensities of the Picket Fence Test; 2013-12-15

Date	Output	Expected Intensity	Measured Intensity	Deviation
11-01	215MU ccw	19.995	19.70	-1.5%
	285MU ccw	26.505	26.57	+0.3%
	285MU cw	26.505	26.42	-0.3%
	425MU ccw	39.525	40.11	+1.5%
	425MU cw	39.525	40.02	+1.3%
	850MU ccw	79.05	83.01	+5%
	850MU cw	79.05	83.31	+5.4%
12-15	117MU ccw	10.881	12.71	+16.8%
	117MU cw	10.881	12.66	+16.3%
	215MU ccw	19.995	18.52	-7.4%
	215MU cw	19.995	18.92	-5.3%
	285MU ccw	26.505	24.64	-7%
	285MU cw	26.505	25.07	-5.4%
	425MU ccw	39.525	37.52	-5%
	425MU cw	39.525	37.69	-4.6%
	850MU ccw	79.05	78.79	-0.3%
	850MU cw	79.05	78.51	-0.7%
03-23	170MU ccw	15.81	8.99	-43.4%
	170MU cw	15.81	8.93	-43.5%
	300MU ccw	27.9	16.73	-40%
	300MU cw	27.0	16.76	-39.9%
	600MU ccw	55.8	32.69	-41.4%
	600MU cw	55.8	32.70	-41.4%
	725MU ccw	72.075	42.81	-40.6%
	725MU cw	72.075	42.80	-40.6%
	850MU ccw	79.05	46.69	-40.9%
	850MU cw	79.05	46.44	-41.3%

Table 6.16: Mean Gap Intensity for each Picket Fence Test

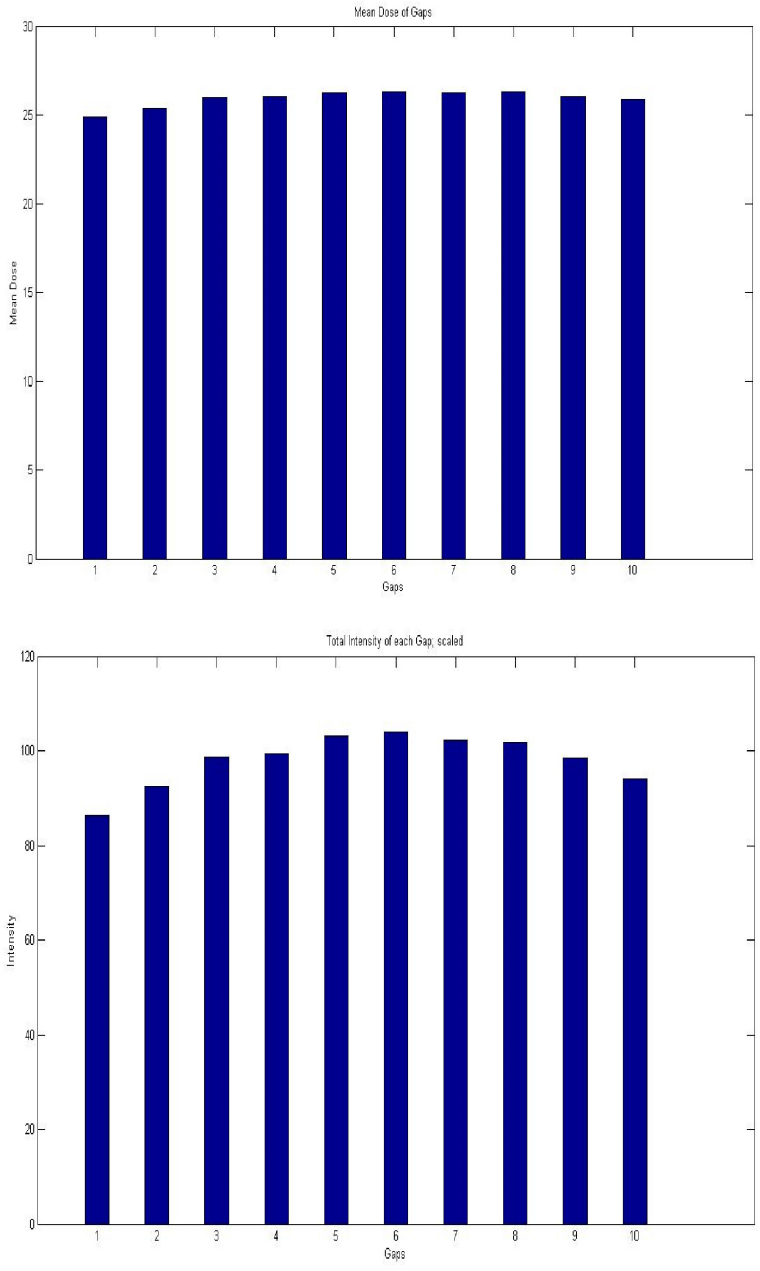

Figure 6.19: Absolute and Relative Gap Dose; 285MU cw, 2013-11-01

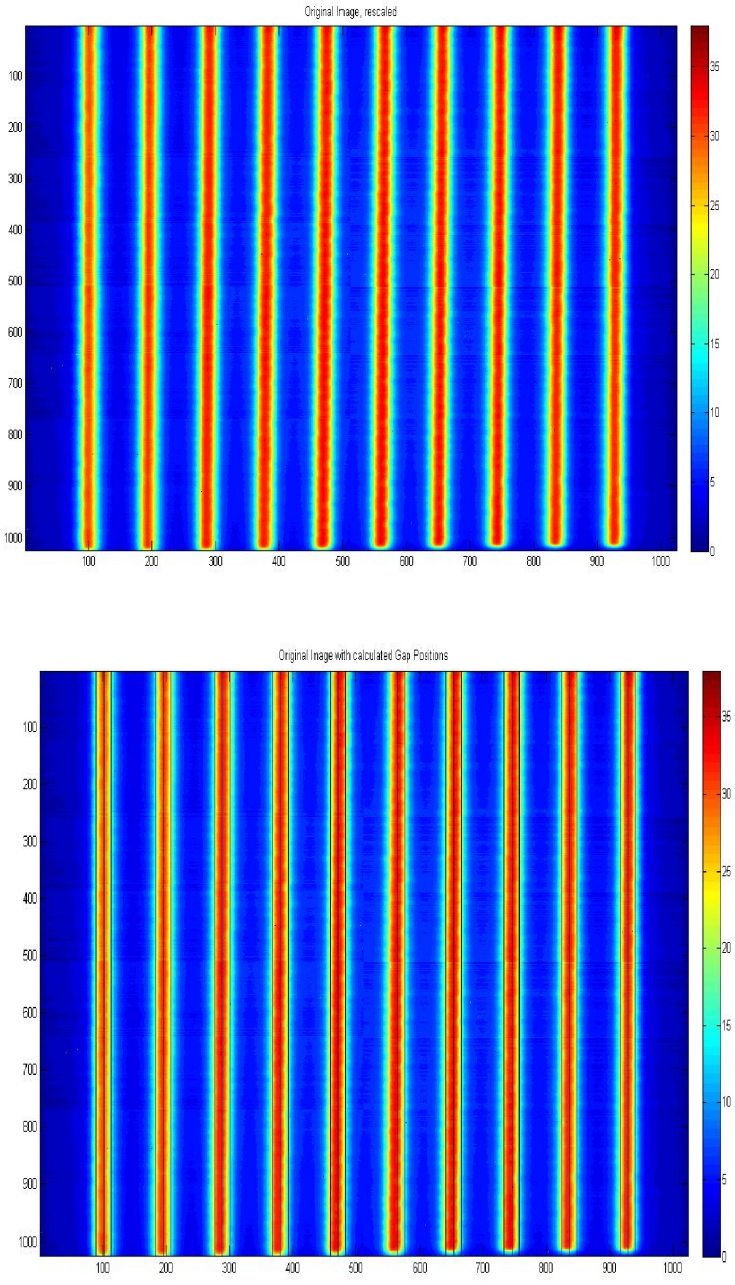

Figure 6.20: Original Image of the Picket Fence Test and Overlay with Calculated Gap Positions and Borders; 285MU cw, 2013-11-01

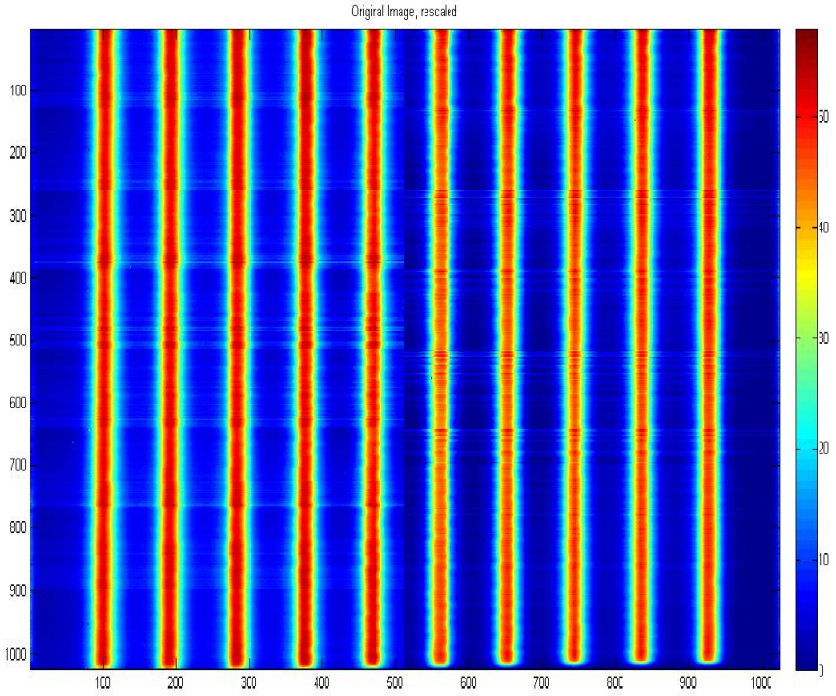

Figure 6.21: Dose Image of 850MU ccw, 2014-03-23

6.3.4 Dynamic MLCs

The dynamic MLC test has been analyzed similar to the first two tests. The main difference is the segment splitting which arises in the other dimension of the image than in the first two tests.

After primary conversion to dose or dose rate the focus has been put to the average image containing the dose.
The rows have been reduced to fit the MLC numbers. Mean values were given for each MLC. Afterwards the four groups which traveled with different velocity over the whole field have been separated. Individual analysis included mean intensity as well as deviation in the segment, for each MLC on its own. After the first group of MLCs arrive at the end of the panel, they stay there and keep the open slit. Therefore high intensities can be observed at the end of the field. To exclude this behavior in the examination of the deviation and mean calculation, the last pixels have been excluded.

The four segments could not be compared because they should have different intensities. Ideally the deviation in one segment should be minimal, intensity proportions from one segment to the others should not vary much.

Figure 6.22 shows two early images of the dMLC test. The first one (a) was done with a recent calibration file but no MLG correction, where the second one (b) had a primary MLG correction included but did calculations with an old calibration file.

Measurements done on one of the three final dates were analyzed and shall be discussed here.
The segments were separated and the mean intensity and intensity deviation were calculated for every segment individually. The resulting numbers can be found in table 6.17, 6.18 and 6.19. No expected values could be calculated as no program to do so was available yet. Therefore the values can not be compared to an absolute value but only compared among themselves. Additionally the deviation in the segments should be low.
Figure 6.23 shows a graphical illustration of results from the dMLC Test on 2013-12-15.
Especially for low doses the values are not reproducible. No decisive distinction can be seen between the lower dose output measurements as the results are located too close to each other. Measurements on the first date showed the highest values and decreased afterwards. Values of the last segment where the MLCs moved slowest and therefore the highest intensity could be found can somehow be found in similar regions but showed great deviations nevertheless. In summary it can be said that the dose exposure was always in regions were noise plays a major role and therefore could not be analyzed profoundly.

Figure 6.24 shows the images attained with the MATLAB function. The original image which was only rescaled is shown, as well as average intensity images over one MLC pair and over one segment. Additionally mean intensity in one segment and intensity deviation are displayed.

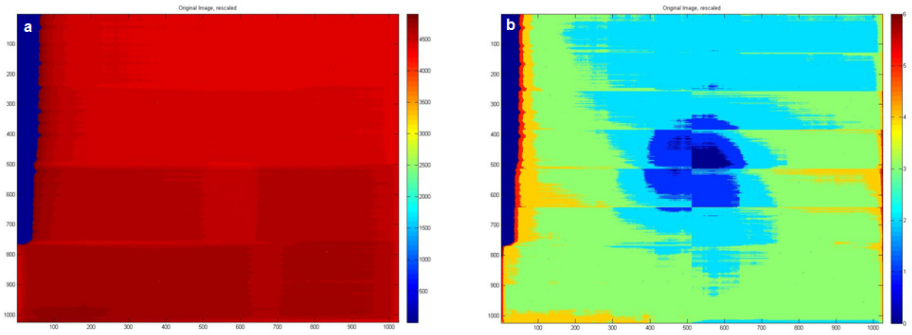

Figure 6.22: First dMLC Test Images, (a) Final Test Setup with new Calibration, (b) Final Test Setup without recent Calibration but first MLG Correction

Output		Seg. 1	Seg. 2	Seg. 3	Seg. 4
135MU ccw	Mean Intensity	2.54	2.90	3.89	4.47
	Stand. Dev.	0.15	0.07	0.11	0.16
135MU cw	Mean Intensity	1.99	2.20	3.23	3.92
	Stand. Dev.	0.01	0.14	0.11	0.08
170MU ccw	Mean Intensity	1.62	1.93	3.09	3.91
	Stand. Dev.	0.13	0.06	0.13	0.09
170MU cw	Mean Intensity	1.99	2.32	3.67	4.33
	Stand. Dev.	0.02	0.17	0.14	0.15
225MU ccw	Mean Int.	2.89	3.34	4.90	5.90
	Stand. Dev.	0.05	0.16	0.13	0.13
225MU cw	Mean Intensity	2.14	2.74	4.48	5.50
	Stand. Dev.	0.09	0.13	0.20	0.16
338MU ccw	Mean Intensity	4.27	5.09	7.60	9.09
	Stand. Dev.	0.14	0.20	0.23	0.27
338MU cw	Mean Intensity	3.93	4.66	7.23	8.71
	Stand. Dev.	0.06	0.18	0.26	0.19
675MU ccw	Mean Intensity	8.28	9.86	14.90	17.87
	Stand. Dev.	0.20	0.34	0.49	0.52
675MU cw	Mean Intensity	8.29	9.77	14.90	17.92
	Stand. Dev.	0.21	0.40	0.46	0.46

Table 6.17: Results of the dMLC Test for Measurements on 2013-11-01

Output		Seg. 1	Seg. 2	Seg. 3	Seg. 4
135MU ccw	Mean Intensity	1.23	1.44	2.37	3.15
	Stand. Dev.	0.11	0.06	0.08	0.14
135MU cw	Mean Intensity	1.19	1.43	2.38	3.05
	Stand. Dev.	0.08	0.06	0.07	0.15
170MU ccw	Mean Intensity	1.49	1.77	3.06	3.87
	Stand. Dev.	0.10	0.19	0.13	0.2
170MU cw	Mean Intensity	1.49	1.74	3.06	3.84
	Stand. Dev.	0.02	0.17	0.13	0.15
225MU ccw	Mean Int.	1.52	2.03	3.45	4.55
	Stand. Dev.	0.02	0.21	0.04	0.22
225MU cw	Mean Intensity	2.51	2.85	4.40	5.43
	Stand. Dev.	0.01	0.18	0.09	0.10
338MU ccw	Mean Intensity	3.54	4.12	6.45	8.20
	Stand. Dev.	0.08	0.24	0.16	0.36
338MU cw	Mean Intensity	3.09	3.70	6.09	7.71
	Stand. Dev.	0.17	0.18	0.18	0.27
675MU ccw	Mean Intensity	6.79	8.11	12.83	16.10
	Stand. Dev.	0.21	0.36	0.35	0.69
675MU cw	Mean Intensity	6.32	7.51	12.28	15.59
	Stand. Dev.	0.15	0.33	0.32	0.48

Table 6.18: Results of the dMLC Test for Measurements on 2013-12-15

Output		Seg. 1	Seg. 2	Seg. 3	Seg. 4
135MU cw	Mean Intensity	0.87	1.06	1.95	2.54
	Stand. Dev.	0.11	0.10	0.11	0.05
250MU ccw	Mean Intensity	1.92	2.23	3.88	5.19
	Stand. Dev.	0.11	0.17	0.15	0.28
250MU cw	Mean Intensity	1.91	2.20	3.85	5.16
	Stand. Dev.	0.10	0.15	0.14	0.22
320MU ccw	Mean Int.	2.04	2.37	4.50	6.08
	Stand. Dev.	0.15	0.20	0.22	0.35
320MU cw	Mean Intensity	2.55	2.90	5.04	6.68
	Stand. Dev.	0.21	0.19	0.20	0.25
450MU ccw	Mean Intensity	3.09	3.62	6.60	8.88
	Stand. Dev.	0.24	0.27	0.32	0.37
450MU cw	Mean Intensity	3.46	3.92	6.90	9.15
	Stand. Dev.	0.24	0.27	0.25	0.42
675MU ccw	Mean Intensity	5.58	6.40	10.91	14.30
	Stand. Dev.	0.35	0.46	0.45	0.66
675MU cw	Mean Intensity	5.12	5.87	10.39	13.84
	Stand. Dev.	0.36	0.41	0.38	0.55

Table 6.19: Results of the dMLC Test for Measurements on 2014-03-23

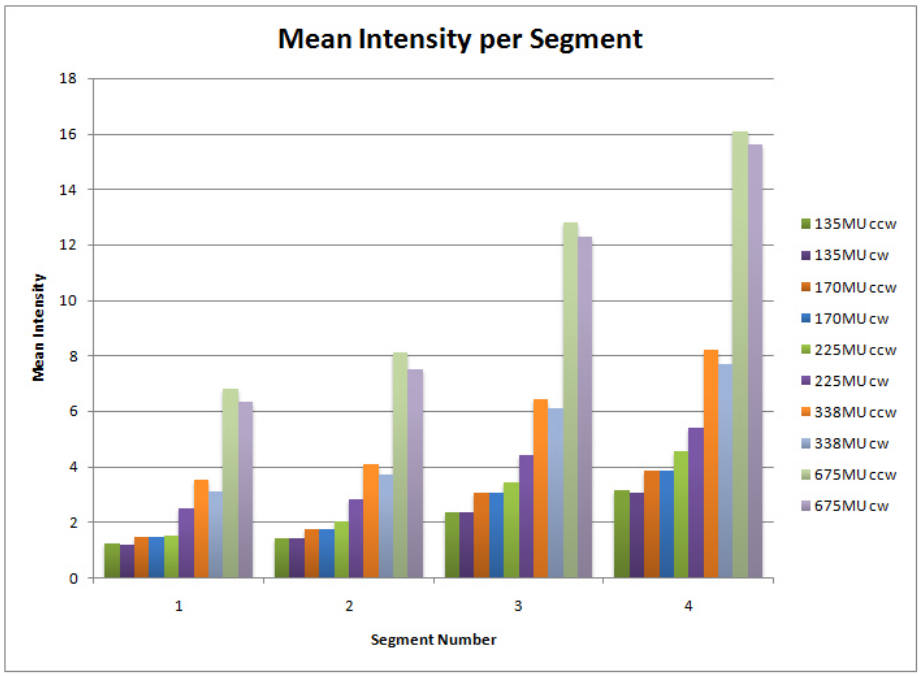

Figure 6.23: Segment Intensities of dMLC Test, 2013-12-15

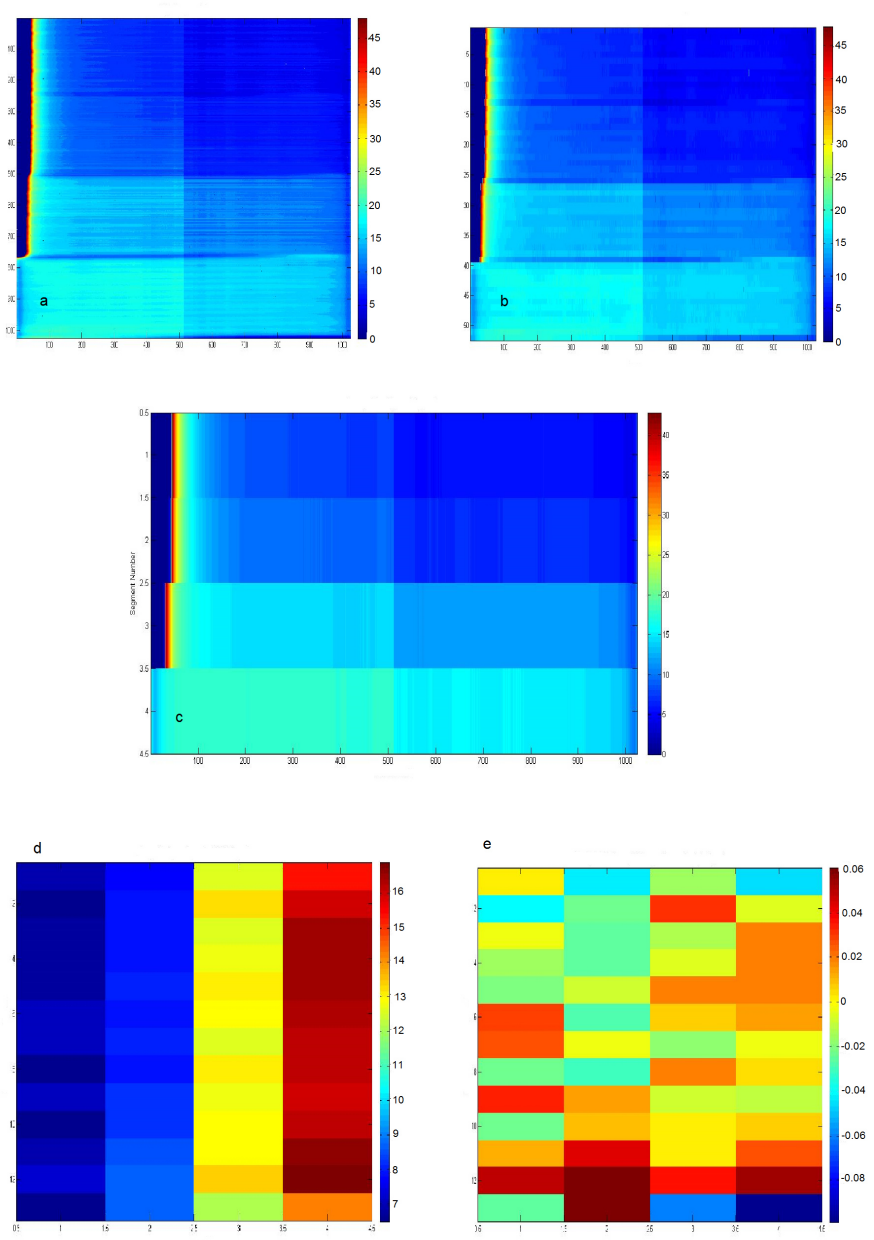

Figure 6.24: MATLAB Figures of dMLC Testing, 675MU ccw, 2013-12-15; (a)With RS and RI corrected Image, (b)One Dimension reduced to Number of MLCs, (c)Mean Intensity over the whole Segment, (d)Mean Intensity in every Segment for every MLC Pair, (e)Intensity Deviation of every MLC pair in each Segment

6.3.5 Sliding Slit

Sliding Slit test analysis has been kept quite simple.
The single frames are examined to inspect correct travel of the MLCs, especially the turning point poses a good examination point. Leaves should neither over nor under travel this position as they reach this point from both sides and start their reverse traveling.
Using the average image the over all behavior of the leaves as they travel across the field can be observed. Ideally the panel should be exposed to complete homogeneous dose. Important parameters to check this behavior are the mean dose and the deviation across the whole field. Mean dose in dependency of the over all dose can be examined as well. Overall dose and mean dose should always show the same ratio.

Differences of the dose image of the sliding slit test is shown in figure 6.25. Image (a) shows an old setup with an old calibration file. The slit did not move over the whole field and a cold spot is visible in the middle of the image. Image (b) was done with a new calibration file, image (c) again used an old one but included initial MLG correction.

Figure 6.26 shows a corrected image of the Sliding Slit Test with 315MU, cw rotation direction, from 2013-11-01. Dose distribution seems to be quite homogeneous, a small slit in the middle of the panel with reduced intensity can be observed, stripes at the borders of the panel additionally show lower dose than expected.

Table 6.20 gives an overview of all measured parameters of the sliding slit test. Mean intensity and standard deviation has been measured for every image. On the first two dates the MU output has been the same, on the last date measurements were done with slightly altered output values.

Measured values are highest in the beginning and tend to decrease. No obvious difference can be observed between two rotation directions. Figure 6.27 visualizes the results from 2013-11-01. Looking at the images the quality seem to decrease the more time decayed between the last calibration and the measurement. For comparison images of the other two dates are provided in figure 6.28 and 6.29. On the image from 2013-12-15 intensity depending on the side of the panel already shows visible deviation. On 2014-03-23 especially the middle of the panel additionally tends to decrease in displayed intensity. Although the slit sweeps over the panel three times, no satisfactory homogeneous dose distribution can be achieved. This behavior does not show up in the deviation calculation, mainly because the large deviations are caused by the borders and middle of the panel where the intensity can always be found on a lower level.
This is another indication that the panel might need a recalibration.

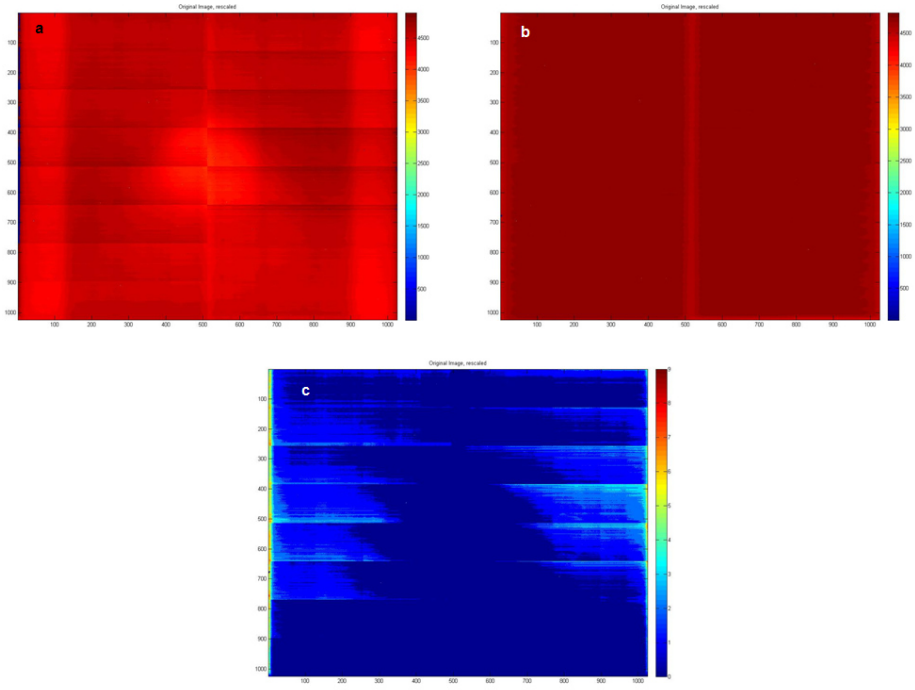

Figure 6.25: First Sliding Slit Test Images; (a) First Test Setup, (b) Final Test Setup with new Calibration, (c) Final Test Setup without recent Calibration but first MLG Correction

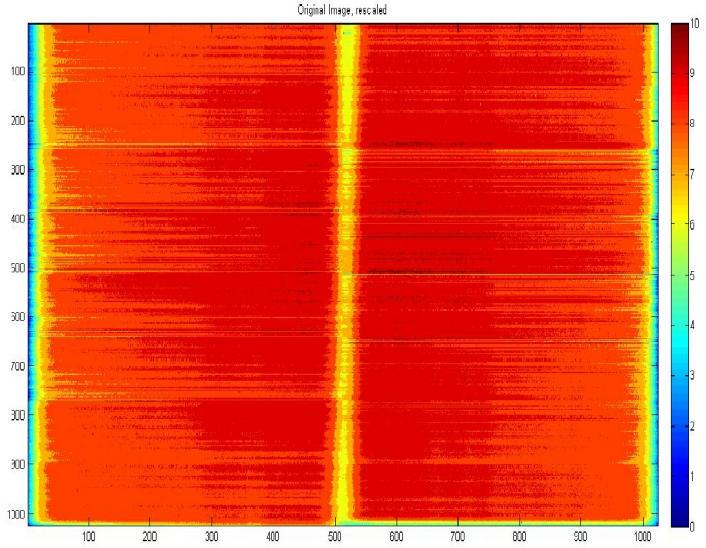

Figure 6.26: Image of the Sliding Slit Test, 315MU cw, 2013-11-01

	01.11.		15.12.			23.03.	
Output	Int.	Dev.	Int.	Dev.	Output	Int.	Dev.
190MUccw	4.58	0.67	3.91	0.49	190MUccw	4.11	0.72
190MUcw	4.65	0.68	3.91	0.54	190MUcw	4.27	0.71
240MUccw	5.89	0.79	5.43	0.71	275MUccw	5.72	0.96
240MUcw	5.93	0.80	5.85	0.70	275MUcw	5.72	1.00
315MUccw	7.73	1.03	7.22	0.88	350MUccw	7.56	1.18
315MUcw	8.22	1.07	7.30	0.91	350MUcw	8.12	1.20
475MUccw	12.11	1.54	11.04	1.30	600MUccw	13.17	1.98
475MUcw	12.66	1.60	11.16	1.36	600MUcw	13.39	2.04
950MUccw	24.65	3.01	22.31	2.58	950MUccw	20.95	3.16
950MUcw	24.65	3.14	21.89	2.73	950MUcw	20.39	3.24

Table 6.20: Results of the Sliding Slit Test, Int.=Intensity, Dev.=Deviation

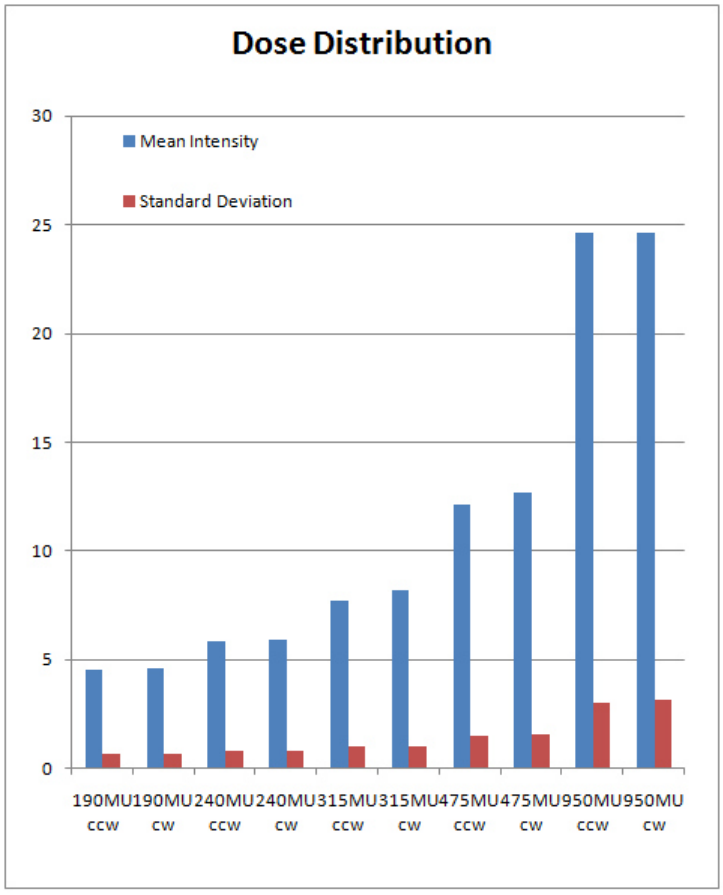

Figure 6.27: Results from the Sliding Slit Test, 2013-11-01

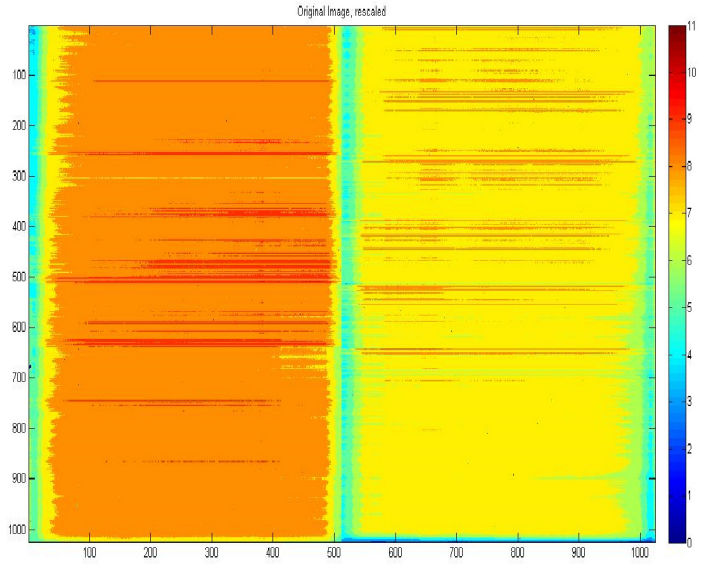

Figure 6.28: Image of the Sliding Slit Test, 315MU cw, 2013-12-15

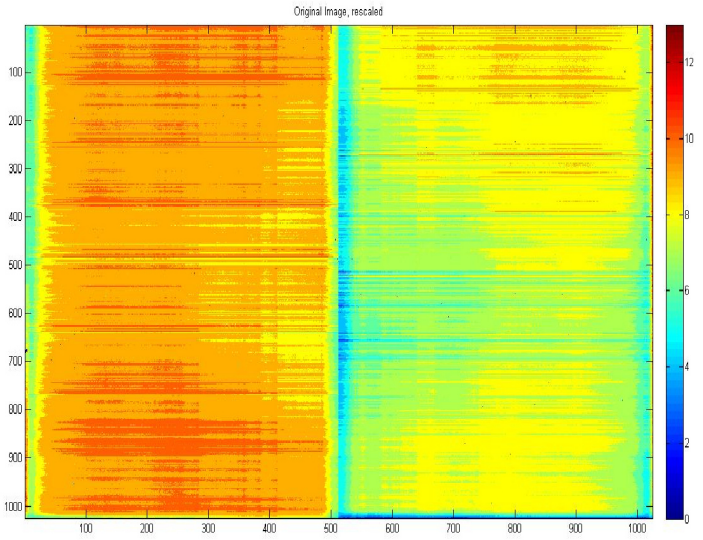

Figure 6.29: Image of the Sliding Slit Test, 350MU cw, 2014-03-23

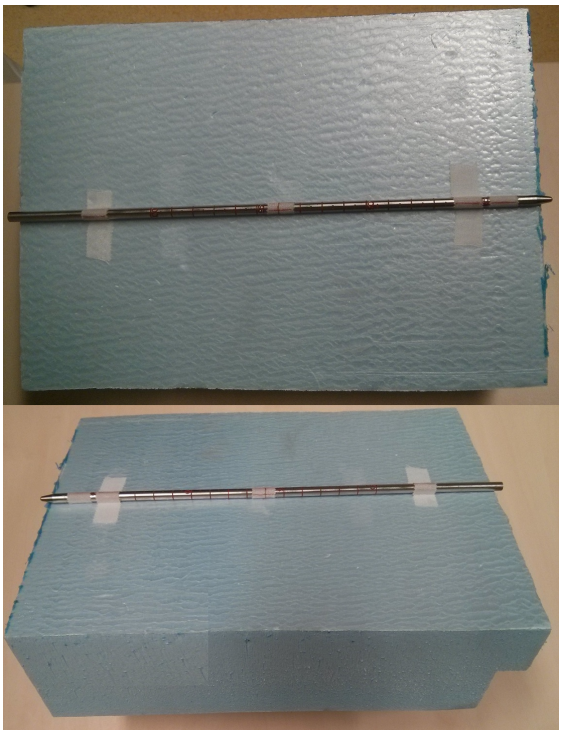

Figure 6.30: Metal Rod on supporting material used for Snooker Cue Test with marks for correct positioning

6.3.6 Snooker Cue

The Snooker Cue test has the nearest resemblance to a clinical patient plan. As correct positioning is an essential part of this test other installed devices on the LinAc have been used as helping resources.
A CT has been made of the metal rod (figure 6.30 shows the metal rod). Lasers are already included in this step to mark the isocenter (normally on the patient). Marks have been set on the rod using tags. For plan set-up the isocenter has been shifted in accordance with the desired values (7cm in x-direction, 5cm in y).

As the metal rod was placed on the treatment couch (see figure 6.32) it has been aligned with the lasers and therefore it was positioned directly at the isocenter; see figure 6.31. Using kV imaging and image guidance protocols the treatment couch has been moved with remote couch control as calculated by the algorithm. The values have been noted and compared to the desired distance from the isocenter of the LinAc itself.
The average image does not contain any useful information in this test and has therefore not been examined.
The single frames show the movement of the MLCs around the full gantry rotation. Optical analysis is done. The metal rod is clearly visible in all images if the right windowing is used depending on the current dose rate. As the dose

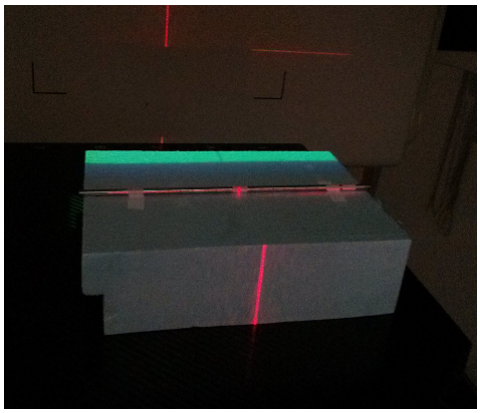

Figure 6.31: Built in Lasers used for correct positioning of the metal rod

rate changes during gantry rotation different frames show different values.
Two important characteristics can be observed.
The metal rod should always be visible in the middle of the slit defined by the MLC opening. Small rotation which normally can not be avoided by the person who placed the rod on the treatment couch can be visible but the position of the rod to the MLCs should not change. The projection of the metal rod onto the panel has a different size depending on the distance between the treatment head and the rod to the distance of the rod to the panel.
Additionally the frames can be correlated to the actual gantry angle. As the change in dose rate is programmed in accordance with a certain gantry angle, this parameter can now be checked as well.
If only one parameter does not coincide with the others, these differences would be visible immediately by misplacement of the rod to the MLCs.

The first dose rate change happens after 38 degrees, where it should change from 28 MU/min to 57 MU/min. After 136 degrees the dose rate increases to 115 MU/min, after 226 degrees to 233 MU/min and after 316 degrees to 463 MU/min. Therefore the dose rate changes should be visible after approximately 1/10th, 1/3rd, 2/3rd and 8/9th of the overall frames. Using the exact values and numbers of frames the point of dose rate change was examined.
As the increase of dose rate takes some time and additional errors of the panel had to be kept in mind, some deviation has been expected. Additionally the dose rate did not accord with the prescribed values, but varied daily.
The changes have been observed at the expected positions with reasonable deviations. These deviations result from not captured frames at the beginning on the second measurement date. The has content value has been set active in the FPPI, therefore some frames at the beginning may have been lost. On the third measurement date no has content check was used, therefore more frames than absolutely necessary may have been captured.
The lowest dose rate of 28 MU/min was not executed by the LinAc at all. This may be the result of a programming mistake but has to be further examined.
Calculated table shifts were (7.2,5.2) / (7.0,5.2) / (7.0,5.2) cm for the three measurement dates which correlate well with the intended values.

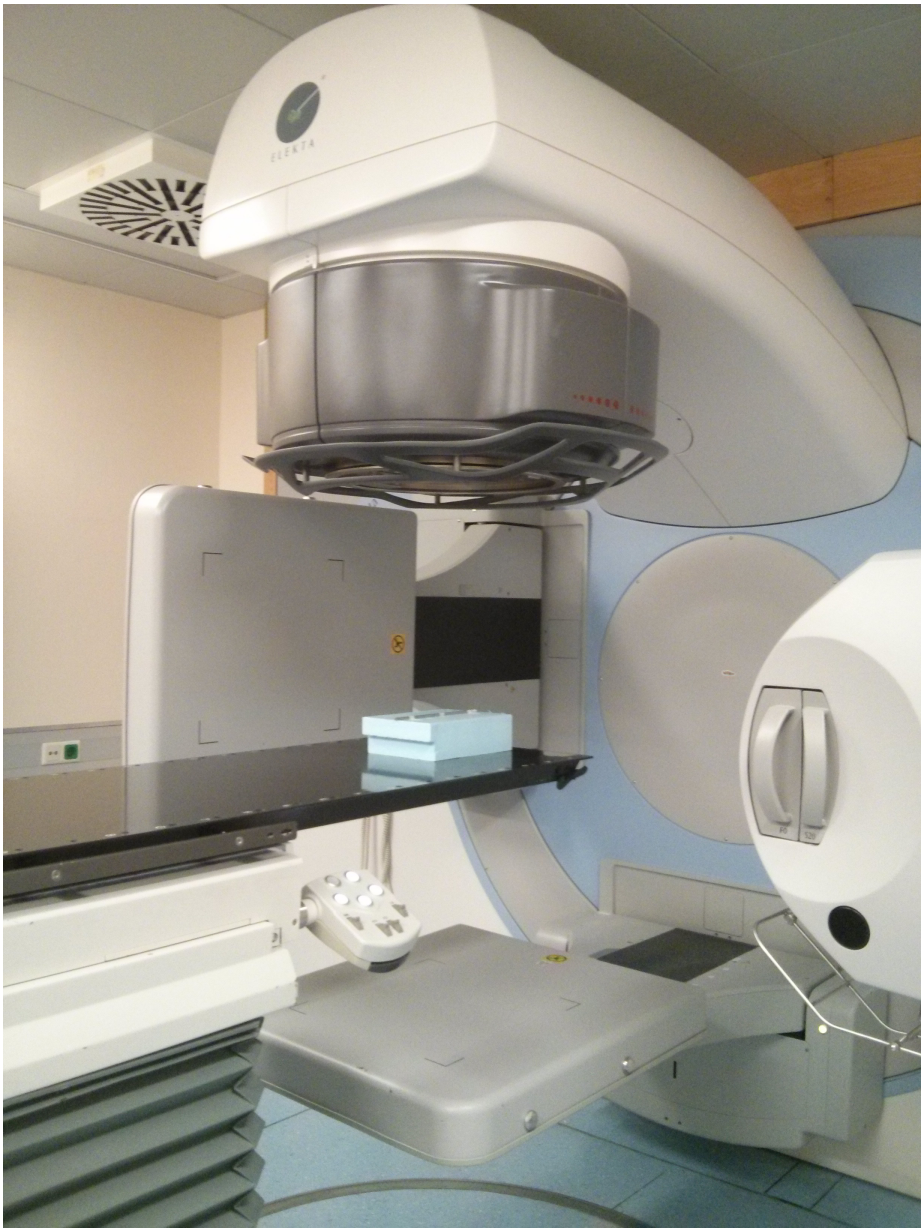

Figure 6.32: Metal Rod positioned in the isocenter of the LinAc; Panel underneath the treatment couch, tube and detector for kV imaging in horizontal direction

7 Conclusion and Prospect

All preclinical VMAT tests have been carried out various times with different dose output and gantry speed. They were done to evaluate the capabilities of the mechanical properties of the LinAc for the new radiation therapy technique Volumetric Modulated Arc Therapy. Additionally, absolute dosimetric measurements have been done with the flat panel which is mounted on the LinAc using a software which is still under construction - the Flat Panel Plug In.
Activating different modes of this software either dose or dose rate can be measured. Various correction algorithms have been implemented to achieve this conversion. Temperature dependencies, aging artefacts, artifacts from synchronous readout and take up of the signal as well as a multi level gain correction have been applied to the original signal. Nevertheless an error remains which still has to be corrected for using other correction algorithms.

The **Dose Rate Test** evaluated the application of different dose rates to achieve a homogeneous dose distribution over the whole panel. Four segments combining different dose rates and irradiation time have been set up and analyzed. Deviations were found in a range of -5.7% to $+8.7\%$ but did not exceed a 10% range in one test. Taking the inaccuracy of the panel into account this deviation is acceptable. A slight tendency for lower measured dose over time can be found but would have to be verified with additional measurements.

The **Dose Rate versus MLC leaf speed Test** confirmed the occurrence of decreasing measured dose in the panel images. During the first measurements absolute dose values in all segments exceeded the expected value and showed deviations of up to $+17.1\%$. Excluding the first measurements, the maximum deviations could be found in a range of -3.2% and $+8.3\%$, the largest range of intensity deviation in one measurement was 7.4%. Deviation ranges decreased with the measurement dates, highest deviations could be found on the first, lowest on the third date.

The **Picket Fence Test** showed high sensitivity to appropriate calibration of the detector. The first two measurements which were done close to the last calibration process showed acceptable outcome. Deviations of the gap intensity could be found in a range of -7.4% to $+5.4\%$, only the lowest output of 117MU showed values were the intensity exceeded the expected value around 16%. Measurements on the last date showed intensities which fell below 60% of the expected value. Deviations in this measurement were found to be in a range of -39.9% to -43.5%. Positioning of the gaps with the MLC pairs was accurate for all measurements. Deviations from the expected position increased on one side of the panel, absolute deviations were found to not exceed $0.2cm$. The images additionally showed a rotation of the panel in the cassette which is mounted on the LinAc due to bowed pickets.

The **dynamic MLC Test** did not create results which could be numerically analyzed. A lack of reproducibility showed that alterations to this test setup might be necessary to use this test for clinical purposes in the future. Overall intensity for each pixel was too low to permit reasonable analysis. Intended intensity differences in the four segments could be observed, MLCs at the borders of these segments did not show extraordinary behavior which eliminated the possibility of interactions between MLC pairs due to friction or motor failures.

The **Sliding Slit Test** showed low intensities as well but provided better numerical results because the slit formed by the MLCs does move across the panel three times in contrast to one time as with the dMLC test. Measurements on the first day showed acceptable homogeneous dose distributions and deviations across the whole panel area and provided reproducible results for the next measurements. Again the measured intensity showed a decreasing behavior with time. Relation of over all MU output of the LinAc and measured dose showed a good match. Images from the first date had a good optical appearance whereas results from the second and third date again indicated the necessity of a new calibration for the detector which especially shows as frazzling artifacts and a lower intensity area in the middle of the panel.

The **Snooker Cue Test** resembled closely a simplified treatment plan with one PTV and no OARs. The MLCs moved accurately in dependence of the gantry angle. Analysis of the single frames showed good results. Dose rate changes were observed at the intended frames which could be assigned to a certain gantry angle. This gantry angle could be found at about the intended values, including some deviation which is explainable due to inaccuracy of the panel and the measurement mode. This test included all new parameters for VMAT and showed that the interactions between these parameters works nicely.

In all tests the lowest part of the panel showed much lower dose than expected. Taking a closer look at the corrected images indicated and confirmed a deviation of the panel positioning in the cassette.
No dependency on the rotation direction of the gantry or the total MU output (and therefore the gantry speed) could be found in the tests.

In summary good results have been achieved using these preclinical tests. Some adjustments may have to be done if these tests should be regularly used in clinical practice but the over all set is satisfactory for the purpose of this project. The parameters which are new for VMAT have been tested individually and in combination, errors where found to be in an acceptable range.
The next step to bring VMAT into clinical use is the generation of VMAT patient plans. These plans will then be irradiated on the LinAc without a patient. Continuous measurements during the radiation need to be analyzed and checked for accuracy. This can be done with the panel. Using edge detection algorithms (see [29]) the MLC openings in each frame can be found, dose rate can be calculated as well in every image and correlated to the gantry angle. Therefore all parameters can be checked with the panel. Nevertheless additional measurements with other dosimetric devices like ionization chambers, diodes or films should be used for verification as measurements with the panel are still subjected to errors which are higher than clinically reasonable.
The flat panel provides a wide range of applications and possibilities. Measurements during the treatment could provide on-site imaging during irradiation and corrections during irradiation of a patient. Reconstruction algorithms can be used to calculate the applied dose and project it onto the CT images to check for correct dose deposition in the patient and allow adaption of the treatment plan after every fraction.
Various other methods may be possible and might be used in future, but patient security and doubtless correct irradiation have to be top priority in all cases.

References

[1] STATISTIK AUSTRIA, *Ergebnisse im Überblick: Gestorbene nach Todesursachen*, http://www.statistik.at/web_de/statistiken/gesundheit/todesursachen/todesursachen_im_ueberblick/index.html, last accessed November 2013

[2] Niteen B. More, Vijay Anand P. Reddy, *Radiation Oncology in 21st century-Changing the paradigms*. Apollo Medicine, Volume 9, Number 2, pp. 115-125, June 2012

[3] Faiz M. Khan, Ph.D., *The Physics of Radiation Therapy*, Third Edition. Lippincott Williams & Wilkins, 2003

[4] Ervin B. Podgorsak, Ph.D., *Radiation Physics for Medical Physicists*, Second Edition. Springer-Verlag, Berlin Heidelberg 2010

[5] C.J. Karzmark, C.S. Nunan, E. Tanabe, *Medical Electron Accelerators*, McGraw-Hill Professional, September 1992

[6] Varian Medical Systems, http://newsroom.varian.com/image/MLC+-+gold.jpg, last accessed January 2014

[7] KY Cheung PhD, *Intensity modulated radiotherapy: advantages, limitations and future developments*, Biomed Imaging Interv J 2006; 2(1):e19

[8] Michael Goitein, *Radiation Oncology: A Physicist's-Eye View*, Springer Verlag, 2008

[9] Ervin B. Podgorska, Ph.D., *Radiation Oncology Physics: A Handbook for Teachers and Students*, IAEA, Austria 2005

[10] Hanno Krieger, *Grundlagen der Strahlungsphysik und des Strahlenschutzes*, 2. überarbeitete und erweiterte Auflage. B.G.Teubner Verlag, Wiesbaden 2007

[11] Herbert Reich, *Dosimetrie ionisierender Strahlung, Grundlagen und Anwendungen*, B.G. Teubner, Stuttgart 1990

[12] Syed Naeem Ahmed, *Physics & Engineering of Radiation Detection*, Academic Press Inc. Published by Elsevier 2007

[13] Wikipedia, http://en.wikipedia.org/wiki/TNM_staging_system, last accessed January 2014

[14] T.S. Kehwar, Ph.D., D.Sc., S.C. Sharma, M.D., *Use of normal tissue tolerance doses into linear quadratic equation to estimate normal tissue complication probability*, http://www.rooj.com/Radiation%20Tissue%20Tolerance.htm, Department of Radiation Oncology, Sanches Cancer Center, Mercy Health Center, Laredo, Texas, USA; Department of Radiotherapy, Postgraduate Institute of Medical Education and Research, Chandigarh, India. Last accessed January 2014

[15] PTW Freiburg GmbH, http://www.ptw.de, last accessed March 2014

[16] Karl Otto, *Volumetric modulated arc therapy: IMRT in a single gantry arc*, Med. Phys. 35(1), January 2008

[17] M. Teoh, C.H. Clark, K. Wood, S. Whitaker, A. Nisbet, *Volumetric modulated arc therapy: a review of current literature and clinical use in practice*, The British Journal of Radiology, 84(2011), 967-996, June 2011

[18] Kjell Eriksson, Henrik Friberger, Erik Sterner, Camilla Blumentahl, *Volumetric Modulated Arc Therapy (VMAT) optimization with RayArc*, Raysearch White Paper, RaySearch Laboratories AB, 2009

[19] RaySearch AB, www.raysearchlabs.com/en/About-RaySearch/Research/White-papers/, last accessed January 2014

[20] Oscar Chang, M. Lee, A. Hung, A. Chang, R. Yeung, A. Lee, *The superiority of hybrid-volumetric arc therapy (VMAT) technique over double arcs VMAT and 3D-conformal technique in the treatment of locally advanced non-small cell lung cancer - A planning study*, Radiotherapy and Oncology 101 (2011) 298-302, September 2011

[21] Crag Elith, *A Retrospective Planning Analysis Comparing IMRT and VMAT for the Treatment of Prostate Cancer*, ISRRT World Congress and CAMRT Annual General Conference, Toronto, Canada, June 7-10, 2012

[22] P. Mayles, A. Nahum, J.C. Rosenwald, *Handbook of Radiotherapy Physics: Theory and Practice*, Taylor & Francis Group, 2007

[23] Larry E Antonuk, *Electronic portal imaging devices: a review and historical perspective of contemporary technologies and research*, Phys. Med. Biol. 47 (2002) RI31-65

[24] M. Mooslechner, B. Mitterlechner, H. Weichenberger, S. Huber, F. Sedlmayer, H. Deutschmann, *Analysis of a free-running synchronization artifact correction for MV-imaging with aSi:H flat panels*, Med.Phys. 40(3), March 2013

[25] S. Huber, M. Mooslechner, B. Mitterlechner, H. Weichenberger, M. Serpa, F. Sedlmayer, H. Deutschmann, *Image quality improvements of electronic portal imaging devices by multi-level gain calibration and temperature correction*, Phys.Med.Biol. 58 (2013) 6429-6446

[26] W. van Elmpt, L. McDermott, S. Nijsten, M. Wendling, P. Lambin, B. Mijnheer, *A literature review of electronic portal imaging for radiotherapy dosimetry*, Radiotherapy and Oncology 88 (2008) 289-309

[27] J.L. Bedford, A.P. Warrington, *Commissioning of volumetric modulated arc therapy (VMAT)*, Int.J. Radiation Oncology Biol. Phys., Vol. 73, No. 2, pp.537-545, 2009

[28] C.C. Ling, P. Zhang, Y. Archambault, J. Bocanek, G. Tang, T. LoSasso, *Commissioning and quality assurance of rapidarc radiotherapy delivery system*, Int.J. Radiation Oncology Biol. Phys., Vol 72, No.2, pp575-581, 2008

[29] M. Bakhtiari, L. Kumaraswamy, D.W. Bailey, S. de Boear, H.K. Malhotra, M.B. Podgosak, *Using an EPID for patient-specific quality assurance*, Med. Phys. 38 (3), March 2011

[30] M.K. Jorgensen, L. Hoffmann, J.B.B. Petersen, L.H. Praestgaard, R. Hansen, L.P. Muren, *Tolerance levels of EPID-based quality control for volumetric modulated arc therapy*, Med. Phys. 38 (3), March 2011

[31] P. Rowshanfarzad, M. Sabet, M. Barnes, D.J. O'Connor, P. Greer, *EPID-based verification of the MLC performance for dynamic IMRT and VMAT*, Med.Phys. 39(10), October 2012

[32] A.van Esch, D.P. Huyskens, C. Behrens, E. Samsoe, M. Sjölin, U. Bjelkengren, D. Sjönström, C. Clermont, L. Hambach, F. Sergent, *Implementing RapidArc into clinlical routine: A comprehensive program from machine QA to TPS validation and patient QA*, Med.Phys. 38(9), September 2011

[33] A. Mans, P. Remeijer, I. Olaciregui-Ruiz, M. Wendling, J. Sonke, B. Mijnheer, M. van Herk, J.C. Stroom, *3D Dosimetric verification of volumetric-modulated arc therapy by portal imaging*, Radiotherapy and Oncology 94 (2010) 181-187

[34] J. Richart, M.C. Pujades, J. Perez-Calatayud, D. Granero, F. Ballester, S. Rodriguez, M. Santos, *QA of dynamic MLC based on EPID portal dosimetry*, Physica Medica 28, 262-268, 2012

[35] D.G.L. Kaurin, L.E. Sweeney, E.I. Marshall, S. Mahendra, *VMAT testing for an Elekta accelerator*, Journal of applied clinical medical physics, Volume 13, Number 2, 2012

[36] C.-S. Chui, S. Spirou, T. LoSasso, *Testing of dynamic multileaf collimation*, Med.Phys. 23(5), May 1996

[37] T. LoSasso, C.-S. Chui, C.-C. Ling, *Physical and dosimetric aspects of a multileaf collimation system used in the dynamic mode for implementing intensity modulated radiotherapy*, Med. Phys. 30, 1919-1927, 1998

[38] M. Wendling, L.N. McDermott, A. Mans, J.J. Sonke, M. van Herk, B.J. Mijnheer, *A simple backprojection algorithm for 3D in vivo EPID dosimetry of IMRT treatments*, Med. Phys. 36(7), July 2009

[39] E. Klein, J. Hanley, J. Bayouth, F. Yin, W. Simon, S. Dresser, C. Serago, F. Aguirre, L. Ma, B. Arjomandy, C. Liu, *Task Group 142 report: Quality assurance of medical accelerators*, AAPM, Med. Phys. 36(9), September 2009

[40] International Electrotechnical Commission, *Evaluation and routine testing in medical imaging departements - Part 1: General aspects*, IEC 61223-1, 1993

[41] Deutsches Institut für Normungen, *Medizinische elektrische Geräte - Medizinische Elektronenbeschleuniger - Apparative Qualitätsmerkmale (IEC 60976:2007); Deutsche Fassung EN 60976:2007*, DIN EN 60976, February 2011

A Appendix

A.1 MATLAB Code

The MATLAB code was generated in the 2008 Version of the software and might not work with a newer version.
Additionally the algorithm has been written to specifically fit the tests for this project. Alterations might have to be done when other but similar tests are done and this code shall be used for analysis. Output of the code are graphs and images, interpretation of the results has to be done afterwards. No pass or fail criteria is implemented in the used functions.

A.1.1 General Preparation

```
%Function includes reading of .raw file and initial
    preparation

function imscale = prepare(fileName, maximum, varargin)

%define extra values
if nargin==4
    RS = varargin{1};
    RI = varargin{2};
else
    RS = 0.0146258;
    RI = -58.5033;
end

%read the file
fid = fopen(fileName);

if fid == -1;
    warning('File could not be opened');
    imscale = -1;
else
    % define dimensions
    Dim = [1024 1024];

    % read and reshape the data
    imorig = uint16(fread(fid,Dim(1)*Dim(2),'uint16'));
    imorig = reshape(imorig,Dim)';

    fclose(fid);

    % filter pixels with too high values
    imorig(imorig>maximum) = 0;

    % calculate dose/doserate
    imscale=imorig.*RS + RI;
```

```
    % show image
    figure(1);
    imagesc(imscale);
    title('Original Image, rescaled');
end

end
```

A.1.2 Dose Rates and DRMLC

Dose Rate Test and DRMLC Test were analyzed with the same algorithm. The only difference is the exclusion of some pixels in the border areas of the segment. Here the Dose Rate Test algorithm is shown.

```
%Function to calculate deviations of segment intensities
    for each MLC Pair seperately
%Segments are perpendicular to MLC Pairs

function [SegIm, MeanAv, StdInt] = Doserate(fileName,
    SegmentNumber, RS, RI)

numMLC = 52;

%reading and preparation of the image
img = prepare(fileName, 6000, RS, RI);

%Pixelwidth of one MLC pair
widthMLC = size(img, 2)/numMLC;

%Create Matrix which only has elements at the middle of
    each MLC pair this value is the mean of the 2 or 3
    surrounding values
meanIntMLC = zeros(size(img));
for i=1:numMLC
    meanIntMLC(ceil((i-1/2)*widthMLC),:) = mean(img(floor
        ((i-1/2)*widthMLC-1):ceil((i-1/2)*widthMLC+1),:));
end

figure(2);
imagesc(meanIntMLC);
title('Intensity for every MLC Pair');

pfimg = zeros(numMLC, size(img,2));
%compressing the matrix, include only mean for each MLC
    pair
for i=1:numMLC
    pfimg(i,:) = meanIntMLC(ceil((i-1/2)*widthMLC),:);
end
```

```
figure(3);
imagesc(pfimg);
xlabel('Image Pixel');
ylabel('MLC Number');
title('Intensity for every MLC Pair, merged');

%separate whole Matrix into Segments, preallocate third
    dimension for segments
SegLen = floor(size(meanIntMLC,2)/SegmentNumber);
SegIm = zeros(numMLC, SegLen, SegmentNumber);
MeanAv = zeros(numMLC, SegmentNumber);

%Matrix separation, plot all segments, calculate mean for
     every MLC for every segment
A = max(max(pfimg));

figure(4);
for i=1:SegmentNumber
     SegIm(:,:,i) = pfimg(:, ((i-1)*SegLen+1):(i*SegLen));
     subplot(2, SegmentNumber/2, i);
     imagesc(SegIm(:,:,i), [1 A]);
     MeanAv(:,i) = mean(SegIm(:,:,i),2);
end

figure(5);
imagesc(MeanAv);
xlabel('Number of Segment');
ylabel('MLC Number');
title('Mean Intensity over each Segment for each MLC Pair
    ');

%Calculate deviation of mean of MLC for each segment to
    mean for each MLC for the whole image
StdInt = zeros(numMLC, SegmentNumber);
for i=1:SegmentNumber
     StdInt(:,i) = (MeanAv(:,i)./mean(MeanAv,2)-1).*100;
end

figure(6);
imagesc(StdInt);
xlabel('Segment Number');
ylabel('MLC Number');
title('Deviation of Mean Intensity in Segment to Mean
    Intensity over whole Image (for each MLC Pair)');
end
```

A.1.3 Picket Fence

```
%Function for PicketFence Test

%Test should be evaluated and found gap positions plottet
     into the old picture for comparison
%Preparation needed
%Sum of intensities of every gap should be given as
    estimate for correct gap width
%Threshold defines sensitivity of algorithm for gap
    detection
%MLCs have to be be in row direction (x)

function [pfimg, gapIntensity2, totalgapInt2, gapPos,
    intmean] = picketfence(fileName, threshold, RS, RI)

numMLC = 52;

%reading and preparation of the image
img = prepare(fileName, 6150, RS, RI);

%Pixelwidth of one MLC pair
widthMLC = size(img, 2)/numMLC;

%Create Matrix which only has elements at the middle of
    each MLC pair this value is the mean of the 2 or 3
    surrounding values
meanIntMLC = zeros(size(img));
for i=1:numMLC
    meanIntMLC(ceil((i-1/2)*widthMLC),:) = mean(img(floor
        ((i-1/2)*widthMLC-1):ceil((i-1/2)*widthMLC+1),:));
end

%set all elements along the middle of the MLCs which are
    below a given threshold to zero
meanIntMLC(meanIntMLC<threshold) = 0;

figure(2);
imagesc(meanIntMLC);
title('Mean Intensity over all MLC Pairs (exceeding
    threshold)');

%locate and number gaps
pfimg = zeros(numMLC, size(img,2));
%compressing the matrix, include only mean for each MLC
    pair
for i=1:numMLC
    pfimg(i,:) = meanIntMLC(ceil((i-1/2)*widthMLC),:);
end
```

```
figure(3);
imagesc(pfimg);
xlabel('Pixel Number');
ylabel('MLC Number');
title('Intensity over Central Position of MLC Pairs');

%search for gaps, number them and return number of all
    gaps
[labeledData, gapnum] = bwlabel(pfimg);

ind=zeros(1,2);
%search for gap with highest number of pixels
for i=1:gapnum
    [r, c] = find(labeledData==i);
    rc = [r c];
    if size(rc,1)>size(ind,1)
        ind=rc;
    end
end

%preallocate matrix which contains positions of all gaps
gappos = zeros(size(ind,1), 2*gapnum);

%for each gap two colomns which contain positions of the
    gap, check if there are more then 10 points for each
    detected gap, discard elsewhere (probably noise), sort
     them on their number of MLC pair
for i=1:gapnum
    [m, n] = find(labeledData==i);
    if size([m n],1)>20
        gappos(1:size([m n],1), (2*i-1):(2*i)) = [m n];
        gapmlc(1,i) = size([m n], 1);
    end
end

j=1;
for i=1:gapnum
    if gappos(1, (2*i-1))>0
        gapposnew(:,(2*j-1):(2*j)) = gappos(:,(2*i-1):(2*
            i));
        gapnumnew = j;
        j=j+1;
    end
end

%Create Matrix with zeros for calculation and for gap
    Intensity itself
pfprep = zeros(size(pfimg));
gapInt = zeros(numMLC, (2*gapnumnew+1));
IntPos = zeros(size(gapposnew,1), gapnumnew);
```

```
%Calculate Sum of Intensity over the whole gap for each
    MLC Pair
for i=1:gapnumnew
    for j=1:size(gapposnew, 1)
        if(gapposnew(j, (2*i-1))>0 && gapposnew(j, (2*i))
            >0)
            pfprep(gapposnew(j, (2*i-1)), gapposnew(j,
                (2*i))) = 1;
            IntPos(j,i) = pfimg(gapposnew(j, (2*i-1)),
                gapposnew(j, (2*i))).*gapposnew(j, (2*i));
        end
    end
    gInt = pfimg.*pfprep;
    gapInt(:,2*i) = sum(gInt,2);
end

gapIntensity = zeros(size(gapInt));
gapIntensity(:,2) = gapInt(:,2);

for i = 2:gapnumnew
    gapIntensity(:,2*i) = gapInt(:,2*i)-gapInt(:,2*(i-1))
        ;
end

gapIntensity2 = gapIntensity./max(max(gapIntensity))
    .*100;

%Create Vektor with total Gap Intensities (for each gap
    for all MLCs)
totalgapInt = sum(gapIntensity,1);
gapPos(1, 1:gapnumnew) = ceil(sum(IntPos,1)./totalgapInt
    (1, 2:2:(2*gapnumnew)));
totalgapInt2 = totalgapInt./mean(mean(totalgapInt
    (:,4:2:(2*gapnumnew-2)))).*100;

img(:,gapPos-12)=0;
img(:,gapPos) = 0;
img(:,gapPos+12)=0;

intm = sum(gapIntensity, 1);
intmean = intm(2:2:2*gapnumnew)./(gapmlc);


figure(4);
imagesc(gapIntensity2);
xlabel('Gaps');
ylabel('MLC Number');
title('Intensity of Gaps over MLC Pairs; scaled');
```

```
figure(5);
bar(totalgapInt2(:,2:2:(2*gapnumnew)), 0.4);
xlabel('Gaps');
ylabel('Intensity');
title('Total Intensity of each Gap; scaled');

figure(6);
imagesc(img);
title('Original Image with calculated Gap Positions');

figure(7);
bar(intmean, 0.4);
xlabel('Gaps');
ylabel('Mean Dose');
title('Mean Dose of Gaps');

end
```

A.1.4 dMLC

```
%Function to calculate deviations of segment intensities
%Segments are parallel to MLC Pairs
%numMLC/SegmentNumber has to be an integer; MLCs have to
    be in x direction (1)

function [avSeg, meanSepSeg, standdev] = MLC(fileName,
    SegmentNumber, RS, RI)

numMLC = 52;

%reading and preparation of the image
img = prepare(fileName, 5000, RS, RI);

%Pixelwidth of one MLC pair
widthMLC = size(img, 2)/numMLC;

%Create Matrix which only has elements at the middle of
    each MLC pair this value is the mean of the 2 or 3
    surrounding values
meanIntMLC = zeros(size(img));
for i=1:numMLC
    meanIntMLC(ceil((i-1/2)*widthMLC),:) = mean(img(floor
        ((i-1/2)*widthMLC-1):ceil((i-1/2)*widthMLC+1),:));
end

figure(2);
imagesc(meanIntMLC);
title('Mean Intensity for every MLC Pair');

pfimg = zeros(numMLC, size(img,2));
```

```
%compressing the matrix, include only mean for each MLC
    pair
for i=1:numMLC
    pfimg(i,:) = meanIntMLC(ceil((i-1/2)*widthMLC),:);
end

figure(3);
imagesc(pfimg);
xlabel('Image Pixel');
ylabel('MLC Number');
title('Mean Intensity for every MLC Pair, merged');

%For every Segment take mean of all MLCs included
SegLen = numMLC/SegmentNumber;
avSeg = zeros(SegmentNumber, size(pfimg,2));
for i = 1:SegmentNumber
    avSeg(i,:) = mean(pfimg(((i-1)*SegLen+1):(i*SegLen)
        ,:),1);
end

figure(4);
imagesc(avSeg);
xlabel('Pixel Number');
ylabel('Segment Number');
title('Average Intensity over Segments');

%calculate total mean Intensity for each segment
average = mean(avSeg, 2);

figure(5);
plot(average, 'x');
xlabel('Segment Number');
ylabel('Average Intensity');
title('Total Average Intensity over Segments');

%Seperate Segments to the third dimension
sepSeg = zeros(SegLen, size(img,2), SegmentNumber);
for i=1:SegmentNumber
    sepSeg(:,:,i) = pfimg(((i-1)*SegLen+1):(i*SegLen),:);
end

%Look at each segment, calculate mean and standard
    deviation of intensities over all MLC pairs in this
    segment
meanSepSeg = zeros(SegLen, SegmentNumber);
for i=1:SegmentNumber
   meanSepSeg(:,i) = mean(sepSeg(:,100:size(img, 2),i),2)
       ;
end
```

```
figure(6);
imagesc(meanSepSeg);
xlabel('Segment Number');
ylabel('MLC Number in Segment');
title('Average Intensity over Segment and MLC in Segment'
    );

standdev = std(meanSepSeg);
figure(7);
plot(standdev, 'o');
xlabel('Segment Number');
ylabel('Standard Deviation');
title('Standard Deviation of Intensity in each Segment');

%for every MLC separately
DevIntMLC = zeros(SegLen, SegmentNumber);
for i=1:SegmentNumber
    DevIntMLC(:,i) = mean(sepSeg(:,:,i),2)./mean(mean(
        sepSeg(:,:,i),2)) -1;
end

figure(8);
imagesc(DevIntMLC);
xlabel('Segment Number');
ylabel('MLC Number in Segment');
title('Intensity Deviation for every MLC in segment to
   mean Intensity in Segment');
end
```

A.1.5 Sliding Slit

For the Sliding Slit Test only the General Preparation algorithm has been used to convert the images to dose images. These have then been analyzed to find their mean and standard deviation.

A.1.6 Snooker Cue

For the Snooker Cue Test the single frames have been converted to dose rate images and afterwards a "movie" was created with these images using the 'implay' function in MATLAB.

List of Figures

List of Tables